

**MULTISCALE ANALYSES
OF
FIBRE METAL LAMINATES**

**MULTISCALE ANALYSES
OF
FIBRE METAL LAMINATES**

PROEFSCHRIFT

ter verkrijging van de graad van doctor
aan de Technische Universiteit Delft,
op gezag van de Rector Magnificus prof. dr. ir. J.T. Fokkema,
voorzitter van het College voor Promoties,
in het openbaar te verdedigen op dinsdag 25 november om 10.00 uur

door

Marcela Viviana CID ALFARO
Ingeniero Civil Mecánico, Universidad de Chile, Chili
geboren te Coyhaique, Chili

Dit proefschrift is goedgekeurd door de promotor:

Prof. dr. ir. R. de Borst

Samenstelling promotiecommissie:

Rector Magnificus,	Voorzitter
Prof. dr. ir. R. de Borst,	Technische Universiteit Eindhoven, promotor
Prof. Dr.-Ing. C. Mieke,	Universität Stuttgart
Prof. dr. ir. R. Benedictus,	Technische Universiteit Delft
Prof. dr. ir. J. Rots,	Technische Universiteit Delft
Dr. ir. R.H.J. Peerlings,	Technische Universiteit Eindhoven
Dr. ir. A.S.J. Suiker,	Technische Universiteit Delft
Dr. sc. tech. P. Linde,	Airbus Deutschland GmbH

Dr. ir. A.S.J. Suiker heeft als begeleider in belangrijke mate aan de totstandkoming van het proefschrift bijgedragen.

Copyright ©2008 by M.V. Cid Alfaro

Cover design: M.V. Cid Alfaro & W. Hoitinga

Printed in the Netherlands by PrintPartner Ipskamp

ISBN 978-90-79488-32-2

A mi madre y a la memoria de mi padre

Foreword

The research presented in this thesis has been carried out at the Faculty of Aerospace Engineering at the Delft University of Technology. This work is part of the research project DLR.5790 - DFG 509 “Multiscale Methods in Computational Mechanics” funded by the Stichting Technische Wetenschappen (STW), the Netherlands, and the Deutsche Forschungsgemeinschaft (DFG), Germany.

This Ph.D. project has been a very challenging experience, not only from an academic point of view, but also from a personal point of view. Leaving my country, family and friends was not easy and arriving in a country with a completely different culture has not always been that simple. However, over the past four years I have met many people who have helped me to overcome these difficulties and have made my life here pleasant. The following words are meant to acknowledge everybody who has helped me, in one way or another, through this sometimes exigent process.

First of all, I would like to gratefully acknowledge my supervisor Prof. René de Borst, for giving me the opportunity to do the Ph.D. at his group and for his trust during this period. Furthermore, I would like to thank my daily supervisor Dr. Akke Suiker for his support and guidance during the research and for the fruitful discussions and feedback that have surely enhanced the quality of this work. In addition, I would like to express my gratitude to the members of the STW-DFG project on “Multiscale Methods in Computational Mechanics” for the nice debates during our meetings.

For my research I have made use of Jem/Jive, which is a finite element toolkit developed by the software company Habanera in Delft. I owe many thanks to Erik-Jan Lingen for helping me with numerical implementation issues within Jem/Jive, especially at the beginning of my research. I am also appreciatively thankful to Joris Remmers for letting me use the packages TIM and Dawn and for all the help provided during this period. Furthermore, many thanks to Clemens Verhoosel for the helpful discussions, in particular regarding multiscale methods, but also for his 'cohzone' formulation and support regarding implementation issues.

I would like to deeply thank Carla Roovers and Harold Thung for the wonderful assistance in solving administrative and technical issues. I am also grateful to my colleagues at the Aerospace Faculty in Delft for providing a very pleasant working atmosphere: Ido Akkerman, Doo-Bo Chung, Miguel Gutiérrez, Michiel Hagenbeek, Steven Hulshoff, Christian Michler, Edwin Munts, Jingyi Shi, Denny Tjahjanto, Sergio Turteltaub, André Vaders, Harald van Brummelen, Kris van der Zee and Gertjan van Zwieten. Special thanks go to my long-time roommates Clemens Verhoosel and Thomas Hille. We have had very interesting dialogues and nice coffee breaks. Thanks to Sarita Singh and Claudia Forero for their friendship. I would also like to express my gratitude to Juliana Lopez de la Cruz for her friendship, support and for the nice conversations we always have.

I am also grateful to Prof. Christian Miehe and the members of his group for providing a very enjoyable work environment during my three-month visit to the University of Stuttgart. During these months, when I was far from home, people welcomed me and made sure that I didn't feel alone. In this respect I would like to say many thanks to Serdar Göktepe, Ercan Gürses, Joel Mendez, Suad Nakid, Ingrid Bruss, Dominik Zimmermann, Martina Hofacker, Ayhan Acartürk and Irina Komarova.

Special thanks go to my friends Marjan Hettinga, Stephan Huijgen and Rossana Brantes for helping me through these years, to my family for their love and support, and to the family of Wijnand for welcoming me and making me feel more

at home here in Holland. In particular, thanks go to Leo and Marga Hoitinga for taking care of me.

Finally, I would like to say infinitely many thanks to Wijnand for always being there for me, for supporting me in all the things that I would like to achieve, and for his patience, love and care. Without him I would certainly not be able to be the person I am now, and I would also not be able to accomplish all the things I have accomplished so far. I am enormously lucky to have him by my side.

Marcela Cid
Delft, October 2008

Contents

1	Introduction	1
1.1	Fibre metal laminates	2
1.1.1	GLARE lay-up	5
1.1.2	Mechanical properties of GLARE constituents	8
1.1.3	Characteristic properties of GLARE	8
1.1.4	Possible applications of GLARE	11
1.1.5	Long term behaviour of GLARE	13
1.1.6	Manufacturing of GLARE	14
1.1.7	New generation of fibre-metal laminates	15
1.2	Typical failure modes in FMLs	17
1.2.1	Constituent failure	17
1.2.2	Delamination failure	18
1.2.3	Failure by cracking	19
1.3	Modelling aspects	19
1.4	Aims and scope of the study	20
1.5	Outline	21
2	Analysis of fracture and delamination in laminates using 3D numerical modelling	25
2.1	Introduction	25
2.2	Formulation of the interface damage model	28
2.3	Time discretisation of the interface damage model	34

2.4	Numerical model of a centre-cracked 2/1 GLARE laminate subjected to uniaxial tension	37
2.4.1	Geometry and boundary conditions	37
2.4.2	Finite element discretisation	39
2.4.3	Material properties	41
2.5	Modelling results	45
2.5.1	2/1 lay-up with elastic aluminium layers	45
2.5.2	2/1 lay-up with elasto-plastic aluminium layers	53
2.5.3	Influence of boundary conditions on failure response	57
2.5.4	Effect of initial crack length on failure strength	58
2.6	Summary of results and concluding remarks	60
3	Micromechanical study of off-axis failure behaviour of fibre-epoxy systems	63
3.1	Introduction	63
3.2	Simulation of a single-fibre composite	65
3.2.1	Mesh refinement study	66
3.2.2	Fibre-epoxy interfacial strength versus epoxy strength	71
3.2.3	Fibre-epoxy interfacial toughness versus epoxy toughness	73
3.2.4	Symmetry of fracture pattern	74
3.3	Simulation of a multiple-fibre composite	78
3.3.1	Influence of the fibre volume fraction	79
3.3.2	Influence of the fibre distribution	84
3.4	Main conclusions and comparison to experiments	88
4	Computational homogenization for simulating discrete fracture in fibre-epoxy systems	93
4.1	Introduction	93
4.2	Micro- and mesoscale modelling	95
4.2.1	Governing equations at the mesoscale	95
4.2.2	Governing equations at the microscale	97
4.3	Connection between the microscale and mesoscale	98
4.3.1	Formulation of boundary conditions on the RVE	99

4.3.2	Derivation of the mesoscopic interfacial traction	100
4.4	Numerical simulations of a fibre-epoxy specimen subjected to uni- axial tension	104
4.4.1	Geometry and boundary conditions of the fibre-epoxy sam- ple	105
4.4.2	Finite element model	105
4.4.3	Influence of sample size and fibre volume fraction	107
4.4.4	Influence of imperfections on failure response	108
4.5	Conclusions	116
	References	117
	Summary	127
	Samenvatting	131
	Curriculum vitae	137

The graphic consists of the word 'CHAPTER' in a vertical, sans-serif font to the left of a large, bold, white number '1' centered within a dark gray square.

Introduction

During the last decades the application of composite materials in engineering structures has become increasingly popular. Especially in aircraft and space structures composites are preferred above conventional materials because of their advantageous strength/stiffness versus weight ratios. In addition, the search for new and improved materials in aerospace industry has stimulated the development of hybrid materials partly made out of composites, such as Fibre-Metal Laminates (FMLs). These materials are composed of alternatively stacked aluminium and fibre-reinforced composite layers, see Figure 1.1, such that the best features of both constituents are combined. The development of FMLs came forward from the manufacturing of metal laminates, which originally started with the English aircraft manufacturer De Havilland as the first company bonding metal sheets together. Later, after the production plant of Fokker was destroyed in the Second World War, Fokker could not afford to invest in large milling machines for producing integrally stiffened panels, as a result of which Fokker engineers were stimulated to search for new technologies. Accordingly, a different structural concept

was adopted to tailor the local strength of aircraft components: laminated structures with bonded stiffeners and doublers. This was the start of the manufacturing of metal laminates that eventually led to the development of FMLs [78].

1.1 Fibre metal laminates

In the early days of laminated structures, it was not known that the fracture toughness and the fatigue properties of a laminated sheet are superior to those of a monolithic metal sheet. After performing different types of fatigue tests on the Fokker F-27 centre wings, it was found that laminate structures have a favorable resistance to fatigue crack growth. Cracks start to grow in a single layer, but the intact, adjacent layers effectively bridge the crack, thereby considerably reducing crack growth. Numerous experiments performed on FMLs with large fatigue cracks in the aluminium layers confirmed the excellent fatigue performance of this material [78]. Under realistic cyclic loading conditions, FMLs show crack growth rates that are 10 to 100 times lower than those in monolithic aluminium. The 'crack bridging' mechanism responsible for the improved fatigue resistance causes the stress intensity at the crack tip in the aluminium layers to be reduced by crack closing stresses in the intact fibres in the wake of the crack. Substantial fibre failure does not occur under fatigue loading, because the generation of controlled delamination at the interfaces between the metal and fibre-epoxy layers relaxes the fibre stresses.

The first generation of FMLs is represented by a laminate called ARALL¹. This laminate is reinforced by aramid fibres and was developed primarily for wing applications. Nevertheless, studies performed on a full scale Fokker 27 wing panel showed that ARALL is quite sensitive to strength reductions caused by holes drilled in the material and that locations with thickness strengthening (i.e., doublers bonded on the structure to increase the strength) are susceptible to premature fatigue cracking. However, the large wing panel made of ARALL was subjected to three times the design load duration for an F-27, i.e., a cyclic loading representative of 270.000 flights. The tests showed that only minor cracks appeared

¹ARALL is an acronym for Aramid Reinforced ALuminium Laminates

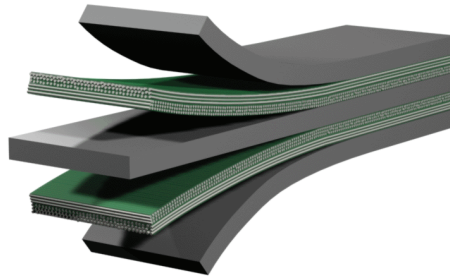


Figure 1.1: Typical lay-up of a fibre-metal laminate (reprinted from [56] with kind permission of Joris Remmers).

in some of the outer layer of ARALL. Essentially, an equivalent aluminium part would have failed dramatically under these loading conditions. In addition to the increased safety level, a weight saving of 33% was achieved in comparison to the original aluminium design [78].

Unfortunately, ARALL appeared not to be a good candidate for fuselage structures. Testing related to the application of ARALL in fuselage structures showed that the aramid fibres around a fatigue crack break relatively easily, as a result of which a reduction of crack growth in the aluminium layers can no longer be warranted. The explanation of this phenomenon was found in the poor connection of the aramid fibres with the adhesive, resulting in fibre pull-out. When the pulled out fibres are subsequently loaded under compression, they break due to their relatively low compressive strength. This set-back, however, did not stop the development of fibre-metal laminates, and in 1987 a new laminate variant called GLARE² was introduced. GLARE is reinforced by glass fibres, which have a higher compressive strength and a better damage tolerance behaviour than the aramid fibres in ARALL [17]. This material, which was developed at the Delft University of Technology, is ideally suited for being applied in fuselage structures.

Research on impact resistance showed that under relatively low loading ve-

²GLARE is an acronym for GLAss fibre REinforced laminate

locities GLARE behaves as good as aluminium and is superior to carbon fibre composites [77]. In addition, under relatively high loading velocities the impact resistance of GLARE is much better than that of aluminium. It was further concluded that damage in terms of denting of the aluminium layers can be easily detected due to clearly visible plastic deformations. This is a difference with composites, which typically fail in a more abrupt, brittle fashion, such that it is much more difficult to detect damage (on time). The first commercial application of GLARE goes back to 1990 when, due to its excellent impact properties, it was used in the cargo floor of the Boeing 777. Extensive fire resistance tests performed by Boeing demonstrated that GLARE also has an excellent burn-through resistance. The fire resistance tests were carried out up to temperatures of 1200° Celsius, and demonstrated that GLARE prevents complete penetration of fire for more than fifteen minutes [77].

In the early nineties, Airbus Industry started a design study for a very large passenger aircraft. This aircraft was intended for short and long range passenger transport with a capacity between 550 and 800 passengers, as well as for pure freight and combined freight passenger missions. The final aircraft design was released in 1996, and was named A3XX. At that time GLARE was already regarded as a potential candidate for being applied in the construction of the fuselage of this aircraft. Consequently, in The Netherlands (i.e., at the Delft University, the National Aerospace Laboratory and Stork Fokker) research on GLARE increased significantly. Studies on fuselage structures of the A320 showed that with GLARE a weight saving of 25.9% could be reached over aluminium. In addition, investigations on the Airbus A330 and A340 demonstrated a weight saving of 20% and 14 – 17%, respectively, as reported in [78].

A disadvantage of GLARE is that this material is more expensive than a traditional aluminium alloy, which appeared to be the main obstacle for its direct application. Nonetheless, after an extensive cost study it was indicated that, although the material costs of GLARE are high, the total costs of a finished GLARE product come very close to those of an aluminium product. This led to the conclusion that GLARE should not be produced as a sheet material, which has to be shaped and machined into a product as is done for aluminium, but as a component. Accordingly, the material is laid-up and cured in a curved mould such that



Figure 1.2: GLARE panel used in the upper part of the fuselage of the Airbus A380 (reprinted from [40]).

after processing a product comes out of the autoclave with the right shape for a specific aircraft application. The final product thus includes the appropriate local fibre orientations and reinforcements with respect to the application it is meant for. With such a manufacturing procedure, the number of production steps, and thus the costs, are reduced significantly. This finally led to the application of GLARE in a significant part of the Airbus A380 fuselage, see Figure 1.2, and in the leading edges of the vertical and horizontal tail planes.

1.1.1 GLARE lay-up

Nowadays GLARE is produced in six different standard grades. These grades are all based on (various) fibre-epoxy (prepreg) layers composed of unidirectional S-glass fibres embedded in a FM94 adhesive. The S-glass fibres have a diameter of approximately $10\ \mu\text{m}$. An individual prepreg layer with UniDirectional (UD) fibres has a nominal thickness of $0.127\ \text{mm}$ and a nominal fibre volume fraction of 0.59 . It is possible to stack prepreg layers with different fibre orientations in between two aluminium layers, resulting in different standard GLARE grades. As an example, the fibre-epoxy layer of the grade GLARE 4 has been presented in detail in Figure 1.3. The GLARE grades, the grade and thickness of the metal layers, the orientation of the UD-prepreg layers, the total thickness of the composite layer and the most important beneficial characteristics, are listed in Table 1.1.

A coding system is used to comprehensively define the laminate grades in

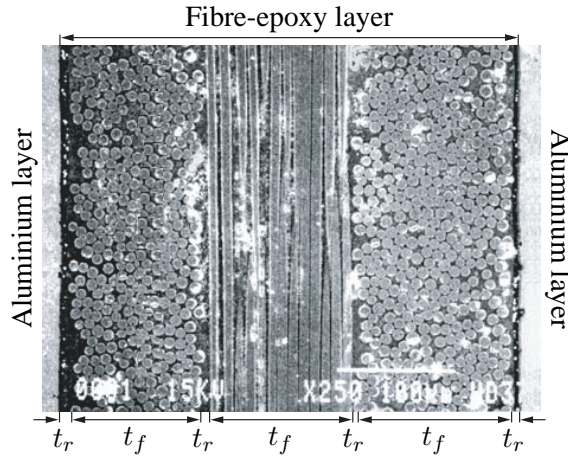
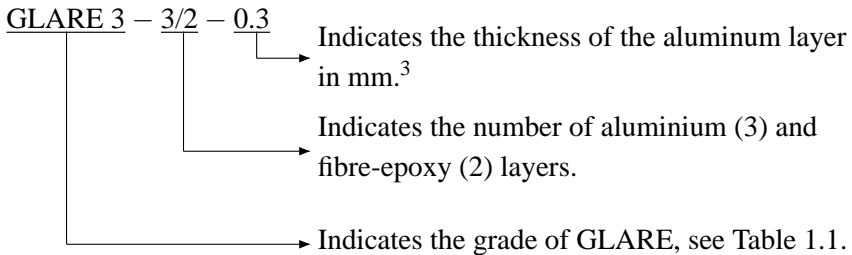


Figure 1.3: Fibre-epoxy layer in a GLARE 4 laminate. The thickness t_r represents the resin-rich area in the fibre-epoxy layer, whereas t_f represents the fibre-rich area (reprinted from [17]).

Table 1.1. This coding system is important for design, production and material qualification. For example, the cross-ply laminate schematised in Figure 1.1 is coded as:



The configurations GLARE 1 and GLARE 2 only have fibres oriented in one direction. These configurations are ideally suited for applications with unidirectionally loaded structural components, such as stringers, stiffeners and crack stoppers.

³In the case where aluminum layers of different thickness are used, the thicknesses of the individual layers are denoted in the order of appearance in the aluminium lay-up.

Table 1.1: GLARE grades, composition and main beneficial characteristics [1, 28].

GLARE grade	Metal layers		Prepreg layers ^a		Main beneficial characteristics
	Grade	Thickness [mm]	Orientation ^b [°]	Thickness [mm]	
GLARE 1	7475-T761	0.3 - 0.4	0/0	0.25	fatigue, strength yield stress
GLARE 2A	2024-T3	0.2 - 0.5	0/0	0.25	fatigue, strength
GLARE 2B	2024-T3	0.2 - 0.5	90/90	0.25	fatigue, strength
GLARE 3	2024-T3	0.2 - 0.5	0/90	0.25	fatigue, impact
GLARE 4A	2024-T3	0.2 - 0.5	0/90/0	0.375	fatigue, strength in 0° direction
GLARE 4B	2024-T3	0.2 - 0.5	90/0/90	0.375	fatigue, strength in 90° direction
GLARE 5	2024-T3	0.2 - 0.5	0/90/90/0	0.5	impact
GLARE 6A	2024-T3	0.2 - 0.5	+45/-45	0.5	shear, off-axis properties
GLARE 6B	2024-T3	0.2 - 0.5	-45/+45	0.5	shear, off-axis properties
GLARE HS ^c	7475-T761	0.3-0.4	see GLARE 2 - 5	see GLARE 2 - 5	fatigue, strength yield stress

^a The number of orientations in this column is equal to the number of unidirectional prepreg layers in each composite layer. The thickness corresponds to the total thickness of a fibre-epoxy layer in between two aluminium layers.

^b The (axial) rolling direction is defined as 0°, the transverse rolling direction is defined as 90°.

^c High Strength (HS) GLARE has similar standard fibre lay-ups as in GLARE 2 to GLARE 5, but contains aluminium 7475-T761 and FM906 epoxy (instead of aluminium 2024-T3 and FM94 epoxy).

GLARE 1 has been replaced by a whole new family of laminates that contains aluminium 7075-T761 (which has a relatively high yield strength) in combination with FM906 epoxy (instead of FM904 epoxy). This family is characterised

by similar lay-ups as GLARE 2 to GLARE 6 listed in Table 1.1. GLARE 3 is suitable for applications with equibiaxially loaded structural components, such as parts of a fuselage skin and bulkheads. GLARE 4 is suitable for locations in the fuselage where the load in one direction is twice the load in the other (perpendicular) direction. GLARE 5 has a particularly good impact resistance and therefore has been used in impact critical components, such as floors and cargo lines. Finally, GLARE 6 has a strong off-axis and shear failure resistance, and thus can be applied to structural parts subjected to high shear loading.

1.1.2 Mechanical properties of GLARE constituents

The mechanical behaviour of GLARE is based upon the mechanical properties of its constituents, i.e., the aluminium and fibre-epoxy layers. The main properties of the constituents are listed in Table 1.2. The effective mechanical properties of GLARE, in general, vary with the Metal Volume Fraction (MVF), which is defined by the ratio between the total thickness of the n aluminium layers, $\sum_i^n t_i$, and the laminate thickness t_{tot} , i.e.,

$$\text{MVF} = \frac{\sum_i^n t_i}{t_{tot}}. \quad (1.1)$$

Experimental studies have demonstrated that most basic mechanical properties of GLARE, such as the ultimate failure strength, yield strength, Young's modulus, shear modulus, gross blunt notch strength, bearing strength and specific weight, relate in a (approximately) linear fashion to the MVF [17].

1.1.3 Characteristic properties of GLARE

As already mentioned briefly, the characteristics of GLARE are generally better than those of individual aluminium and fibre-epoxy layers. The most important thermal-mechanical characteristics of the GLARE constituents, as reported in [17], are summarised in Table 1.2.

Table 1.2: The thermo-mechanical mechanical properties of the constituents of GLARE, as reproduced from [17]. Subscript 1 refers to the rolling direction of the aluminium while subscript 2 refers to the direction perpendicular to the rolling direction, i.e., the transverse direction.

Property	Dimension	UD prepreg ($V_f = 60\%$)	Aluminium 2024-T3
Young's modulus, E_1	[GPa]	54.0	72
Young's modulus, E_2	[GPa]	9.4	72
Ultimate strength, σ_{ult}	[MPa]	2640	455
Ultimate strain, ε_{ult}	[%]	4.7	19
Poisson's ratio, ν_{12}	[-]	0.33	0.33
Poisson's ratio, ν_{21}	[-]	0.0575	0.33
Shear modulus, G_{12}	[GPa]	5.55	27.6
Density, ρ	[kg/m ³]	1980	2770
Thermal expansion coefficient, α_1	[1/°C]	$6.1 \cdot 10^{-6}$	$23.4 \cdot 10^{-6}$
Thermal expansion coefficient, α_2	[1/°C]	$26.2 \cdot 10^{-6}$	$23.4 \cdot 10^{-6}$

Corrosion

GLARE possesses a good corrosion resistance. This behaviour can be ascribed to the usage of relatively thin aluminium sheets. Thin aluminium sheets are manufactured by following the rolling process with a relatively fast quenching process, which leads to less alloy elements at the crystal boundaries of the aluminium and thus to an improvement of the corrosion resistance. Furthermore, the aluminium sheets are anodised and coated with a corrosion-inhibiting primer prior to bonding these to prepreg layers. The outer aluminium layers can be supplied clad instead of anodised/primed in order to improve the surface corrosion resistance. In addition, through-the-thickness corrosion in a FML is prevented due to the barrier role of the fibre-epoxy layers.

Damage tolerance

The damage tolerance of GLARE is higher than that of the individual aluminium and fibre-epoxy layers. The strength of GLARE structures remains preserved for conditions causing significant strength reduction in aluminium or composite structures, such as those occurring at rivet holes during fatigue loading.

Fatigue

The fatigue resistance of GLARE is substantially higher than that of aluminium due to the crack bridging effect explained previously. As a consequence, the crack growth rates remain very low and at an approximately constant level, thus simplifying the determination of inspection intervals. Further, it has been found that the fatigue crack initiation period in the aluminium layers of GLARE is significantly less than that of a comparable aluminium 2024-T3 sheet. In monolithic aluminium the largest part of the fatigue life is characterised by crack initiation while for FMLs this is characterised by crack growth.

Fire resistance

GLARE has shown to have better fire resistance properties than its constituents. Although the matrix of composite layers melts, the glass fibres stay intact at temperatures of 1000 °C to 1100 °C, acting as a fire barrier. Further, GLARE demonstrates an additional benefit in firewall testing: The heat of the fire enforces thick laminates to delaminate, which creates a large improvement in insulation. Since the metal layers behind the first fibre-epoxy layer do not melt, the temperature inside the laminate remains at an acceptable level. In addition, the intact metal layers provide some coherence to the structure, preventing its deterioration that leads to final collapse.

Impact

The impact properties of GLARE grades with biaxial fibre layers are better than those of aluminium, despite the fact that the impact behaviour of glass fibre composites lies below that of aluminium. The impact properties of GLARE are es-

pecially good if the loading is characterised by relatively high strain rates, such as occurring during hail strike or bird impact. After impact has taken place, it is possible to observe a dent in the surface of GLARE, which makes the visual inspection of damage due to impact loads rather simple (as in aluminium).

Others characteristics

- The specific weight of GLARE is approximately 10% lower than that of aluminium.
- GLARE can be formed and manufactured in a wide variety of shapes.
- GLARE can be machined and repaired using similar tools and procedures as those used for aluminium alloys.
- Like composites, GLARE is affected by hot-wet ageing under accelerated conditions. However, since in GLARE there is a large amount of unaffected aluminium, moisture absorption and property reduction are less in comparison to glass fibre composites.

1.1.4 Possible applications of GLARE

The feasibility of GLARE as an aerospace material is determined by its potential to establish significant weight savings and reduce maintenance costs for a competitive price. The properties of GLARE listed in the previous section allow for the applications listed below [78].

Bulkheads

The combination of fatigue, strength and damage tolerance properties makes GLARE attractive for this application.

Cargo barriers

The good impact properties make GLARE very attractive for this application. Cargo barriers are heavy structures that separate the cargo from the cockpit. They

prevent the cargo from seriously damaging the cockpit under crashing conditions.

Cargo containers

The superior impact properties of GLARE provide a good blast resistance.

Firewalls

The excellent fire resistance properties combined with a high impact resistance and a good formability make GLARE a serious candidate for firewall applications.

Floors in passenger and cargo areas, aircraft doors, lower flap skin, wheel doors, leading edge of tail planes and cockpit roof

The impact properties of GLARE, in particular those of GLARE 5, allow for using this material in areas that are sensitive to impact due to, for example, human handling or bird striking.

Fuselage skin

The good fatigue properties and the high damage tolerance make GLARE especially suitable for fuselage skins.

Stringers and frames

The extremely high strength and good fatigue properties of GLARE grades with unidirectional fibre-epoxy layers allow for the application of this material in structural parts with one dominant loading direction.

Thermal protection systems for space vehicles

The excellent fire resistance of GLARE allows for using this material for the thermal protection of space vehicles.

Upper and lower wing skins

A high fatigue resistance, a high strength and a high damage tolerance combined with the latest developments in the manufacturing of large-curved panels make the material ideal for this type of applications.

From the possibilities mentioned above the use of GLARE in fuselage skins, floors and forward bulkheads has resulted in series applications [78]. Since the aircraft industry is somewhat conservative, for a new material a long evaluation and analysis is considered necessary in order to make the application of the material possible. Furthermore, for the realisation of new applications of GLARE, some additional conditions have to be fulfilled, i.e., manufacturers must have confidence in the material concept, GLARE must provide clear benefits over other materials against acceptable costs, and the material must be sufficiently available.

1.1.5 Long term behaviour of GLARE

It is important that materials used for the construction of aircrafts maintain optimal properties during the entire lifetime of the aircraft. One of the main threats to aircraft materials are environmental effects, i.e., moisture combined with temperature, ranging from cold, dry air conditions at cruise altitude to hot, humid air conditions in tropical environments. When GLARE is used in humid environments, it may be susceptible to corrosion. In order to decrease/eliminate the amount of corrosion, a protective layer can be applied onto the surface of the material. This may be done through anodisation, by applying a clad layer of pure aluminium and/or by using a paint system, such as a primer combined with a top coat. The usage of GLARE in humid conditions may also lead to moisture absorption in the fibre-epoxy layers, which is undesirable from the aspects of weight increase and its deteriorating effect on the mechanical properties. The effect of moisture on epoxy materials is typically notable through processes like swelling, plasticizing, hydrolysis and physical ageing can occur. Moisture effects may be reversible or irreversible, which for a large part depends on how moisture is present in the material. If moisture appears in the form of free molecules, the process is generally reversible. Conversely, if water molecules are chemically bonded to polymer

molecules, the process is typically irreversible.

Although under most circumstances the influence of moisture on GLARE is expected to be relatively small, especially in comparison to conventional composites, further research is needed for obtaining a more detailed understanding of the influence of moisture. Nevertheless, this type of research falls beyond the scope of the present thesis.

1.1.6 Manufacturing of GLARE

For practical applications GLARE was initially produced as flat sheets. The idea was that aircraft manufacturers would use these flat sheets in order to manufacture specific components using conventional methods developed for metal structures, such as forming, bonding, riveting, etc. Several studies showed the benefits of GLARE in performance and weight saving, but also indicated the high production costs in comparison to those of conventional aluminium structures. As a consequence, a series of developments related to manufacturing were initiated in order to reduce the production costs [78]. The main manufacturing developments are summarised below.

Splicing concept

In the years 1990-1995 GLARE laminates were manufactured as flat sheets. However, the width of the aluminium sheets used in the manufacturing of GLARE was limited to 1.65 m, while fuselage skin sheets with sizes up to 2 m and more were needed. As a solution to this problem the splicing concept was developed. This manufacturing method consists of positioning aluminium sheets side by side with a narrow gap of about 1 mm in between, such that 3 to 4.5 m wide GLARE panels can be obtained. The gaps between the metal sheets are positioned slightly staggered across the thickness of the laminate to prevent substantial strength loss in a specific cross section. A drawback of the splicing concept is the occurrence of sudden delamination, especially in the outer aluminium layers of the laminate at which the transverse stress may exceed 400 MPa. To solve this problem, doublers were bonded over the spliced area by means of a second autoclave cycle, which locally reduce the stress and thus the material damage. A disadvantage of these

spliced panels is that their manufacturing process includes (at least) two cure cycles. However, this problem can be solved by using a self-forming technique, see below.

Self-forming technique

This technique allows for manufacturing a complete spliced panel (including doublers) in only one cure cycle (thus avoiding the difficulty of manufacturing spliced GLARE panels in two cure cycles). Under static and cyclic loading conditions the splices manufactured with the self-forming technique are no longer critical in terms of delamination. This is due to the fact that the adhesive, which is added to the locations of load transfer between metal layers, has a much higher shear strength than the prepreg layers.

Single-curved panels

Single-curved panels can be produced by performing the lay-up of the metal and prepreg layers in a single curved mould. This technique does not add extra costs to the GLARE production beyond the costs of the lay-up mould. Additionally, this method avoids the production step where the panel needs to be roll-formed to the required curvature, as typical for aluminium panels.

Double-curved panels

Double-curved GLARE panels are obtained by laminating all metal and prepreg sheets in a double-curved mould and forming these to the required shape in a single autoclave cure cycle. This method eliminates the need for a difficult and costly forming process.

1.1.7 New generation of fibre-metal laminates

In theory, laminates may be composed of arbitrary components. However, problems following from high internal stresses, galvanic corrosion and voids creation may happen when the components are not chosen appropriately. Other boundary conditions in the composition of laminates are provided by the availability

of components and their costs; i.e., a laminate will not be applied if its price is exceptionally high or its components are difficult to acquire.

There are a large number of different (potential) type of fibres that can be used in fibre-metal laminates. Initially, aramid fibres were utilised (ARALL). However, due to their inferior bonding and strength properties under compressive loading, these fibres were replaced by glass fibres (GLARE). The usage of carbon fibres in FMLs is another option. The combination of carbon fibres and aluminium may lead to galvanic corrosion, but a combination with titanium does not have this problem and results in a laminate with a high stiffness. Other fibre options are ceramic, synthetic, organic or silicon carbide fibres.

The metals most commonly used in FMLs are aluminium and titanium. Other metals, such as stainless steel, high strength steel or niobium, can be applied as well. Furthermore, different adhesives are available, such as epoxy, bismaleide, phenolics, cyanate esters and thermoplastics. The main requirements for the adhesive used in FMLs are a good shear and toughness behaviour. Additional points of attention in the selection of an adhesive are its bonding properties with the fibres and the metal layers, the sensitivity to temperature and moisture, the flow properties, and the glass transition temperature.

The specific application of a laminate eventually determines the selection of its individual components. For example, if GLARE were to be used at higher temperatures, the standard 120 °C curing epoxy may be replaced by a 177 °C curing epoxy and the 2024-T3 aluminium may be replaced by a 2024-T81 alloy. Such a laminate can be used in applications with temperatures up to 180 °C, such as engine covers or fighter applications. Supersonic aviation, in which subsonic heating plays an important role, is also one of the possible applications of this laminate.

Carbon-titanium laminates were investigated in the early nineties. The good combination of high stiffness, high yield strength, good fatigue and impact properties at both room and elevated temperatures is an important advantage of this type of laminate. Since both titanium and carbon fibres can be exposed to temperatures up to 300 °C, this combination makes the laminate extremely suitable for high temperature applications. Carbon-titanium laminates are very attractive for applications in space structures, due to their good mechanical and thermal prop-

erties combined with a low density, a high damage tolerance and various manufacturing possibilities. Compared to GLARE, carbon-titanium laminates have a higher strength and stiffness and better fatigue properties. Moreover, the density of this laminate is lower than that of GLARE, due to the lower density of the carbon fibres, which means that a greater weight reduction is possible in aircraft applications.

FMLs can also be attractive for applications other than those aerospace engineering. In fact, it is the freedom of choosing its components and lay-up in accordance with the specific requirements that makes the concept of FMLs flexible and competitive in many practical applications.

1.2 Typical failure modes in FMLs

Failure processes in FMLs are rather complicated and often involve multiple failure modes. Failure typically takes place in one of the constituents (constituent failure) or at the interface between different plies or constituents (delamination failure).

1.2.1 Constituent failure

Several important failure modes of the GLARE constituents can be distinguished, as observed experimentally in various GLARE grades [15, 17, 76].

Failure modes in the metal layer

The dominant failure mechanisms in the metal layers are cracking and plasticity. These failure mechanisms are identical to those of a monolithic metal sheet. In its elastic range the aluminium attracts more load than the prepreg. Increasing the load will cause the aluminium to yield, as a result of which a plastic zone develops. A further continuation of the loading can induce cracking, which normally occurs in the outer metal layers. Nevertheless, under specific circumstances cracking may (also) happen in the inner layers of the laminate. When a layer is cracked,

the load is transferred by the adjacent layers. This redistribution of loading may lead to interfacial delamination between layers.

Failure modes in the composite layer

In fibre-epoxy layers the following failure mechanisms can take place: matrix cracking, fibre-matrix debonding, fibre-matrix interfacial shear failure, fibre fracture, fibre pull-out and fibre splitting. Fibre failure is expected, for example, at the edges of a delamination zone, as a result of a strong local clamping of fibres in this region. Another source for fibre failure is when a crack in the aluminium layer is bounded by an adjacent layer and delamination at the layer interface remains absent. This may induce significant stress concentrations in the fibres, eventually leading to fibre failure and continued growth of the aluminium crack.

1.2.2 Delamination failure

In FMLs generally two types of delamination can be distinguished, as described below.

- (i) Static delamination. This type of delamination occurs without fibre failure and develops as a result of an increasing shear load between the metal and prepreg layers. This type of delamination relaxes the stress concentration in the (intact) fibre-epoxy layer, and increases the local stress in the aluminium layers, resulting in the development of a substantial plastic zone. Static delamination can also take place between the fibres and the epoxy (adhesive failure), in the epoxy itself (cohesive failure) or between the epoxy and the aluminium layers (adhesive failure).
- (ii) Dynamic delamination. This type of delamination is accompanied by sudden debonding between fibre and epoxy and by fibre failure. It is observed experimentally that the area of dynamic delamination is small compared to that of static delamination.

A typical example of delamination is buckling delamination, where one or more layers separate from the remainder of the laminate due to high compressive loads. Interlaminar shear failure is another source for delamination, where an interface fails due to a lack of shear strength. This may occur when the specimen is subjected to a high out-of-plane (transverse) shear load. Another delamination

mode is free-edge delamination, which happens as a result of the specific stress distribution at laminate edges, where the net result is the emergence of a peel force at ply interfaces.

1.2.3 Failure by cracking

Essentially two types of cracking may be distinguished in a GLARE laminate [2, 78]:

(i) Part-through cracks. These are cracks arising in one or more aluminium layers. When the fibres in the prepreg layers remain intact, these may bridge the crack resulting in a reduced stress intensity at the crack tip. The part-through cracks are mainly caused by fatigue loading and they originate, for example, from rivet holes, scratches, corrosion damage or lightning strikes.

(ii) Through-the-thickness cracks. These are cracks that develop in the prepreg and aluminium layers simultaneously. Through-the-thickness cracks typically appear when an object penetrates the structure, for example under the impact of a bird strike or a runway debris.

1.3 Modelling aspects

In order to ensure maximum reliability of FMLs under service conditions, the failure mechanisms of these materials, as occurring at different scales of observation, must be well understood. On the structural or macroscopic level, fracture may be regarded as a structural defect that is characterised by failure mechanisms developing at lower scales of observation. At the mesoscopic level, the main failure mechanisms are delamination between metal and prepreg layers and crack propagation and plasticity in the metal layers. Figure 1.4(a) gives an example of delamination between two adjacent laminate layers. At the microscopic level, the prominent failure mechanisms are cracking in the epoxy matrix, debonding between fibres and matrix, fibre breakage and pull-out of broken fibres. Figure 1.4(b) shows an example of failure at the microscale, namely matrix cracking and fibre-matrix debonding.

In this thesis the finite element method is used to simulate the static failure

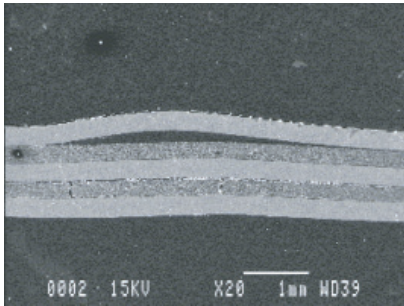
behaviour of FMLs, in particular GLARE, at the meso- and microscales. At the mesoscale, the individual layers of the laminate are modelled as homogeneous materials. The aluminium and fibre-epoxy layers are discretised with solid-like shell elements, see [29, 53, 56], and delamination and crack growth are modelled in a discrete fashion, using interface elements equipped with a mixed-mode damage model, see also [3–5, 29, 56–58].

Interface elements equipped with a cohesive-zone model serve as a convenient tool for describing mesoscale fracture in layered materials. In a cohesive-zone formulation, the fracture process is modelled by a traction-separation relation specified along a discrete line (in 2D) or plane (in 3D). The traction-separation relation used for modelling the fracture process is often chosen in a pure phenomenological or mathematically convenient manner. Commonly used traction-separation relations have a bilinear [13, 72], trapezoidal [73] or exponential [79] shape.

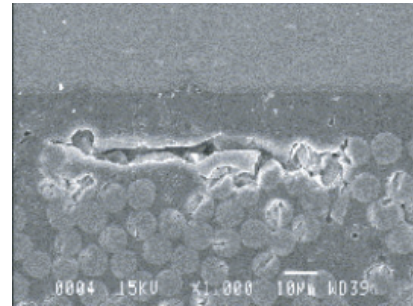
The details of small-scale fracture processes within prepreg layers are generally not taken into account in mesoscale traction-separation relations for laminate failure. However, it is one of the objectives of this thesis to connect the complex microscale fracture behaviour in a fibre-epoxy layer to a mesoscopic traction-separation law with the aid of a numerical homogenization approach. To accomplish this goal, at the microscale a representative sample of the prepreg layer is analysed. The epoxy matrix and the fibres are discretised using continuum elements and the microscopic failure mechanisms are simulated with the cohesive surface methodology. Matrix cracking is modelled by placing interface elements furnished with a mixed-mode damage model in between all continuum elements in the epoxy matrix. In the same fashion, debonding between fibres and matrix is modelled by introducing interface elements at the physical interface between fibres and epoxy.

1.4 Aims and scope of the study

The main objectives of this thesis are to analyse the fracture behaviour of laminated materials at the meso- and microlevels and to couple the failure mechanisms at both scales by means of a numerical homogenization method. In order to fulfill those objectives the following steps are performed:



(a) Mesoscale level. Local buckling of the top layer of a GLARE 2-3/2-0.3 specimen after being subjected to a three point bending test.



(b) Microscale level. Debonding between fibres and matrix and cracking in the matrix of the prepreg layer. The crack propagates in the transition zone between fibre-low and fibre-rich parts of the prepreg layer.

Figure 1.4: Failure mechanisms of a GLARE laminate at different scales of observation (reprinted from [16]).

- (i) An interface damage model is developed that can be used for simulating discrete cracking and delamination in FMLs, both at the meso- and microscales.
- (ii) Finite element simulations are performed at the mesoscale in order to study the failure mechanisms at this scale, such as interfacial delamination between two adjacent layers and cracking and plasticity in metal layers.
- (iii) Finite element simulations are performed at the microscale to analyse the failure mechanisms present at this scale, such as cracking in the epoxy matrix and debonding between the fibres and the epoxy matrix.
- (iv) A computational homogenization method is developed in order to relate the complex microscale fracture behaviour in the fibre-epoxy layer to a mesoscale traction-separation relation that can be used to model adhesive failure in laminates.

1.5 Outline

The outline of this thesis is as follows.

Chapter 2. In this chapter, the static failure behaviour of the fibre-metal lam-

inate GLARE is examined using 3D finite element simulations. The configuration analysed is a centre-cracked tensile specimen composed of two aluminium layers sandwiching a cross-plyed, fibre-epoxy layer. The crack and delamination growths are simulated by means of interface elements equipped with a mixed-mode damage model. The formulation and time discretisation of the interface damage model used for the simulation of fracture is presented. The results from the numerical simulations are discussed, starting with the response of a 'quasi-brittle' GLARE laminate with elastic aluminium layers (where the fracture strength is compared to a closed-form expression presented in [62]), followed by the response of a 'ductile' GLARE laminate with elasto-plastic aluminium layers. The failure response is computed for two different types of boundary conditions at the vertical edges of the specimen. Further, a study of the effect of the initial crack length on the laminate failure strength is performed, where the results are compared with experiments of de Vries [17]. The chapter ends with summarising the main analyses results.

Chapter 3. In this chapter, the failure behaviour of unidirectional fibre-epoxy systems is analysed with 2D (plane-strain) finite element simulations. The fibres and matrix are discretised using continuum elements. To simulate matrix cracking and fibre-matrix debonding, interface elements furnished with a mixed-mode damage model are placed in between the continuum elements. The interface damage model used in the numerical simulations is the damage model proposed in Chapter 2. As a start, numerical simulations are discussed of a single fibre embedded in an epoxy matrix and loaded under uniaxial tension. A mesh refinement study is performed in order to examine the objectivity of the numerical results as a function of the finite element discretisation. The effect is examined of the ratio between the fibre-epoxy interfacial strength and the epoxy strength on the failure behaviour of the system, as well as the influence of the ratio between the toughnesses of the fibre-epoxy interface and the epoxy matrix. Further, an assessment of the validity of the usage of symmetry boundary conditions for the single-fibre matrix configuration is performed. Subsequently, numerical simulations on uniaxially loaded epoxy systems containing multiple fibres are presented. As for the single-fibre epoxy system, the influence of the ratio between the fibre-epoxy strength and the epoxy strength on the failure response is studied. In addition,

the effect of the fibre volume fraction and the fibre distribution on the failure behaviour of the system is analysed. The chapter ends with a summary of the main conclusions of the study, and a qualitative comparison of the simulation results with experiment results presented in the literature.

Chapter 4. In this chapter, a numerical homogenization method is presented that connects the microscopic fracture behaviour in fibre-epoxy samples to a mesoscopic traction-separation law. The homogenization method is applied to fibre-epoxy samples loaded under uniaxial tension. It is studied how the traction-separation response and the corresponding microscopic failure pattern are influenced by the finite element discretisation, the specimen size, the fibre volume fraction and the number and position of imperfections. The chapter ends with a summary of the results.

Analysis of fracture and delamination in laminates using 3D numerical modelling

2.1 Introduction

Failure under tensile loading is a design limiting characteristic of fibre-reinforced, layered composites. Experimental studies have shown that the effective tensile response of these materials is bounded by the development of various failure mechanisms at a lower scale, such as transverse matrix cracking, fibre decohesion and fracture, and interfacial delamination, see for example [12, 17, 21, 46, 55, 71, 78] and references therein. In addition, modelling studies have demonstrated that the cracking and delamination patterns typically observed in layered composites depend upon local geometrical and material properties, such as the number, location and size of initial flaws, the stacking sequence, the fibre volume fraction, the

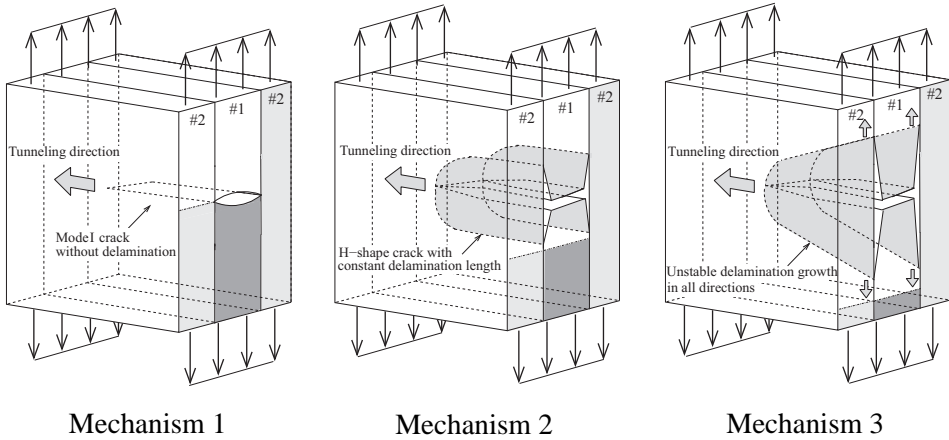


Figure 2.1: Three possible failure scenarios for a brittle laminate composed of two dissimilar, isotropically elastic materials subjected to uniaxial tension (taken from Suiker and Fleck [62]). *Mechanism 1*: Tunneling of a stable mode I crack with delamination absent. *Mechanism 2*: Tunneling of a stable H-shape crack with constant delamination length. *Mechanism 3*: A tunneling crack with unstable delamination developing in all directions.

toughness and stiffness characteristics of the individual plies, the interfacial delamination toughness, and the presence of residual stresses [8, 14, 18, 32, 36, 42, 43, 47, 66]. Recently, Suiker and Fleck [62] studied the competition of three possible failure mechanisms for a laminate composed of two dissimilar isotropically elastic layers, subjected to uniaxial tension, see Figure 2.1. These failure mechanisms are assumed to have grown from a large pre-existing flaw in the mid-layer (material #1), where 'mechanism 1' reflects the tunneling of a stable mode I crack in the mid-layer with delamination absent, 'mechanism 2' represents the tunneling of a stable H-shape crack with constant delamination length and 'mechanism 3' relates to a tunneling crack with unstable delamination growth in all directions. It was found that the operative failure mechanism is strongly determined by the relative toughness of layer and interface, and to a lesser extent by the stiffness mismatch of the layers, the location(s) of the initial flaws(s), and the number of plies.

The results presented in [62] were determined combining 2D linear elastic fracture mechanics solutions for the problems of (i) plane-strain delamination of an H-shape crack and (ii) steady-state tunneling of an H-shape crack. In line with this approach, the crack nucleation phase was ignored, as well as the presence of plastic deformations in the individual layers. These effects, however, may contribute to the static failure behaviour of laminates containing ductile layers, such as the fibre-metal laminates ARALL and GLARE. In the present chapter, the effects of plasticity and crack nucleation on the tensile failure response of GLARE are examined by means of 3D finite element analyses. The configuration studied is composed of two aluminium alloy sheets sandwiching a cross-plyed, fibre-epoxy layer, where a horizontal initial crack is placed at the centre of the specimen, across the thickness of the aluminium sheets, i.e., a centre-cracked tensile specimen is studied. After imposing the tensile loading, the centre crack starts to tunnel in the aluminium layers and induces delamination at the interfaces between the aluminium and fibre-epoxy layers, effects that are simulated by means of interface elements equipped with a mixed-mode damage model, see also [3–5, 29, 56–58]. For the interface damage model used in the present study, the formulation of the mode-mixity is based upon an energy criterion regularly applied in linear elastic fracture mechanics studies [43, 44], using a derivation procedure similar to the one proposed recently by Turon *et al.* [72]. In addition, the kinetic law describing the evolution of the damage process is taken as rate-dependent. This is done to account for rate effects generated during interfacial delamination, and to avoid numerical convergence problems induced by crack bifurcations. The incorporation of these two features in the interface damage formulation distinguishes the present model from most other models presented in the literature. The individual aluminium and fibre-epoxy layers of the laminate are modelled by solid-like shell elements [29, 53, 56]. These elements allow for a linear strain field in thickness direction, which avoids the effect of Poisson-thickness locking that appears in conventional volume elements with a high aspect ratio in spatial dimensions, i.e., 'slender' volume elements [9]. The isotropic, elastoplastic behaviour of the aluminium layer is simulated using a J_2 -plasticity model with an exponentially saturating hardening law. The cross-plyed, fibre-epoxy layer is modelled as isotropically elastic. This simplification, which is reasonable if the

elastic mismatch between fibres and matrix is moderate, allows part of the numerical results to be quantitatively compared to those presented in Suiker and Fleck [62]. Furthermore, the fracture mechanisms observed in the present study can then be adequately validated against the failure scenarios depicted in Figure 2.1.

The chapter is organised as follows. Section 2.2 contains the formulation of the interface damage model used for the simulation of fracture within the laminate layers, and mixed-mode delamination along the interfaces between the layers. The traction-separation law and the rate-dependent kinetic law for interfacial damage are specified, where the mode-mixity for damage growth is derived from linear elastic fracture mechanics concepts. In Section 2.3 the time discretisation of the model is discussed, which is based on a backward Euler approach. In Section 2.4 the interface damage model is incorporated into a three-dimensional finite element model for a centre-cracked GLARE specimen subjected to uniaxial tension. The geometry and boundary conditions are specified, followed by a discussion of the finite element discretisation and the material properties. The numerical results obtained with the model are discussed in Section 2.5, starting with the response of a 'quasi-brittle' GLARE laminate with elastic aluminium layers (where the results are compared to those presented in [62]), followed by the response of a 'ductile' GLARE laminate with elasto-plastic aluminium layers. The failure response is computed for two different types of boundary conditions at the vertical edges of the specimen. The section ends with a study of the effect of the initial crack length on the laminate failure strength, where the results are compared with experiments of de Vries [17]. In Section 2.6 the main analysis results are summarised.

2.2 Formulation of the interface damage model

In the current section the governing equations of the interface damage model are presented. The arrangement and treatment of these equations within a consecutive algorithmic framework can be found in Section 2.3. For cohesive zone models used in 3D solid mechanics analyses, the tractions t_i at the interface modelling the cohesive zone and the relative displacements v_i across the interface consist of three components: $i \in \{1, 2, 3\}$, with the numbers denoting the normal direction and the two tangential directions at the interface, respectively. For convenience,

the tangential directions in the plane of crack propagation are taken parallel (index '2') and perpendicular (index '3') to the direction of crack. The tractions and relative displacements are related by means of a constitutive formulation, which, in the present study on interfacial damage, has the form

$$t_i = (1 - d)C_{ij}v_j - dC_{ij}\delta_{1j}\langle -v_1 \rangle \quad \text{where} \quad i, j \in \{1, 2, 3\}, \quad (2.1)$$

with the damage parameter d bounded as $0 \leq d \leq 1$. Here, $d = 0$ corresponds to the initial, undamaged state, and $d = 1$ to the state at which the integrity of the interfacial material point is fully lost. Further, C_{ij} is the elastic stiffness tensor, given by

$$C_{ij} = K\delta_{ij}, \quad (2.2)$$

with K a stiffness parameter and δ_{ij} the Kronecker delta symbol. Observe from the last term in Eq.(2.1) that crack penetration of two opposite crack faces is avoided, by prescribing these faces to interact elastically in the normal direction of the interface during contact, with the elastic contact stiffness being equal to K . The fact that crack face contact is characterised by a negative value of the normal crack face displacement v_1 is accounted for by the Macaulay brackets $\langle \cdot \rangle$, which are defined as $\langle x \rangle = \frac{1}{2}(x + |x|)$.

During a loading process, the damage in an interfacial material point evolves with deformation, as formally expressed by $d = \hat{d}(\kappa)$ with κ a deformation history variable that is monotonically increasing (since damage is an irreversible process). The specific form of $\hat{d}(\kappa)$ corresponds to the shape of the softening curve of the traction-separation law. In the present study a linear softening law is adopted, as schematised in Figure 2.2, where the onset of damage relates to $\kappa = v^0$ (corresponding to $d = 0$) and the completion of damage is reflected by $\kappa = v^u$ (corresponding to $d = 1$), with v^0 and v^u the equivalent crack face displacements at which damage is considered to be initiated and completed, respectively. Although the softening law may have other forms (e.g., multi-linear, exponentially decaying), the shape of the softening law commonly has a minor influence on the characteristics of the fracture process, especially in the case of ductile fracture [65, 73, 74]; the fracture process is mainly determined by the ultimate traction t^u and the fracture toughness G_c (which equals the area under the

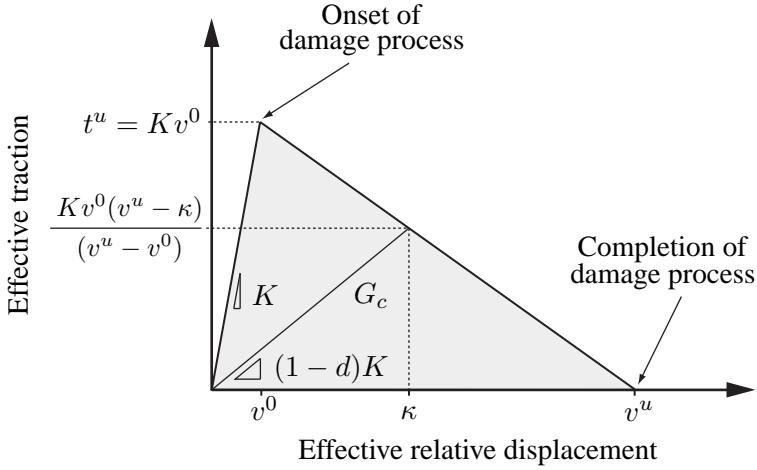


Figure 2.2: Traction-separation law.

traction-separation curve, see Figure 2.2). As further shown in Figure 2.2, for a specific value of κ the equivalent traction is equal to $K v^0 (v^u - \kappa) / (v^u - v^0)$, or, alternatively, in terms of the damage parameter d , equal to $(1 - d)K\kappa$. Equating these two expressions for the traction leads to the following expression for the damage parameter:

$$d = \hat{d}(\kappa) = \frac{v^u (\kappa - v^0)}{\kappa (v^u - v^0)}. \quad (2.3)$$

In contrast to rate-independent damage processes, for *rate-dependent* damage processes the evolution of the damage parameter d is not set by the deformation only, but also by its rate, as described by a specific kinetic law. The actual value of the corresponding history variable κ is then obtained by the inverted form of Eq.(2.3). In the present study, the following rate-dependent kinetic law is proposed:

$$\dot{d} = \begin{cases} \frac{\hat{F}(\lambda, \kappa)}{\eta} & \text{for } \lambda \leq \kappa \text{ and } v^0 \leq \kappa < v^u, \\ 0 & \text{for } 0 \leq \lambda < \kappa \text{ or } \kappa = v^u, \end{cases} \quad (2.4)$$

where η is a relaxation parameter (with dimension of time) and $\hat{F}(\lambda, \kappa)$ is the

damage loading function. In Eq.(2.4), the upper expression reflects the rate of damage when the effective deformation λ exceeds the threshold κ , whereas the lower expression sets the rate of damage equal to zero when (i) the threshold value has not (yet) been reached, (ii) the interfacial material point is in a state of unloading, or (iii) the damage process has completed. The deformation measure λ is taken here as the Euclidean norm of the vector of relative crack face displacements, $\lambda = \|\mathbf{v}\| = \sqrt{v_1^2 + v_{sh}^2}$, with v_{sh} the total shear displacement, $v_{sh} = \sqrt{v_2^2 + v_3^2}$. Furthermore, the loading function has the form

$$\hat{F}(\lambda, \kappa) = \hat{f}(\lambda) - \hat{d}(\kappa) = \frac{v^u(\lambda - v^0)}{\lambda(v^u - v^0)} - \frac{v^u(\kappa - v^0)}{\kappa(v^u - v^0)}, \quad (2.5)$$

where the right expression is obtained by substituting Eq.(2.3) for $\hat{d}(\kappa)$, and choosing the form of $\hat{f}(\lambda)$ to be similar as $\hat{d}(\kappa)$.

The specific form of the kinetic law, Eq.(2.4), is analogous to the form often used in visco-plasticity modelling (see for example [33]), with the equivalent plastic strain rate being replaced by the damage rate and the static yield function by the damage loading function. In the limit of the relaxation parameter going to zero, $\eta \rightarrow 0$, the kinetic law, Eq.(2.4), turns into the rate-independent loading condition, $\hat{F}(\lambda, \kappa) = 0$, which, as can be observed from Eq.(2.5), is identical to $\lambda = \kappa$. Under these circumstances, the loading-unloading conditions are represented by the Kuhn-Tucker relations

$$(\lambda - \kappa)\dot{\kappa} = 0, \quad \lambda - \kappa \leq 0, \quad \dot{\kappa} \geq 0. \quad (2.6)$$

Hence, the present interface damage model can be used for describing both (virtually) rate-independent fracture in the metal layers of GLARE and rate-dependent delamination at the metal-prepreg interfaces, by setting the relaxation parameter η accordingly.

In mixed-mode fracture processes, the equivalent crack face displacements v^0 and v^u appearing in Eq.(2.5) are dependent on the relation between the normal and shear displacements at the interface. As recently proposed by Turon *et al.* [72], this relation may be captured by the following mode-mixity parameter:

$$\beta = \frac{v_{sh}}{v_{sh} + \langle v_1 \rangle}. \quad (2.7)$$

In this definition, pure mode I loading is reflected by $v_{sh} = 0$, and thus by $\beta = 0$, whereas pure shear loading relates to $v_1 = 0$, and thus to $\beta = 1$. Turon *et al.* [72] demonstrated that the functions $v^0 = \hat{v}^0(\beta)$ and $v^u = \hat{v}^u(\beta)$ can be computed adopting a specific mixed-mode failure criterion from linear elastic fracture mechanics. The mixed-mode criterion adopted in the present study is a model regularly used to characterise mixed-mode toughness data for brittle interfacial fracture [43, 44], i.e.,

$$\frac{G_I}{G_{I,c}} + \frac{G_{II}}{G_{II,c}} + \frac{G_{III}}{G_{III,c}} = 1, \quad (2.8)$$

where G_I , G_{II} and G_{III} are the mode I, mode II and mode III energy release rates, and $G_{I,c}$, $G_{II,c}$ and $G_{III,c}$ are the toughnesses under pure mode I, pure mode II and pure mode III loading conditions. For simplicity, the mode II and mode III fracture toughnesses are assumed to have a common value, $G_{sh,c} = G_{II,c} = G_{III,c}$, as a result of which the criterion (2.8) reduces to

$$\frac{G_I}{G_{I,c}} + \frac{G_{sh}}{G_{sh,c}} = 1, \quad (2.9)$$

with $G_{sh} = G_{II} + G_{III}$. Essentially, the above fracture criterion is an extension of the well-known Griffiths' criterion, $G = G_c$, where G is the total energy release rate measured at the crack tip and G_c is the effective fracture toughness (which thus depends on the mode-mixity of the loading). As already mentioned, the fracture toughness G_c is represented by the area under the traction-separation curve in Figure 2.2, and thus can be computed as

$$G_c = \hat{G}_c(\beta) = \frac{1}{2} K \hat{v}^0(\beta) \hat{v}^u(\beta). \quad (2.10)$$

In the limits of pure mode I loading ($\beta = 0$) and pure shear loading ($\beta = 1$), the fracture toughness in Eq.(2.10) respectively reduces to

$$\begin{aligned} G_{I,c} &= \hat{G}_c(\beta = 0) = \frac{1}{2} K v_1^0 v_1^u, \\ G_{sh,c} &= \hat{G}_c(\beta = 1) = \frac{1}{2} K v_{sh}^0 v_{sh}^u, \end{aligned} \quad (2.11)$$

where $v_1^0 = t_1^u/K$ is the displacement at which damage is initiated under pure mode I loading, with t_1^u being the ultimate normal traction, $v_{sh}^0 = t_{sh}^u/K$ is the displacement related to damage initiation under pure shear loading, and v_1^u and v_{sh}^u are the corresponding ultimate displacements at which damage is completed, with the ultimate shear traction t_{sh}^u being computed from the two tangential traction components as $t_{sh}^u = \sqrt{(t_2^u)^2 + (t_3^u)^2}$. In order to find expressions for v^0 and v^u in terms of the mode-mixity β , Griffiths' criterion, $G = G_c$, is incorporated into Eq.(2.9), which leads to

$$\frac{G_I}{G_{I,c}} + \frac{G_{sh}}{G_{sh,c}} = \frac{G}{G_c}. \quad (2.12)$$

This expression can be further developed by writing the total energy release rate as¹ $G = G_I + G_{sh}$ and substituting this form into the right-hand side of Eq.(2.12). In line with this decomposition, the individual crack mode components of the energy release rate are expressed in terms of the relative crack face displacements as $G_I = \gamma v_1^2$ and $G_{sh} = \gamma v_{sh}^2$, with γ a proportionality factor (with dimension of force \times length⁻³) that depends on the stiffness and geometry properties of the configuration under consideration and on the actual position along the crack faces at which the relative crack face displacements are evaluated (commonly measured with respect to the origin of the crack tip, see [43]). Invoking Eq.(2.10), and using the definition of the mode-mixity parameter β , Eq.(2.7), to express the relative normal displacement in terms of the relative shear displacement as $v_1 = v_{sh}(1 - \beta)/\beta$, Eq.(2.12) can be elaborated into an expression for v^u :

$$v^u = \hat{v}^u(\beta) = \frac{2(1 + 2\beta^2 - 2\beta)}{K v^0} \left[\left(\frac{(1 - \beta)^2}{G_{I,c}} \right) + \left(\frac{\beta^2}{G_{sh,c}} \right) \right]^{-1}, \quad (2.13)$$

¹An additive decomposition of the energy release rate into its individual crack mode components is allowed if the stiffness properties of the two elastic bulk materials separated by a propagating, brittle interfacial crack are in agreement with the second Dundur's stiffness mismatch parameter being equal to zero, see [43]. This condition is not met strictly for most of the elastic fracture configurations studied in this chapter. Moreover, the present interface crack model is used in boundary value problems where the bulk materials experience plastic yielding. However, based on heuristic reasoning it may be assumed that the effect of this discrepancy on the computational results remains relatively small.

with $G_{I,c}$ and $G_{sh,c}$ given by Eq.(2.11). An explicit expression for the parameter v^0 can be found by substituting Eqs.(2.11)_{1,2} into Eq.(2.13), replacing v^u , v_1^u and v_{sh}^u by the corresponding initial values v^0 , v_1^0 and v_{sh}^0 , and solving for v^0 . This results in

$$v^0 = \hat{v}^0(\beta) = v_1^0 v_{sh}^0 \sqrt{\frac{1 + 2\beta^2 - 2\beta}{(\beta v_1^0)^2 + ((1 - \beta)v_{sh}^0)^2}}. \quad (2.14)$$

Note from Eqs.(2.13) and (2.14) that the mode-mixity β is indeed the only variable in the expressions for v^u and v^0 (since the other parameters represent interfacial fracture data).

2.3 Time discretisation of the interface damage model

In order to perform finite element simulations with the interface damage model presented in the previous section, the model formulation needs to be discretised in time. Using a backward Euler approach, for each discrete time interval $[t_n, t_{n+1}]$ the model variables in an interfacial integration point are evaluated at time t_{n+1} ($= t_n + \Delta t_{n+1}$) assuming the corresponding values at the previous time step t_n are known. In a displacement-based finite element method, the incremental update at integration point level is governed by the relative displacements \mathbf{v}_{n+1} across the interface. These displacements are provided as input from the global iterative procedure at the system level. With the relative displacements, the deformation measure λ is updated as $\lambda_{n+1} = \hat{\lambda}(\mathbf{v}_{n+1}) = \|\mathbf{v}_{n+1}\|$. This value is compared against the history parameter κ_n computed at the previous time step, where for $\lambda_{n+1} > \kappa_n$ damage is assumed to occur, and for $\lambda_{n+1} \leq \kappa_n$ the response is considered to be elastic (i.e., no damage has occurred (yet), or the integration point is subjected to elastic unloading). The history parameter is initialised as $\kappa_n^0 = v_{n+1}^0 = \hat{v}^0(\beta_{n+1})$, using Eq.(2.14) with $\beta_{n+1} = v_{sh,n+1}/(v_{sh,n+1} + \langle v_{1,n+1} \rangle)$. Subsequently, the damage increment Δd_{n+1} is computed by combining Eqs.(2.4) and (2.5) (with all parameters evaluated at t_{n+1}), with the time discretisation of

the damage rate in accordance with $\Delta d_{n+1} \approx \dot{d}_{n+1} \Delta t_{n+1}$. This leads to

$$\Delta d_{n+1} = \begin{cases} \frac{(f_{n+1} - d_n) \Delta t_{n+1}}{\eta + \Delta t_{n+1}} & \text{for } \lambda_{n+1} > \kappa_n, \\ 0 & \text{for } 0 \leq \lambda_{n+1} \leq \kappa_n. \end{cases} \quad (2.15)$$

where f_{n+1} is given by

$$f_{n+1} = \frac{v_{n+1}^u (\lambda_{n+1} - v_{n+1}^0)}{\lambda_{n+1} (v_{n+1}^u - v_{n+1}^0)}, \quad (2.16)$$

and $v_{n+1}^u = \hat{v}^u(\beta_{n+1})$ is calculated from Eq.(2.13). Formally, the damage process is completed if the damage parameter reaches unity. Correspondingly, in the present algorithm completion of damage is checked by means of the condition: $d_n + \Delta d_{n+1} > 1 - \varepsilon$, where ε is a small positive value ($0 < \varepsilon \ll 1$), introduced here to improve the global numerical convergence behaviour when locally damage has completed. If the above condition holds, the damage process is considered to have finished and, accordingly, the damage parameter is then set equal to the maximum value, $d_{n+1} = 1 - \varepsilon$. Hence, the update of the damage parameter can be concisely formulated as

$$d_{n+1} = \min(d_n + \Delta d_{n+1}, 1 - \varepsilon). \quad (2.17)$$

For any damage value within the range $0 \leq d_{n+1} \leq 1 - \varepsilon$, the traction vector, $\mathbf{t}_{n+1} = \hat{\mathbf{t}}(\mathbf{v}_{n+1}, d_{n+1})$, is computed by substituting the relative displacement vector, \mathbf{v}_{n+1} together with the updated damage variable, $d_{n+1} = \hat{d}(\mathbf{v}_{n+1})$, into Eq.(2.1), which results in

$$t_{i,n+1} = (1 - d_{n+1})K v_{i,n+1} - d_{n+1}K \delta_{1i} \langle -v_{1,n+1} \rangle, \quad i \in \{1, 2, 3\}, \quad (2.18)$$

where use has been made of Eq.(2.2). In addition, the history parameter κ is updated using the inverted form of Eq.(2.3), i.e.,

$$\kappa_{n+1} = \frac{v_{n+1}^0 v_{n+1}^u}{v_{n+1}^u - (v_{n+1}^u - v_{n+1}^0) d_{n+1}}. \quad (2.19)$$

From the above expression, it can be confirmed that completion of damage corresponds to $\kappa_{n+1} = v_{n+1}^u$ (when ignoring the contribution by the small value ε

in Eq.(2.17)). Note that the present time integration procedure can be performed without any iterations, due to the use of the specific damage loading function, Eq.(2.5), in the kinetic law, Eq.(2.4). Alternative, more complex forms of the damage loading function require an iterative time integration procedure at the integration point level, which obviously is computationally more expensive.

The tangent operator necessary for constructing the stiffness matrix at the system level follows from

$$\frac{d\hat{\mathbf{t}}_{n+1}}{d\mathbf{v}_{n+1}} = \frac{\partial \hat{\mathbf{t}}_{n+1}}{\partial \mathbf{v}_{n+1}} + \frac{\partial \hat{\mathbf{t}}_{n+1}}{\partial d_{n+1}} \frac{\partial \hat{d}_{n+1}}{\partial \mathbf{v}_{n+1}}, \quad (2.20)$$

which, with Eq.(2.18), leads to

$$\begin{aligned} \frac{d\hat{t}_{i,n+1}}{dv_{j,n+1}} &= K\delta_{ij} - d_{n+1}K \left(\delta_{ij} + \delta_{1i} \frac{\langle -v_{1,n+1} \rangle}{v_{1,n+1}} \delta_{1j} \right) + \\ &\quad - \frac{\partial \hat{d}_{n+1}}{\partial v_{j,n+1}} K \left(v_{i,n+1} + \delta_{1i} \langle -v_{1,n+1} \rangle \right). \end{aligned} \quad (2.21)$$

Here, the derivative $\partial \hat{d}_{n+1} / \partial \mathbf{v}_{n+1}$ can be determined from Eqs.(2.15) to (2.17) as

$$\frac{\partial \hat{d}_{n+1}}{\partial v_{j,n+1}} = \begin{cases} \frac{v_{n+1}^0 v_{n+1}^u}{\lambda_{n+1}^3 (v_{n+1}^u - v_{n+1}^0)} \frac{\Delta t_{n+1}}{\eta + \Delta t_{n+1}} v_{j,n+1} \left(1 + \frac{\langle -v_{1,n+1} \rangle}{v_{j,n+1}} \delta_{1j} \right) & \text{for } \lambda_{n+1} > \kappa_n \quad \text{and} \quad 0 < d_{n+1} < 1 - \varepsilon, \\ 0 & \text{else,} \end{cases} \quad (2.22)$$

where the multiplication factor $(1 + \delta_{1j} \langle v_{1,n+1} \rangle / v_{j,n+1})$ has been added in the upper expression to account for the fact that the derivative in the normal direction of the interface, $\partial \hat{d}_{n+1} / \partial v_{1,n+1}$, is zero during (elastic) crack face contact. For reasons of simplicity, the extensive terms related to the derivatives $\partial \hat{v}_{n+1}^0 / \partial v_{j,n+1}$ and $\partial \hat{v}_{n+1}^u / \partial v_{j,n+1}$ are ignored in Eq.(2.22). This simplification is acceptable if the mode-mixity β varies rather slowly with deformation, causing these derivatives to remain relatively small. However, for boundary value problems where

the mode of fracture changes abruptly with deformation, additional computations not presented here have shown that the tangent operator given by Eq.(2.22) may induce a drastic collapse in the global convergence rate (i.e., a transition from a quadratic to a quasi-linear convergence rate). Under these circumstances it may be preferential to compute the tangent operator numerically (see [54] for the case of small deformations and [49, 64] for the case of finite deformations), in order to preserve the quadratic convergence rate at the system level and to avoid the analytical determination of the extensive derivatives $\partial \hat{v}_{n+1}^0 / \partial v_{j,n+1}$ and $\partial \hat{v}_{n+1}^u / \partial v_{j,n+1}$.

2.4 Numerical model of a centre-cracked 2/1 GLARE laminate subjected to uniaxial tension

2.4.1 Geometry and boundary conditions

The interface damage model presented in the previous section is used to study mode I fracture and interfacial delamination in a centre-cracked 2/1 laminate subjected to uniaxial tension, see Figure 2.3. The 2/1 lay-up refers to a laminate composed of two aluminium layers sandwiching a single fibre-epoxy layer. Laminates reinforced by glass fibres are commercially known as GLARE. For this material the aluminium and fibre-epoxy layers commonly have thicknesses of 0.3 mm and 0.25 mm, respectively (see for example, [17]), which leads to a total specimen thickness of 0.85 mm. The specimen length is taken as $L = 60$ mm and its width equals $W = 40$ mm. The initial pre-crack at the centre of the specimen is placed across the complete thickness of the two aluminium layers, and has a length of $2a_0 = 0.12 W = 4.8$ mm. The tensile loading is imposed by prescribing a remote normal displacement u^∞ at the top and bottom edges of the laminate, which induces a uniform remote tensile stress σ^∞ in the aluminium layer at short distance from the top and bottom edges. Quasi-static loading conditions are warranted by applying a relatively small nominal strain rate $\dot{u}^\infty / L = 10^{-5} \text{ s}^{-1}$. As demonstrated by experimental and modelling studies on the static and fatigue failure behaviour of centre-cracked laminates [17, 60, 62, 63, 68, 78], under the applied remote tensile loading the initial pre-crack will start to tunnel as a mode I crack

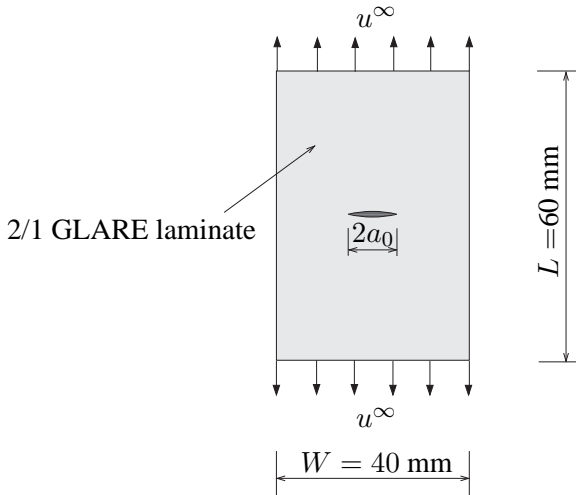


Figure 2.3: Dimensions of a centre-cracked tensile specimen made of 2/1 GLARE. The length of the centre crack is: $2a_0 = 4.8 \text{ mm}$.

through the aluminium sheet, thereby initiating delamination along the interface between the aluminium (material #1) and fibre-epoxy (material #2) layers. The complete fracture mechanism has been sketched in Figure 2.4 (Left), and can be denoted as a *tunneling, doubly-deflected crack* [62]. Since the doubly-deflected cracks in the two outer layers of the 2/1 specimen taken together resemble an H-shape crack, this fracture mechanism is comparable to the failure scenarios depicted in Figure 2.1.

In order to examine how plasticity in the aluminium layer affects the failure characteristics of the specimen, simulations in which the aluminium layer behaves isotropically elastic are compared to simulations where the aluminium is modelled as isotropically elasto-plastic. In both cases the fibre-epoxy layer is modelled as isotropically elastic. This is an acceptable simplification if the internal structure of the fibre-epoxy layer is cross-plyed, i.e., made of two sublayers of 0.125 mm thickness with the uni-directional fibres oriented under 0° and 90° , respectively, see Figure 2.4 (Left), and the elastic mismatch between the fibres and the epoxy is moderate. The assumption of an isotropic fibre-epoxy layer increases the de-

gree of symmetry of the problem, such that only one octant of the actual geometry can be modelled, see Figure 2.4 (Right). This significantly reduces the computational time of the analysis. Furthermore, this simplification allows the present computational results to be compared to results reported by Suiker and Fleck [62], which relate to fracture and delamination processes in lay-ups composed of brittle, isotropic elastic layers. The symmetry of the configuration depicted in Figure 2.4 (Right) is warranted by fixed and roller supports, and by using a customised interface element that relates the interface tractions of the mode I crack in the aluminium (propagating along the horizontal x-y symmetry plane half-way the specimen) to *half* of the relative crack face displacements across the interface.

The effect of the boundary conditions at the right edge of the specimen on the failure response is studied by considering two cases. The first case, referred to as 'BC1', reflects the unconstrained situation, where the normal traction at the right vertical edge of the specimen (i.e., the normal traction in the x-direction) is prescribed as zero. The second case, referred to as 'BC2', reflects a constrained situation, where the normal displacement at the right vertical edge of the specimen (i.e., the displacement in x-direction) is set to zero. For both cases the shear tractions at all specimen boundaries are prescribed to be zero.

2.4.2 Finite element discretisation

The numerical analyses are performed within a large-displacement, small-strain framework, where the aluminium and fibre-epoxy layers are meshed with sixteen-node, iso-parametric solid-like shell elements, with a $2 \times 2 \times 2$ Gauss quadrature [29, 53, 56]. As illustrated in Figure 2.5, these elements have eight nodes at their element corners (indicated by the solid circles '1-8') and eight nodes half-way each element side (indicated by the open circles '9-16'). In addition, they have four internal nodes (indicated by the open squares 'a-d'), which are positioned at the four corners of the mid-surface that is located half-way the element thickness. The internal nodes are used for constructing a linear strain field in the thickness direction (i.e., the ζ -direction) of the element, which remedies the problem of Poisson-thickness locking that characterises conventional volume elements with a high length-to-thickness ratio see [29, 53, 56] for more details. At the plane at

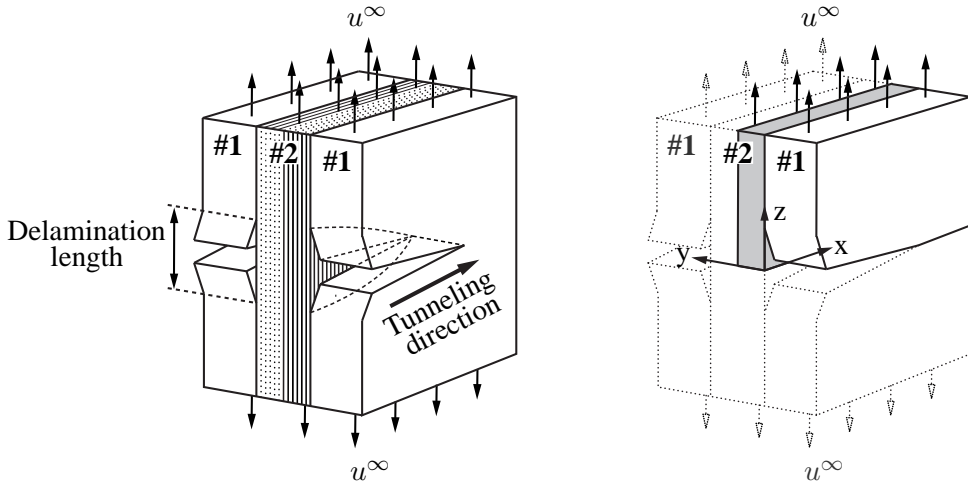


Figure 2.4: Left: Doubly-deflected crack in the two outer layers of a 2/1 GLARE laminate subjected to uniaxial tension (imposed by a remote displacement u^∞). The laminate is composed of two aluminium (material #1) layers sandwiching a single, cross-plyed, fibre-epoxy (material #2) layer. Right: One symmetrical octant of the centre-cracked tensile specimen, used in the numerical simulations.

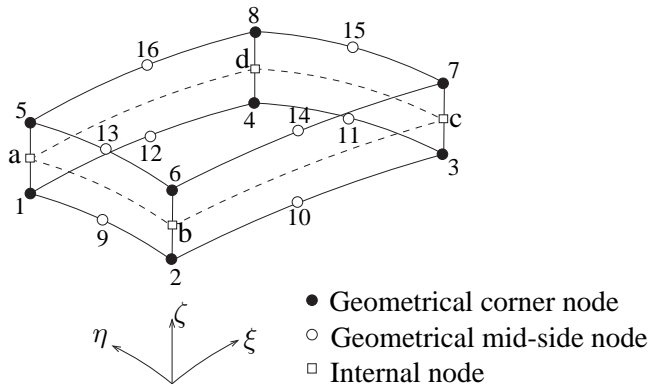


Figure 2.5: Geometry of a sixteen-node, iso-parametric solid-like shell element. The element is composed of sixteen geometrical nodes (indicated by the circles '1-16') and four internal nodes (indicated by the squares 'a-d').

which interfacial delamination between the aluminium layer and the fibre-epoxy layer is expected, the top (or bottom) surface of the solid-like shell element, which is spanned by eight nodes in the $\xi - \eta$ plane, is connected to a sixteen-node interface element, see Detail A in Figure 2.6. This interface element has eight nodes per surface, and is equipped with a 3×3 Newton-Cotes quadrature. The numerical formulation of the geometrically non-linear interface element is based on [57, 58], see also [29]. At the plane along which mode I fracture in the aluminium layer develops, the side surface of the solid-like shell element, which consists of six nodes in the $\eta - \zeta$ (or $\xi - \zeta$) plane, is attached to a twelve-node interface element (which has six nodes per surface), equipped with a 3×2 Newton-Cotes quadrature. The total number of solid-like shell elements used for meshing the aluminium layer and the fibre-epoxy layer is $2 \times 700 = 1400$, see Figure 2.6. Correspondingly, the number of sixteen-node interface elements used for meshing the plane along which delamination is expected equals 700. In addition, the number of twelve-node interface elements used for modelling the plane along which the mode I crack in the aluminium develops is 22. This results into a total number of 2122 elements.

As further illustrated in Figure 2.6, the finite element mesh is relatively fine close to the plane along which the mode I crack propagates, and becomes coarser towards the top edge of the specimen at which the loading is applied. The relatively small interface elements capturing the mode I crack growth and the initial part of the interfacial delamination process are approximately square-shaped, having a size Δ . For the fracture problems studied in [11], convergence of the numerical results upon mesh refinement was observed when the value of Δ was chosen smaller than 4 times the ultimate separation v^u used in the traction-separation law. Accordingly, in the present study the size of the interface elements at the mode I crack tip and at the delamination tip is chosen such that Δ/v^u is approximately equal to 1.5 and 2.5, respectively.

2.4.3 Material properties

The material data used in the numerical model is listed in Table 2.1. The elastoplastic response of the aluminium layers is simulated using a standard J_2 -flow

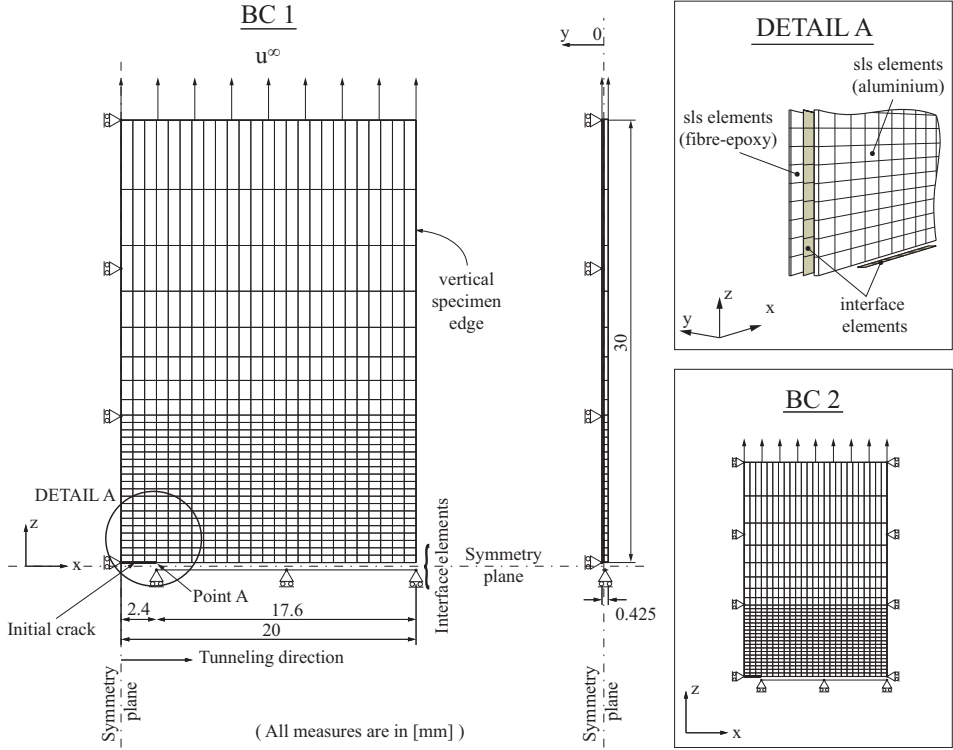


Figure 2.6: Finite element mesh and boundary conditions for the GLARE 2/1 specimen. The case 'BC1' refers to a specimen where the horizontal displacement at the vertical specimen edge is unconstrained, i.e., a traction-free boundary, whereas for the case 'BC2', depicted in the lower right inset, these horizontal displacements are fully constrained. The upper right inset shows the details of the connection between the solid-like shell (sls) elements and the interface elements, close to the initial pre-crack.

theory (Von Mises plasticity), where the yield strength σ_y evolves in accordance with an exponentially-saturating hardening law,

$$\sigma_y = \hat{\sigma}_y(\kappa^p) = \sigma_y^0 + (\sigma_y^u - \sigma_y^0) (1 - \exp(-\xi \kappa^p)). \quad (2.23)$$

Table 2.1: Material properties of a GLARE laminate.

<i>Parameter(s)</i>	<i>Value(s)</i>
Aluminium layer	
Young's modulus	$E = 72$ [GPa]
Poisson's ratio	$\nu = 0.33$ [-]
Initial yield strength	$\sigma_y^0 = 305$ [MPa]
Ultimate yield strength	$\sigma_y^u = 430$ [MPa]
Hardening rate parameter	$\xi = 27$ [-]
Fibre-epoxy layer	
Young's modulus	$E = 32$ [GPa]
Poisson's ratio	$\nu = 0.20$ [-]
Mode I crack in aluminium	
Elastic stiffness	$K = 1 \times 10^8$ [N/mm ³]
Ultimate normal traction (3 cases)	$t_1^u = 430$ [MPa] ($= 1.4\sigma^*$), 610 [MPa] ($= 2.0\sigma^*$), 915 [MPa] ($= 3.0\sigma^*$), with $\sigma^* = 305$ [MPa])
Fracture toughness	$G_{I,c} = 112$ [N/mm]
Relaxation parameter	$\eta = 2 \times 10^{-5}$ [s]
Numerical offset at damage completion	$\varepsilon = 10^{-8}$ [-]
Interfacial delamination	
Elastic stiffness	$K = 1 \times 10^6$ [N/mm ³]
Ultimate normal traction	$t_1^u = 50$ [MPa]
Ultimate shear traction	$t_2^u = t_3^u = 25$ [MPa]
Fracture toughnesses	$G_{I,c} = G_{II,c} = G_{III,c} = 4$ [N/mm]
Relaxation parameter	$\eta = 2 \times 10^{-3}$ [s]
Numerical offset at damage completion	$\varepsilon = 10^{-6}$ [-]

The evolution from the initial yield strength σ_y^0 ($= 305$ MPa) to the ultimate yields strength σ_y^u ($= 430$ MPa) (representing the saturation state) is in correspondence with uniaxial stress-strain data reported in [76] for the aluminium alloy 2024-T3

typically used in GLARE. The yielding saturation state of this type of aluminium is reached at an equivalent plastic strain κ^p of about 15 %, which is captured by setting the hardening rate parameter in Eq.(2.23) as $\xi = 27$ [-]. The effective Young's modulus and the Poisson's ratio of the fibre-epoxy layer are computed by averaging the stiffness values and Poisson's ratios in the fibre-direction and perpendicular to the fibre-direction, as reported in [76]. The dummy elastic stiffness K of the interface elements modelling the mode I crack and the delaminating crack is taken relatively high, such that in the elastic regime the interfacial deformations remain negligibly small. Observe from Table 2.1 that the stiffness value for the delaminating crack is taken a little lower than that of the mode I crack in the aluminium, which has been done in order to optimise the convergence behaviour of the numerical simulations. The value of the mode I fracture toughness, $G_{I,c}$, is determined adopting the value for the critical mode I stress intensity factor $K_{I,c} = 89.6 \text{ MPa}\sqrt{\text{m}}$ reported in Hashagen [29] (which was obtained by calibrating the crack mouth opening displacement and the effective crack length in a centre-cracked aluminium sheet subjected to uniaxial tension), and substituting this value into Irwin's relation, $G_{I,c} = K_{I,c}^2/E$, where E is the Young's modulus of the aluminium. Values for the ultimate normal traction of the mode I crack in the aluminium, t_1^u , have not been widely reported in the literature. In Hashagen [29], the ultimate normal traction was taken approximately 1.3 times higher than the initial yield strength of the aluminium layer. Furthermore, the studies of Tvergaard and Hutchinson [73] and Chen *et al.* [11] showed that the ratio between the ultimate normal traction of the crack and the initial yield strength of the surrounding elasto-plastic bulk material may have a significant influence on the effective crack growth resistance. Correspondingly, in the present analysis the ultimate traction is varied, considering the following three values: $t_1^u = 1.4\sigma^*$, $2.0\sigma^*$ and $3.0\sigma^*$, with the reference stress taken as $\sigma^* = 305 \text{ MPa}$ (which equals the initial yield strength σ_y^0 in the elasto-plastic model for the aluminium). The mode I fracture toughness of a delaminating crack is obtained from test data for a 2/1 GLARE specimen subjected to mode I delamination [75]. For simplicity, the mode II and mode III delamination toughnesses are chosen to have the same value as the mode I toughness, so that the effective delamination toughness G_c becomes independent of the mode-mixity. The ultimate tractions for the delaminating crack, t_1^u ,

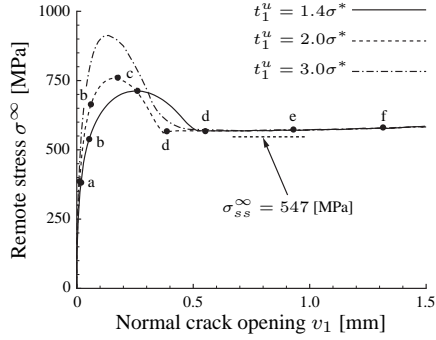
t_2^u and t_3^u , are taken equal to the values reported in Hashagen [29], which were determined from shear and tensile tests on a prepreg material typically used in GLARE. The relaxation parameter η for the mode I crack is taken very small such that under quasi-static loading conditions the crack advancement occurs virtually rate-independently. For the delaminating crack, the relaxation parameter η is chosen slightly larger in order to avoid convergence problems due to crack bifurcations; additional simulations not presented here have shown that in the limit of a truly rate-independent fracture behaviour (i.e., $\eta \rightarrow 0$) the convergence of the present numerical simulations can not be warranted. A detailed analysis on rate effects during interfacial delamination is considered to be a topic for future studies. Finally, both for the mode I crack and the delaminating crack the parameter ε , which represents the (small) numerical offset at damage completion, see Eq.(2.17), is taken equal to the inverse value of the corresponding elastic stiffness K of the interface.

2.5 Modelling results

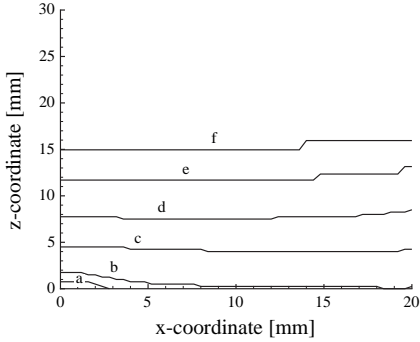
In Table 2.2 an overview of the numerical simulations is given. With the present selection of simulations, the influence of the following four aspects on the effective failure response is studied: (i) The value of the ultimate traction of the mode I crack in the aluminium, (ii) the generation of plasticity in the aluminium layers, (iii) the type of boundary conditions at the vertical specimen edge, and (iv) the initial crack length.

2.5.1 2/1 lay-up with elastic aluminium layers

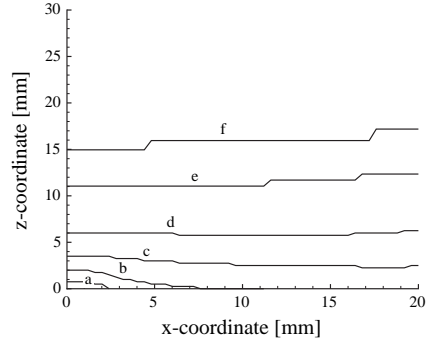
For the case where the aluminium layer behaves elastically, Figure 2.7(a) depicts the remote stress in the aluminium layer (evaluated at the top of the laminate, near the horizontal edge at which the loading is applied) plotted against the normal opening of the mode I crack in the aluminium (measured at the tip position of the initial pre-crack, as represented by point A in Figure 2.6) for three different values of the ultimate normal traction, t_1^u , of the mode I crack (as listed in Table 2.1). The characters 'a-f', which indicate different deformation stages, correspond to



(a) Normal opening v_1 of the mode I crack in the aluminium (measured at point A, see Figure 2.6) versus the remote stress σ^∞ in the aluminium layer, for three different values of the ultimate normal traction t_1^u of the mode I crack in the aluminium. The horizontal, dashed line indicates the steady-state remote stress $\sigma_{ss}^\infty = 547$ MPa computed with Eq.(2.24), and the characters 'a-f' indicate different deformation stages during the loading process.



(b) Delamination profiles for deformation stages 'a-f' (see Figure 2.7(a)), for the case where the ultimate traction of the mode I crack in the aluminium is $t_1^u = 1.4\sigma^*$ ($= 430$ MPa). The x- and z-coordinates relate to the coordinate system in Figure 2.6.



(c) Delamination profiles for deformation stages 'a-f' (see Figure 2.7(a)), for the case where the ultimate traction of the mode I crack in the aluminium is $t_1^u = 2.0\sigma^*$ ($= 610$ MPa). The x- and z-coordinates relate to the coordinate system in Figure 2.6.

Figure 2.7: Failure response for a 2/1 lay-up with *elastic* aluminium layers.

Table 2.2: Overview of the simulations, which are characterised by variations of the boundary conditions, BC1 and BC2 (see Figure 2.6), different values of the ultimate mode I traction t_1^u of the mode I crack in the aluminium, different lamellae properties, and a different relative initial crack length $2a_0/W$.

	$t_1^u = 1.4\sigma^*$	$t_1^u = 2.0\sigma^*$	$t_1^u = 3.0\sigma^*$
Aluminium elastic and fibre-epoxy elastic	BC1 & BC2 $\frac{2a_0}{W} = 0.12$	BC1 $\frac{2a_0}{W} = 0.12$	BC1 $\frac{2a_0}{W} = 0.12$
Aluminium elasto-plastic and fibre-epoxy elastic	BC1 & BC2 $\frac{2a_0}{W} = 0.12$ $= 0.28$ $= 0.48$	BC1 $\frac{2a_0}{W} = 0.12$	BC1 $\frac{2a_0}{W} = 0.12$

the delamination profiles in Figures 2.7(b) and c for the cases where the ultimate traction of the mode I crack is $t_1^u = 1.4\sigma^*$ and $t_1^u = 2.0\sigma^*$, respectively. Since the delamination evolution for the case with $t_1^u = 3.0\sigma^*$ looks similar to that of the case with $t_1^u = 2.0\sigma^*$ (with the only difference being a somewhat stronger delamination development during the initial loading stage), the former case has not been visualised. From Figure 2.7(a) it can be observed that the remote stress initially increases, subsequently reaches a maximum value, then decreases (thus representing an unstable, softening response) and finally asymptotes to a (residual) stress level that remains approximately constant under continuing crack opening. Clearly, the value of the maximum remote stress is higher for a higher value of the fracture strength t_1^u of the aluminium, i.e., $\sigma_{max}^\infty = 720, 760$ and 913 MPa for $t_1^u = 1.4\sigma^*, 2.0\sigma^*$ and $3.0\sigma^*$, respectively. The fact that the local ultimate traction influences the remote stress indicates that the size of the fracture process zone of the tunneling crack can *not* be ignored with respect to its length and/or the total specimen width. If this would be the case, the crack would be of the Griffith type, where the remote stress only depends on the local toughness characteristics of the crack [43]. However, due to the crack bridging behaviour by the fibre-epoxy layer, the size of the process zone of the tunneling crack is significant. A more detailed

discussion on the size of the process zone of the aluminium crack will follow later in this section.

The delamination profiles in Figures 2.7(b) and (c) are obtained by graphically connecting the integration points in which the damage d has just exceeded the value of 0.99 (which thus is close to the maximum damage value $d = 1$). The x - and z -coordinates used for denoting the location of the profiles are in correspondence with the coordinate system depicted in Figure 2.6, with the origin taken at the centre of the initial pre-crack. It can be observed that the differences in delamination growth for $t_1^u = 1.4\sigma^*$ and $t_1^u = 2.0\sigma^*$ are small. In both cases, the delamination profile initially develops with increasing length of the mode I crack in the aluminium (stages 'a' and 'b'), where the maximum delamination takes place at the specimen centre. When the mode I crack reaches the vertical specimen edge, the delamination starts to develop mainly in the vertical direction. After stage 'd' the delamination profile has become almost uniform across the specimen width (only near the free edge the delamination is slightly larger), where the growth process closely approximates the condition of steady-state delamination. In Suiker and Fleck [62] a closed-form expression has been presented for the remote failure stress for steady-state delamination that propagates along the two outermost plies of a uniaxially-loaded, brittle laminate. This expression is derived from the energy difference upstream and downstream of the delamination front, and reads

$$\sigma_{ss}^{\infty} = \sqrt{\frac{4\bar{E}_1 G_c \left((n-2)w_1\bar{E}_1 + (n-1)w_2\bar{E}_2 \right)}{2w_1 \left(n w_1 \bar{E}_1 + (n-1)w_2 \bar{E}_2 \right)}}. \quad (2.24)$$

Here, σ_{ss}^{∞} is the remote stress in the aluminium layer, n is the number of material #1 layers, G_c is the delamination toughness, and w_1 and w_2 are the thicknesses of the material #1 and #2 layers. Further, the stiffness \bar{E}_i is defined by

$$\bar{E}_i = \begin{cases} E_i / (1 - \nu_i^2) & \text{for plane strain} \\ E_i & \text{for plane stress.} \end{cases} \quad (2.25)$$

where E_i and ν_i are the Young's moduli and Poisson's ratios of materials $i = 1$ (aluminium) and 2 (fibre-epoxy). During uniform, steady-state delamination the

laminates approaches a *plane-stress* condition, since the right edge of the specimen is traction-free, in accordance with the boundary conditions of case BC1 depicted in Figure 2.6. Substitution of the material parameters listed in Table 2.1 into Eq.(2.24), with the delamination toughness taken as $G_c = 4$ N/mm (recall that the effective delamination toughness is independent of the mode-mixity and thus equals the toughness value of the individual fracture modes), and the number of aluminium layers as $n = 2$ (in correspondence with a 2/1 lay-up), for a plane-stress condition leads to a remote stress of $\sigma_{ss}^\infty = 547$ MPa. This stress value, which is represented in Figure 2.7(a) by a horizontal, dashed line, is in close agreement with the residual strength following from the numerical analyses.

As illustrated by Eq.(2.24), the residual strength during steady-state delamination mainly depends on the delamination toughness G_c , and is independent of the aluminium fracture strength t_1^u . The latter aspect can also be observed from Figures 2.7(a), (b) and (c), which illustrate that at stages 'e' and 'f' both the $\sigma^\infty - v_1$ response and the delamination profiles are virtually identical for the different fracture strengths t_1^u . The brittle, almost rate-independent behaviour of the delamination process is further confirmed by the appearance of a relatively small process zone at the delamination tip, which actually can be ignored with respect to the specimen length L .

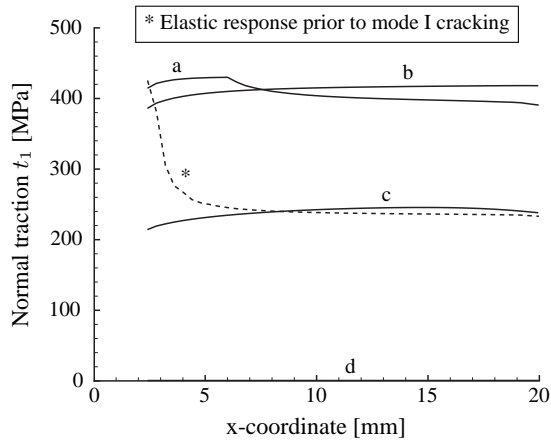
The mode-mixity during steady-state delamination may be evaluated in accordance with the definition given by Eq.(2.7). An alternative measure for the mode-mixity, typically used in linear elastic fracture mechanics [43], is

$$\psi = \tan^{-1} \left(\frac{\sigma_{zy}(r)}{\sigma_{yy}(r)} \right) \Bigg|_{r=l}, \quad (2.26)$$

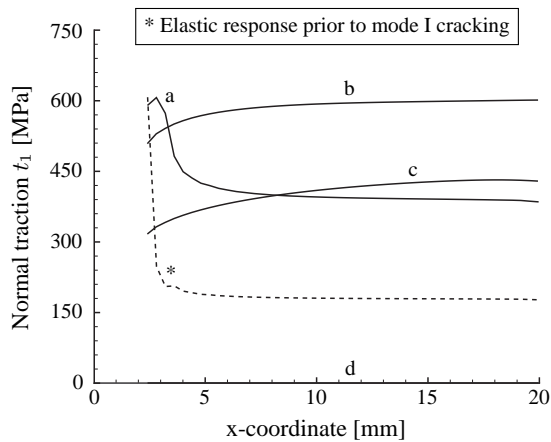
which is based on the shear (σ_{zy}) and normal (σ_{yy}) stresses evaluated at a specified horizontal distance $r = l$ ahead of the crack (or delamination) tip. Note that the definition, Eq.(2.26), assumes that the crack propagates in the z -direction along a plane separating two (possibly dissimilar) bulk materials, with the normal to the cracking plane pointing in the y -direction, where pure mode I conditions correspond to $\psi = 0^\circ$, and pure mode II conditions relate to $\psi = 90^\circ$. In cohesive zone modelling there is no standard procedure to identify the crack tip from a traction-separation law. However, a definition regularly used is based on relating

the crack tip to the point at which the interface traction reaches the peak value t^u [59], which is consistent with the experimental observation that micromechanical processes are not only active ahead of the crack tip, but also in the wake of the crack tip [41]. With this definition, the present numerical results show that during steady-state delamination the mode-mixity, Eq.(2.26), for the case $t_1^u = 1.4\sigma^*$ varies between a minimum value $\psi = 31^\circ$ measured at a small distance ahead of the crack tip, and a maximum value $\psi = 90^\circ$ measured exactly at the crack tip. The maximum value reflects a purely mode II condition. This condition is reached since the crack faces at the crack tip are in contact, as a result of which the mode I contribution vanishes. In Suiker and Fleck [62], the mode-mixity for the case of steady-state delamination in a brittle, uniaxially-loaded 2/1 laminate with a stiffness mismatch of $\bar{E}_2/\bar{E}_1 \approx 0.4$ (which is in correspondence with the elastic parameters of the aluminium and fibre-epoxy layers presented in Table 2.1) has been measured as $\psi \approx 54^\circ$, where the distance l has been arbitrarily specified as the semi-width of the mode I crack in the aluminium, $l = 0.15$ mm. Obviously, this value falls within the range $31^\circ < \psi < 90^\circ$ following from the present numerical analyses. In the wake of the crack tip, the mode-mixity in the present simulations varies between a value $\psi = 90^\circ$ measured exactly at the crack tip and a value $\psi = 85^\circ$ measured when the damage is close to unity, $d \approx 1$, and the adherence between the crack faces is virtually lost. Hence, it may be concluded that in the wake of the crack tip the failure process is mode II dominated. For the cases with a higher maximum traction, $t_1^u = 2.0\sigma^*$ and $t_1^u = 3.0\sigma^*$, the mode-mixities ahead and behind the crack tip have similar ranges, with the main difference being that the minimum value ahead of the crack tip is somewhat larger, i.e., $\psi = 38^\circ$ and $\psi = 40^\circ$ for $t_1^u = 2.0\sigma^*$ and $t_1^u = 3.0\sigma^*$, respectively.

The traction profile of the mode I crack in the aluminium is plotted in Figure 2.8(a) ($t_1^u = 1.4\sigma^*$) and Figure 2.8(b) ($t_1^u = 2.0\sigma^*$) across the complete specimen width, during various deformation stages of the loading process. The curve indicated by an asterisk, '*', represents the elastic response of the interface (plotted by a dashed line) prior to cracking (i.e., before the ultimate traction t_1^u is reached at the tip of the initial pre-crack), while the curves 'a-d', which relate to the deformation stages 'a-d' indicated in Figure 2.7, correspond to a mode I crack developing in the aluminium. At deformation stage 'a', the integration points next



(a) Case where the ultimate traction of the mode I crack is $t_1^u = 1.4\sigma^*$ (= 430 MPa).



(b) Case where the ultimate traction of the mode I crack is $t_1^u = 2.0\sigma^*$ (= 610 MPa).

Figure 2.8: Normal traction t_1 of the mode I crack tunneling in the *elastic* aluminium layer, evaluated across the specimen width, at various deformation stages. The curve '*' refers to an elastic interfacial response and the curves 'a-d' (which correspond to the deformation stages 'a-d' indicated in Figure 2.7(a)) reflect the fracture process.

to the initial pre-crack have just entered the softening regime, while the integration points at larger distance from the pre-crack still have not reached the ultimate traction t_1^u and therefore respond elastically. During deformation stages 'b' and 'c' all integration points across the specimen width have reached the softening regime. Note that during softening the tractions vary only weakly in the x-direction, such that the size of the process zone of the aluminium crack substantially exceeds the specimen width. As expected, close to the pre-crack the variation in the softening profile is slightly larger for a larger ultimate traction t_1^u , indicating that the fracture process occurs a little less spread out. Finally, at stage 'd' all integration points across the specimen width have reached the end of the softening regime, and the crack faces of the aluminium crack have become fully separated.

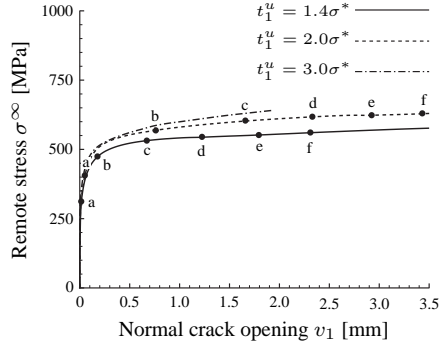
During the final phase of the crack tunneling process (i.e., between stages 'c' and 'd'), significant delamination has developed, see Figures 2.7(b) and (c), where the effective response of the laminate has become unstable, see Figure 2.7(a). In the study of Suiker and Fleck [62] on laminates subjected to uniaxial tension, this unstable tunneling mechanism was named 'mechanism 3', see Figure 2.1. Although the study in [62] relates to an 'ideally brittle' laminate of infinite size, where the size of the process zone of the tunneling crack is equal to zero, the typical features of mechanism 3 thus also are observed in a 'quasi-brittle' laminate where the tunneling crack is characterised by a process zone of substantial length. Essentially, the appearance of mechanism 3 can be explained from the specific material parameters that characterise the 2/1 GLARE laminate, i.e., the elastic stiffness of the fibre-epoxy layer, which, as already mentioned, is about 0.4 times smaller than the elastic stiffness of the aluminium layer, and the ratio between the delamination toughness and the mode I fracture toughness, which has a rather low value of 0.04, see Table 2.1. The analyses performed by Suiker and Fleck [62] confirm that for these material parameters 'mechanism 3' is indeed the operative failure mechanism during crack tunneling in a 2/1 laminate. This failure mechanism map further indicates that the stiffness mismatch between the fibre-epoxy layer and the aluminium layer has a moderate influence on the appearance of this specific fracture mechanism, and that it is mainly determined by the relatively low toughness for interfacial delamination. In fact, it is shown that the delamination during crack tunneling remains absent if the delamination toughness becomes

larger than the toughness for mode I fracture in the aluminium. For such a relatively high delamination toughness the tunneling crack becomes stable and of the pure mode I type (i.e., 'mechanism 1' in Figure 2.1), in correspondence with a remote, steady-state tunneling stress that is about three to four times larger than that obtained for the present delamination toughness. Obviously, this conclusion holds as long as the aluminium layers do not deform plastically. The influence of plasticity in the aluminium on the effective failure response of the laminate is investigated in the subsequent section.

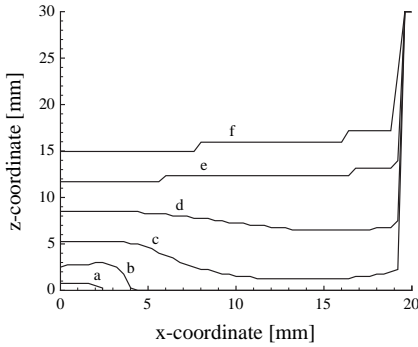
2.5.2 2/1 lay-up with elasto-plastic aluminium layers

In Figure 2.9(a) the remote stress in the aluminium layers is plotted versus the normal opening of the mode I crack in the elasto-plastic aluminium layers. It can be observed that a higher fracture strength t_1^u of the aluminium leads to a higher remote stress, i.e., at a crack opening $v_1 = 1.9$ mm the remote stress in the aluminium equals $\sigma^\infty = 557, 611$ and 642 MPa for $t_1^u = 1.4\sigma^*, 2.0\sigma^*$ and $3.0\sigma^*$, respectively. For the case with the highest aluminium fracture strength, $t_1^u = 3.0\sigma^*$, at $v_1 = 1.9$ mm the continuum elements close to the crack tip have become strongly distorted, which is due to the generation of substantial plastic deformations in these elements. Consequently, at this stage the numerical procedure fails to converge. Although it is expected that this problem can be overcome by further decreasing the size of the elements near the crack tip, this strategy has not been explored in more detail due to the already large computational times of the present simulations (i.e., the solid-like shell elements used in the numerical model are computationally expensive). Note that the curves depicted in Figure 2.9(a) do not show a softening branch, which is in contrast to the effective response of a lay-up with elastic aluminium layers, see Figure 2.7(a). Hence, it may be concluded that the dissipation in the plastic zone ahead of the crack in the aluminium stabilizes the effective failure response of the laminate. For a larger fracture strength t_1^u of the aluminium, the plastic zone, and thus the dissipation in this zone, becomes larger, as a result of which the failure response becomes more stable, see Figure 2.7(a).

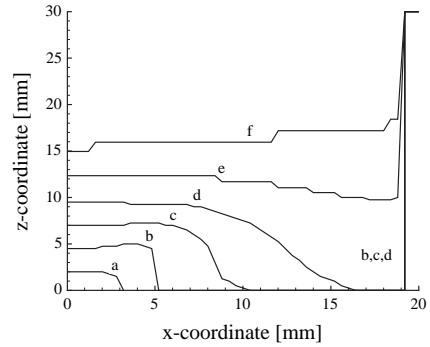
The delamination profiles for the deformation stages 'a-f' indicated in Fig-



(a) Normal opening v_1 of the mode I crack in the aluminium (measured at point A, see Figure 2.6) versus the remote stress σ^∞ in the aluminium layer, for three different values of the ultimate normal traction t_1^u of the mode I crack in the aluminium. The characters 'a-f' indicate different deformation stages during the loading process.



(b) Delamination profiles for deformation stages 'a-f' (see Figure 2.9(a)), for the case where the ultimate traction of the mode I crack in the aluminium is $t_1^u = 1.4\sigma_y^0 (= 1.4\sigma_y^0 = 430 \text{ MPa})$. The x- and z-coordinates relate to the coordinate system in Figure 2.6.

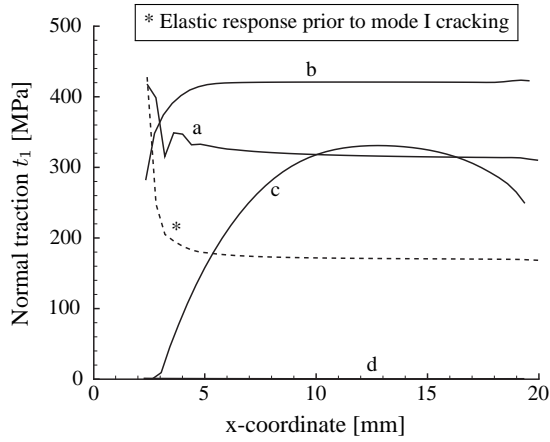


(c) Delamination profiles for deformation stages 'a-f' (see Figure 2.9(a)), for the case where the ultimate traction of the mode I crack in the aluminium is $t_1^u = 2.0\sigma_y^0 (= 2.0\sigma_y^0 = 610 \text{ MPa})$. The x- and z-coordinates relate to the coordinate system in Figure 2.6.

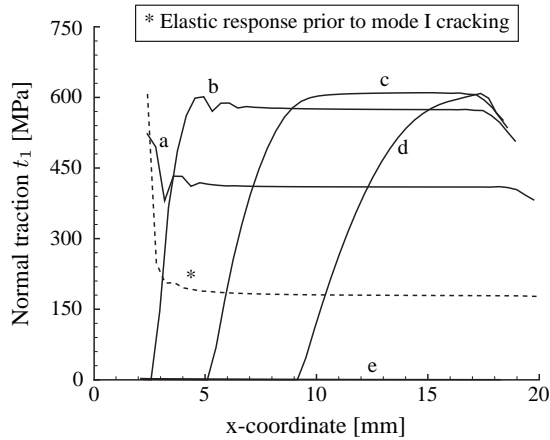
Figure 2.9: Failure response for a 2/1 lay-up with *elasto-plastic* aluminium layers.

ure 2.9(a) are plotted in Figures 2.9(b) ($t_1^u = 1.4\sigma^*$) and 2.9(c) ($t_1^u = 2.0\sigma^*$). Apparently, during crack tunneling the delamination front for a specimen with elasto-plastic aluminium layers is much steeper than for a specimen with elastic aluminium layers, see Figures 2.7(b),(c). In addition, plastic deformations in the aluminium layer induce substantial free-edge delamination along the vertical specimen edge. Essentially, near the free edge the plastic deformations in the aluminium layer increase the mismatch in deformation with the fibre-epoxy layer that wants to contract laterally. This gives rise to the development of stress concentrations at the interface between the two layers, which are relaxed through the appearance of free-edge delamination. When the delamination has fully developed and is approximately uniform across the specimen width (i.e., stage 'f'), for the case $t_1^u = 1.4\sigma^*$ the mode-mixity, Eq.(2.26), ahead of the crack tip on average varies between a value $\psi = 60^\circ$ measured at a small distance from the crack tip and a value $\psi = 90^\circ$ measured exactly at the crack tip. In the wake of the crack tip the mode-mixity varies between a value $\psi = 90^\circ$ measured at the crack tip and a value $\psi = 86^\circ$ measured at a position where damage has approached unity, $d \approx 1$. The latter variation in mode-mixity is similar to that for the case of a 2/1 laminate with elastic aluminium layers, and indicates that the fracture process in the wake of the crack is mode II dominated. Note that the variation of the mode mixity ahead of the crack tip is somewhat smaller than for the 2/1 laminate with elastic layers, from which it may be concluded that the generation of plasticity in the aluminium reduces the mode I contribution to delamination. Furthermore, as for the case of a specimen with elastic layers, the influence of the value of the ultimate traction t_1^u on the mode-mixity is relatively small.

The evolution of the normal traction of the mode I crack in the aluminium has been plotted in Figures 2.10(a) ($t_1^u=1.4\sigma^*$) and b ($t_1^u=2.0\sigma^*$), for all integration points across the specimen width. The characters 'a-e' correspond to the deformation stages 'a-e' indicated in Figure 2.9(a). Comparing the profiles in Figures 2.10(a) and (b) shows that ahead of the crack tip the increase in traction with distance is stronger for a higher ultimate traction, t_1^u , of the aluminium crack. Correspondingly, the length of the fracture process zone, which relates to the distance between the integration point in which all traction is lost and the integration point that has just reached the maximum traction value t_1^u , decreases



(a) Case where the ultimate traction of the tunneling mode I crack is $t_1^u = 1.4\sigma^* (= 1.4\sigma_y^0 = 430 \text{ MPa})$.



(b) Case where the ultimate traction of the tunneling mode I crack is $t_1^u = 2.0\sigma^* (= 2.0\sigma_y^0 = 610 \text{ MPa})$.

Figure 2.10: Normal traction t_1 of the mode I crack tunneling in the *elasto-plastic* aluminium layer, evaluated across the specimen width, at various deformation stages. The curve '*' refers to an elastic interfacial response and the curves 'a-e' (which correspond to the deformation stages 'a-e' indicated in Figure 2.9(a)) reflect the fracture process.

if the ultimate traction t_1^u becomes larger. A similar result was found by Tvergaard and Hutchinson [73] for a purely mode I crack propagating in an elasto-plastic medium. In addition, it can be noticed that the fracture process zone for a laminate with elasto-plastic aluminium layers is considerably shorter than for a laminate with elastic aluminium layers, see Figures 2.7(b) and (c). Essentially, a compliant, elasto-plastic aluminium layer is less constrained to deformation, and therefore induces a shorter fracture process zone than a stiff elastic aluminium layer. Combining Figures 2.10(a) and (b) with Figures 2.9(b) and (c), it can be observed that a tunneling crack with a higher fracture strength and a shorter fracture process zone (i.e., the case with $t_1^u = 2.0\sigma^*$) is characterised by a steeper delamination front near the crack tip. In addition, a tunneling crack with a higher fracture strength and a shorter fracture process zone requires the application of more external work in order for the crack tip to reach the vertical specimen edge and to evolve into an (almost) uniform delamination pattern. Accordingly, at the level of uniform delamination (stage 'f'), the normal crack opening v_1 and the remote failure strength σ^∞ are larger for a higher fracture strength t_1^u of the aluminium, see Figure 2.9(a). Recall that this effect has *not* been observed for the 2/1 laminate with elastic aluminium layers; the strength and deformation characteristics at uniform delamination are independent of the fracture strength of elastic aluminium layers, see stages 'e' and 'f' in Figures 2.7(a), (b) and (c) and Eq.(2.24). It is further interesting to notice that during uniform delamination the remote strength for a laminate containing elasto-plastic aluminium layers may be somewhat higher than for a laminate containing elastic aluminium layers, especially for higher values of the aluminium fracture strength t_1^u , see Figures 2.9(a) and 2.7(a). Hence, the plastic deformation history developed during crack tunneling then provides a positive contribution to the final residual strength of the laminate specimen.

2.5.3 Influence of boundary conditions on failure response

In accordance with Figure 2.6 and Table 2.2, the effect of the boundary conditions at the right specimen edge on the effective failure response is studied by comparing the cases BC1 (unconstrained boundary) and BC2 (horizontally constrained boundary), using $t_1^u = 1.4\sigma^*$ in the traction separation law for the aluminium

crack. In Figure 2.11 the remote stress in the aluminium layer is plotted against the normal crack opening in the aluminium (measured at point A, see Figure 2.6), for the cases where the aluminium layer behaves elastically (Figure 2.11(a)) and elasto-plastically (Figure 2.11(b)). For a specimen with elastic aluminium layers the remote failure response is initially similar for both types of boundary conditions. However, when the crack has tunnelled across the complete specimen width and uniform delamination starts to develop, the remote stress related to the constrained boundary, BC2, becomes somewhat larger than for the unconstrained boundary, BC1. Essentially, the boundary conditions BC1 then approach a plane-stress condition and the boundary conditions BC2 approach a plane-strain condition. The corresponding remote stresses respectively are $\sigma_{ss}^{\infty} = 547$ MPa and $\sigma_{ss,*}^{\infty} = 562$ MPa, as computed with Eqs.(2.24) and (2.25) using the numerical values in Table 2.1. Figure 2.11(a) illustrates that these values are in close agreement with the numerical results.

As shown in Figure 2.11(b), the difference in failure response for the two boundary conditions becomes negligible when plastic deformations develop in the aluminium. The delamination patterns corresponding to case BC2 are similar to those of case BC1 (see Figures 2.7 and 2.9 for lay-ups with elastic aluminium layers and elasto-plastic aluminium layers, respectively), and therefore are not presented here. The only difference between the delamination patterns for the two cases is that for case BC2 free-edge delamination remains absent due to the constraint of the horizontal displacement of the right specimen edge.

2.5.4 Effect of initial crack length on failure strength

In this section the effect of the initial crack length on the overall laminate strength is examined. In addition to the configuration depicted in Figure 2.3, for which the initial crack length is relatively small, $2a_0 = 0.12W$, samples with a larger initial crack length are considered, i.e., $2a_0 = 0.28W$ and $0.48W$, for the case where $t_1^u = 1.4\sigma^*$ and the aluminium layers behave elasto-plastically, see also Table 2.2. The results of the computations are illustrated in Figure 2.12, where the remote gross stress $\bar{\sigma}^{\infty}$ of the laminate is plotted against the relative initial crack size $2a_0/W$. The gross stress is computed as the weighted average of the remote

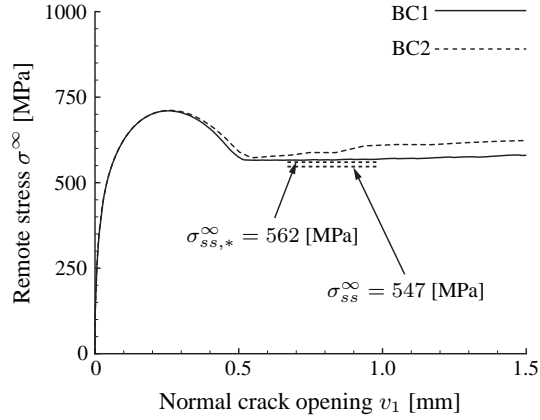
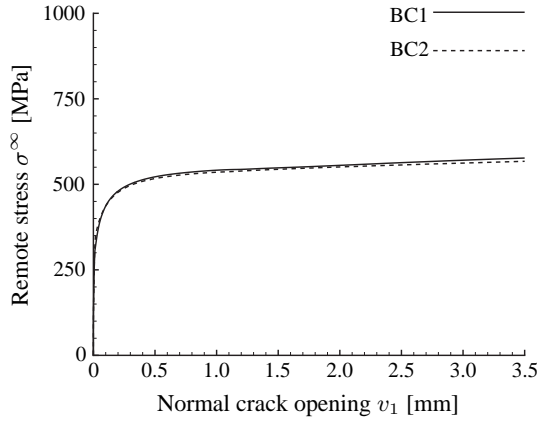
(a) 2/1 lay-up with *elastic* aluminium layers.(b) 2/1 lay-up with *elasto-plastic* aluminium layers.

Figure 2.11: Normal opening v_1 of the mode I crack in the aluminium (measured at point A, see Figure 2.6) versus the remote stress σ^∞ in the aluminium, for a laminate with an *unconstrained* right specimen edge (BC1) and a *horizontally constrained* right specimen edge (BC2), see Figure 2.6. The ultimate traction for the mode I crack in the aluminium is $t_1^u = 1.4\sigma^*$ ($= 430$ MPa). The horizontal, dashed lines in Figure 2.11(a) indicate the steady-state remote stress computed with Eqs.(2.24) and (2.25), which reflects a *plane stress* condition (with $\sigma_{ss}^\infty = 547$ MPa) for the case BC1 and a *plane-strain* condition (with $\sigma_{ss,*}^\infty = 562$ MPa) for the case BC2.

stresses over the total thickness of the laminate, and is evaluated when somewhere in the prepreg layer the axial strain becomes equal to the fracture strain of 4.7 % (as reported in [17]). The computations show that this strain value is first reached in the wake of the aluminium crack, close to the centre of the specimen. It is assumed that at the prepreg fracture strain the gross stress reaches its maximum, and is going to drop under continued loading due to (substantial) fibre failure. With this assumption, the computed gross stress may be considered as the *residual strength* of the centre-cracked specimen, which is typically defined as the ultimate static strength in the presence of damage [17]. Figure 2.12 illustrates that the calculated maximum gross stress drops with about 100 MPa when the initial crack length is increased from $2a_0 = 0.12W$ to $0.48W$. Furthermore, the numerical predictions appear to be in good correspondence with the residual strengths measured experimentally by de Vries [17] for centre-cracked 2/1 GLARE laminates with widths ranging from 100 mm to 400 mm. In the experiments the initial crack is generated through the application of a fatigue load with constant amplitude, which results in a residual strength that is about 200 MPa higher than when the initial crack is generated by a saw cut [17]. In spite of the good correspondence between the model and the experiments, it should be mentioned that the fibre-epoxy layers of the tested 2/1 laminates are unidirectional with the fibres oriented in the loading direction, which differs from the cross-plyed fibres-epoxy layers considered in the numerical simulations. Furthermore, the laminate widths used in the experiments are somewhat larger than that in the simulation (i.e., $W = 40$ mm, see Figure 2.3). These two discrepancies are expected to lead to, respectively, (relatively small) under- and overpredictions of the experimental strengths, as can be concluded from experimental variation studies on laminates with alternative lay-ups [17]. A more detailed analysis of the effects of fibre-orientation and specimen width on the overall laminate failure response is a topic for future modelling studies.

2.6 Summary of results and concluding remarks

Three-dimensional numerical simulations have been performed on a centre-cracked 2/1 GLARE laminate subjected to uniaxial tension. The laminate is com-

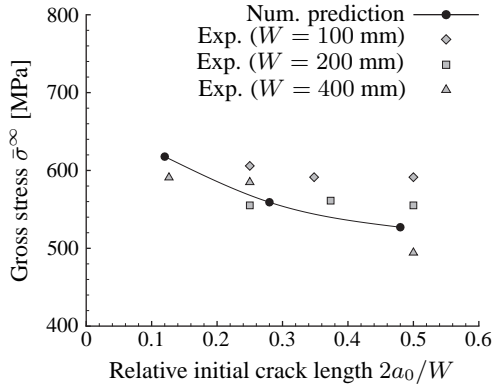


Figure 2.12: Maximum gross stress $\bar{\sigma}^\infty$ of the centre-cracked laminate specimen versus the relative initial crack length $2a_0/W$. The experimental values are taken from de Vries [17]

posed of two aluminium layers sandwiching a cross-plyed fibre-epoxy layer. The fracture and delamination characteristics are simulated with an interface model, in which the mode-mixity is derived from an energy criterion typically used in linear elastic fracture mechanics studies. The response for a lay-up with elastic aluminium layers shows that during the final phase of the loading process the delamination becomes virtually uniform across the specimen width, reaching a steady state. The corresponding residual failure strength of the laminate strongly depends on the delamination toughness. These results appear to be in close correspondence with those obtained by Suiker and Fleck [62] for a uniaxially-loaded laminate composed of brittle, elastic layers. During the initial, crack nucleation phase, which can not be simulated with the model presented in [62], a higher fracture strength of the aluminium leads to a higher ultimate failure strength of the laminate. The transition from the deformation stage at which the ultimate failure strength is reached to the deformation stage at which the residual failure strength is reached is characterised by an unstable response, in correspondence with 'mechanism 3' depicted in Figure 2.1. This unstable behaviour vanishes when the aluminium is able to deform plastically. Furthermore, both during the phases of crack tunneling and uniform delamination, the strength of the laminate

with elasto-plastic aluminium layers strongly depends upon the fracture strength of the aluminium. Essentially, a higher aluminium fracture strength provides the aluminium crack with a shorter fracture process zone and a steeper delamination front at the crack tip, which leads to a higher effective failure strength of the laminate. In addition, the final residual strength at uniform delamination may be higher than for a laminate composed of elastic aluminium layers, especially at higher values of the aluminium fracture strength. When the horizontal displacements at the vertical boundaries of the laminate specimen are unconstrained, the generation of plasticity in the aluminium layers induces free-edge delamination. The free-edge delamination remains absent when the horizontal displacements at these boundaries are fully constrained. In addition, the gross strength drops with increasing initial crack length $2a_0$, and shows to be in good correspondence with the experimental values reported in [17].

In the discussion of the simulation results, the effect of several length scales on the overall failure response of the laminate has been addressed and analysed, i.e., the size of the fracture and delamination process zones, the size of the plastic zone ahead of the mode I crack tip and the size of initial crack length. However, the interactive effect on the response by these length scales and higher-scale, geometrical lengths, such as the width of the laminate, has not been studied in detail. This would require the variation of the laminate specimen size, which is kept constant in the present analyses. More information about the interaction between material length scales and geometrical length scales and their effect on the global failure strength, as often conveniently described by means of so-called *size-effect laws*, can be found in the textbook of Bažant and Planas [6] and references therein.

The present interface damage model has proven to behave robustly and accurately in the numerical boundary value problems studied in this chapter. It is emphasised that the excellent numerical performance of the interface damage model is not limited to the specific type of boundary value problems examined here, as it will be shown in the forthcoming chapters.

Micromechanical study of off-axis failure behaviour of fibre-epoxy systems

3.1 Introduction

The macroscopic tensile failure response of fibre-metal laminates and fibre-reinforced composites, as often characterised by mechanisms such as transverse matrix cracking and interfacial delamination, at the microscale typically is determined by a combination of various complex failure modes, such as fibre debonding, epoxy cracking, and fibre pull-out. For optimising the design and manufacturing of these materials, it is important to understand these failure modes in detail, which requires the development of advanced numerical models that can simulate the microscale failure behaviour in a stable, robust and accurate fashion. The present chapter focuses on the numerical simulation of the off-axis failure behaviour of unidirectional fibre-epoxy systems, which is characterised by two

out of the three microscale failure modes mentioned above, namely fibre debonding and epoxy cracking. The mechanisms of fibre debonding and epoxy cracking are modelled in a discrete fashion, using interface elements equipped with the cohesive zone model presented in Section 2.2. To allow for arbitrary, complex fracture patterns that develop as result of crack branching and crack coalescence, interface elements are introduced between all continuum elements modelling the epoxy matrix, and at the interfaces between fibres and epoxy matrix. This modelling approach, which was originally proposed by Xu and Needleman [80] somewhat more than a decade ago, has since then been successfully applied in failure analyses of various materials, such as crazing in polymers [70], and quasi-brittle fracture in cementitious composites [69]. The main advantages of this simulation technique are that (i) the nucleation and growth of cracks is entirely determined by the interaction between existing cracks and the corresponding stress (re-)distribution in the surrounding bulk material, (ii) branching and coalescence of cracks emerge as a natural outcome of the simulation, with no need for additional selection criteria. A disadvantage of the method is that the chosen spatial discretisation of the actual boundary value problem may have an influence on the location and direction of the cracking path. However, as will be shown in this chapter, this effect can be kept small by choosing a sufficiently fine finite element mesh.

This chapter is organised as follows. Section 3.2 discusses the numerical simulation of a sample composed of a single fibre embedded in an epoxy matrix, which is loaded under uniaxial tension. A mesh refinement study is performed in order to examine the objectivity of the numerical results as a function of the finite element discretisation. Subsequently, the effect is studied of the ratio between the fibre-epoxy interfacial strength and the epoxy strength on the failure behaviour of the system, as well as the influence of the ratio between the toughnesses of the fibre-epoxy interface and the epoxy matrix. The section ends with an assessment of the validity of the usage of symmetry boundary conditions for the single-fibre matrix configuration. Section 3.3 treats numerical simulations on uniaxially loaded epoxy systems containing multiple fibres. As for the single-fibre epoxy system, the influence is studied of the ratio between the fibre-epoxy strength and the epoxy strength on the failure response. In addition, the effect of

the fibre volume fraction and the fibre distribution on the failure behaviour of the system is analysed. The chapter ends with a summary of the main conclusions of the study, and a qualitative comparison of the simulation results with experimental observations.

3.2 Simulation of a single-fibre composite

As mentioned in the above introduction, the interface damage model presented in Chapter 2 is used in the numerical simulation of the off-axis strength of unidirectional fibre-epoxy systems. As a start, the failure behaviour of a uniaxially-loaded sample composed of a single S2 glass fibre embedded in a FM94 epoxy matrix is studied. This combination of materials is typical for the fibre-epoxy layers utilised in the fibre-metal laminate GLARE [78]. The modelled sample is assumed to be under plane-strain conditions, which is representative of a fibre with a relatively large (actually infinite) length. As a result of symmetry of the sample geometry, one quarter of the actual configuration may be modelled. The validity of symmetry boundary conditions in terms of the generated sample fracture pattern will be studied in detail in Section 3.2.4. The geometry and boundary conditions of the model are illustrated in Figure 3.1. The symmetry is warranted by placing fixed and roller supports at the left and bottom edges of the sample. The diameter of the S2 glass fibre is $10\mu\text{m}$, which is representative of the glass fibres used in GLARE [78]. The specimen is square-shaped, with a side length of $L = 28\mu\text{m}$, which is in correspondence with a fibre volume fraction $V_f = 0.1$. The tensile loading is imposed by applying a uniform displacement u at the right edge of the specimen. Quasi-static loading conditions are warranted by prescribing a relatively small nominal strain rate of $\dot{u}/L = 4 \times 10^{-3} \text{ s}^{-1}$. The fibre and the epoxy matrix are meshed with 6-node triangular elements equipped with a 7-point Gauss quadrature. Debonding between fibre and matrix is simulated with the interface damage model presented in Section 2.2, using 6-node interface elements equipped with a 3-point Newton-Cotes quadrature. Fracture processes within the epoxy material are also simulated with the interface damage model, placing 6-node interface elements furnished with a 3-point Newton-Cotes quadrature in between the triangular continuum elements constructing the epoxy matrix, see Figure 3.2.

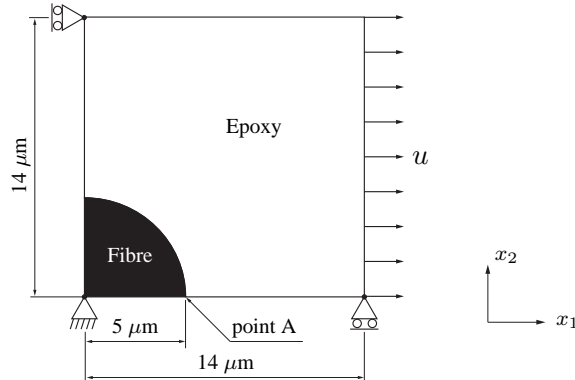


Figure 3.1: Geometry and boundary conditions of a single fibre embedded in an epoxy matrix. Using symmetry boundary conditions only a quarter of the sample can be simulated.

This approach for the simulation of fracture was originally proposed by Xu and Needleman [80], and warrants that the crack initiation and propagation processes in the sample are naturally determined by the geometry and boundary conditions applied, and by the parameter values used in the interface traction-separation law. The influence of the finite element discretisation on the fracture response can be minimised by choosing a sufficiently fine, randomly oriented mesh. Nonetheless, the mesh fineness is bounded by a maximum in order to limit artificial response contributions related to the use of an interface 'dummy' stiffness K in the traction-separation law, see Eq.(2.1). In fact, the application of interface elements with an elastic dummy stiffness causes that the elastic response of the finite element model does not convergence to that of an ideal continuum in the limit of an 'infinitely fine' mesh.

3.2.1 Mesh refinement study

In order to assess the influence of the numerical discretisation on the sample response, three different meshes are considered, see Figure 3.3, named the 'Coarse mesh', 'Intermediate mesh' and 'Fine mesh'. The number of continuum elements and interface elements used in each of these meshes are listed in Table 3.1. The

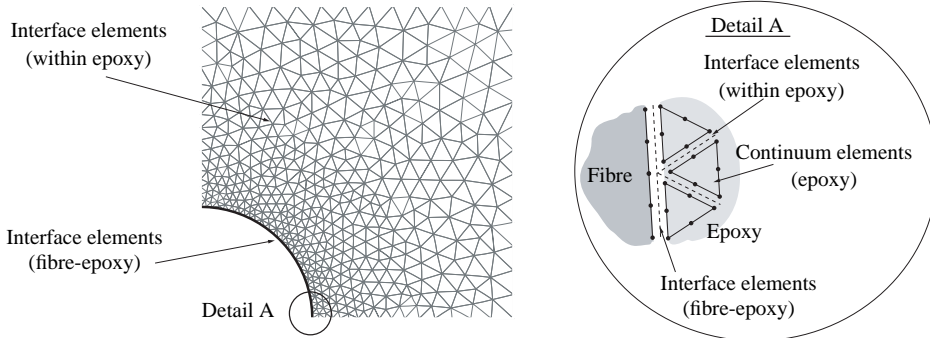
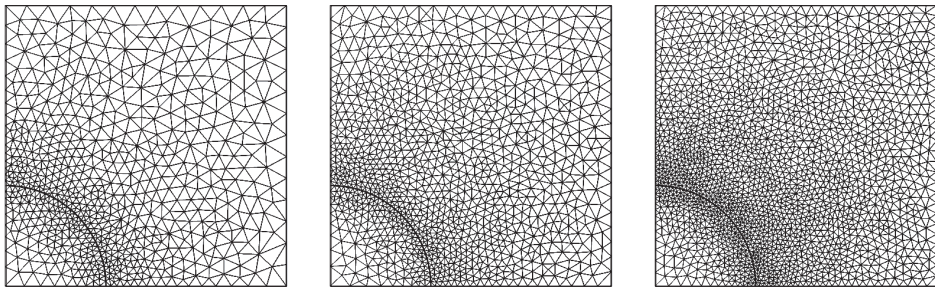


Figure 3.2: Finite element mesh where interface elements are placed at the fibre-epoxy interface and within the epoxy.

material parameters of the S2 glass fibre, the FM94 epoxy and the interfaces within the epoxy and between the fibre and epoxy are summarised in Table 3.2. The elastic material parameters of the fibre and the epoxy (i.e., their Young's modulus and Poisson's ratio) have been taken from [28]. The value of the elastic stiffness K of the interfaces is chosen relatively high in order to warrant interfacial deformations in the elastic regime to remain negligibly small. Values for the ultimate strengths and fracture toughnesses of the epoxy material and the fibre-epoxy interface have not been reported in the literature, and therefore were estimated



(a) Coarse mesh (3003 elements)

(b) Intermediate mesh (5137 elements)

(c) Fine mesh (9569 elements)

Figure 3.3: Three different meshes used in the numerical simulations of the fibre-epoxy sample sketched in Figure 3.1.

Table 3.1: Number of elements for the three different meshes in Figure 3.3.

Mesh	Continuum elements	Fibre-epoxy interface elements	Epoxy interface elements	Total
Coarse	1346	31	1550	2927
Intermediate	2230	34	2775	5039
Fine	4140	44	5247	9431

from the failure response of delamination tests on double spliced GLARE specimens [30]. For simplicity, both for the epoxy and the fibre-epoxy interface the strength and toughness values were taken the same for tension (mode I) and shear (mode II). The subscripts 'coh' and 'adh' used in the denotation of these parameters refer to the *cohesive* strength (toughness) of the epoxy material and the *adhesive* strength (toughness) of the fibre-epoxy interface, respectively. The influence of the strength and toughness parameters on the effective failure response of the sample will be studied in detail by means of parameter variation studies presented in the forthcoming sections. The value of the relaxation parameter η is taken relatively small in order to closely approach the limit case of rate-independent crack growth. Additional simulations not presented here have shown that the introduction of a small rate-dependency is necessary to avoid numerical convergence problems caused during crack coalescence and bifurcation. Figure 3.4 shows the effective sample response for the three different meshes displayed in Figure 3.3, by plotting the prescribed displacement u (normalised by v_{coh}^u) against the traction \tilde{t} averaged across the right sample boundary (normalised by t_{coh}^u). For all three meshes the response is similar, i.e., during fracture the traction drops linearly from a peak value of $\tilde{t}/t_{coh}^u \approx 0.92$ (corresponding to $\tilde{t} \approx 46 \text{ N/mm}^2$) to relatively small value of $\tilde{t}/t_{coh}^u \approx 0.1$ (corresponding to $\tilde{t} \approx 5 \text{ N/mm}^2$), after which the slope of the softening curve changes abruptly and the traction decreases further to zero. Because the sample consists for 90 % of epoxy material, the effective tensile strength of the sample ($= 46 \text{ N/mm}^2$) is close to the tensile strength of the epoxy ($= 50 \text{ N/mm}^2$). The kink in the softening curve is due to the fact that the interface models for fibre-epoxy cracking and for epoxy cracking have different ul-

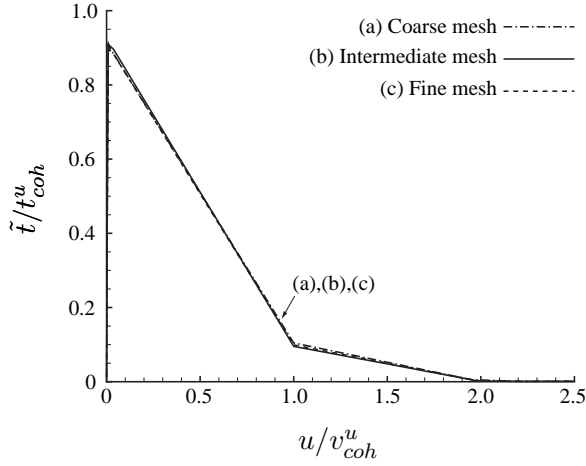


Figure 3.4: Effective sample response for the three different meshes in Figure 3.3. The traction \tilde{t} represents the average value at the right sample boundary at which the displacement u is prescribed, see Figure 3.1.

imate relative displacements v^u . Since the values of the ultimate strength and the fracture toughness were chosen equal for mode I and mode II loading conditions, and the softening branch in the traction-separation curve is linear, the ultimate relative displacement for modes I and II can be simply estimated as $v^u \approx 2G_c/t^u$. With the material data listed in Table 3.2, this leads to $v_{coh}^u \approx 0.02$ mm for the epoxy interface model (which is reached in Figure 3.4 at the kink of the softening branch, when $u = v_{coh}^u$) and $v_{adh}^u \approx 0.04$ mm for the fibre-epoxy interface model (which is reached in Figure 3.4 at the end of the softening branch, when $u = v_{adh}^u = 2v_{coh}^u$). Hence, during the deformation stage between the kink and the end of the softening branch, the crack through the epoxy has completely opened and the remaining load is transferred solely via the fibre-epoxy interface.

In Figure 3.5 the axial normal stress σ_{11} is shown in a deformed configuration (plotted on true scale), for the three different meshes depicted in Figure 3.3. The response states are taken at a prescribed displacement of $u = 0.05 v_{coh}^u$, after the effective peak strength is passed, but before complete failure has occurred, i.e., there is still transfer of loading possible across the separated crack faces, see Figure 3.4. The depicted fracture pattern nucleates at the interface between

Table 3.2: Material properties of the fibre-epoxy sample.

Parameter(s)	Value(s)
Fibre	
Young's modulus	$E = 86.9$ [GPa]
Poisson's ratio	$\nu = 0.23$
Epoxy	
Young's modulus	$E = 3.9$ [GPa]
Poisson's ratio	$\nu = 0.37$
Fibre-epoxy interface	
Elastic stiffness	$K = 1 \times 10^8$ [N/mm ³]
Ultimate normal and shear strengths	$t_1^u = t_2^u = t_{adh}^u = 25$ [MPa]
Mode I and mode II fracture toughnesses	$G_{I,c} = G_{II,c} = G_{c,adh} = 0.5$ [N/mm]
Relaxation parameter	$\eta = 0.002$ [s]
Epoxy interface	
Elastic stiffness	$K = 1 \times 10^8$ [N/mm ³]
Ultimate normal and shear strengths	$t_1^u = t_2^u = t_{coh}^u = 50$ [MPa]
Mode I and mode II fracture toughnesses	$G_{I,c} = G_{II,c} = G_{c,coh} = 0.5$ [N/mm]
Relaxation parameter	$\eta = 0.002$ [s]

the fibre and the epoxy, as represented by point A in Figure 3.1. After some crack growth along the fibre-epoxy interface, the stress locally reaches the tensile strength of the epoxy, where the crack deflects into the epoxy material. The angle θ , at which the crack developing along the fibre perimeter proceeds into the epoxy material (measured with respect to the horizontal axis through the fibre centre), can be estimated using the closed-form expression reported by París *et al.* [52] for an ideally brittle fibre-epoxy system subjected to uniaxial tension:

$$\theta = -2 \operatorname{sgn}(\beta) \arccos \sqrt{\frac{2 + |\beta|}{3 + |\beta|}}, \quad \text{for } \beta \neq 0. \quad (3.1)$$

Here, β is the second Dundur's elastic mismatch parameter, given by [20]

$$\beta = \frac{1}{2} \frac{(1 - 2\nu_2)/\mu_2 - (1 - 2\nu_1)/\mu_1}{(1 - \nu_2)/\mu_2 + (1 - \nu_1)/\mu_1} \quad (3.2)$$

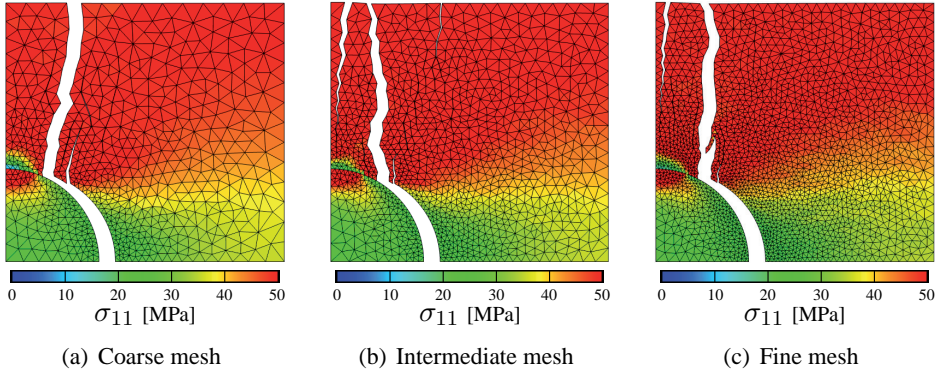


Figure 3.5: Axial normal stress σ_{11} depicted in the deformed configuration (plotted on true scale), for the three different meshes in Figure 3.3. The response states are taken after the effective peak strength is passed, at a prescribed displacement of $u = 0.05 v_{coh}^u$, see Figure 3.4.

with $\mu_i = E_i/2(1 + \nu_i)$ the elastic shear modulus of materials $i = \{1, 2\}$, where E_i and ν_i are the corresponding Young's moduli and Poisson's ratios. Substitution of the material parameters listed in Table 3.2 into Eq.(3.2) leads to $\theta = 68^\circ$. This value for the crack deflection angle is in close correspondence with the numerical values computed for the Coarse mesh ($\theta = 67^\circ$), the Intermediate mesh ($\theta = 61^\circ$) and the Fine mesh ($\theta = 63^\circ$). It can be further observed from this figure that for the Intermediate and Fine meshes a second crack emerges left from the dominant crack in the epoxy. This crack, which is absent in the response for the Coarse mesh, does not have a significant influence on the effective traction-separation response depicted in Figure 3.4. Considering the small differences between the fracture geometries for the Intermediate and Fine meshes, the computationally less expensive Intermediate mesh will be used in the forthcoming computations.

3.2.2 Fibre-epoxy interfacial strength versus epoxy strength

The influence of the ratio between the fibre-epoxy interfacial strength and the epoxy strength on the effective failure response of the single-fibre composite is studied considering three different strength ratios: $t_{adh}^u/t_{coh}^u = 0.5, 1.0$ and 2.0 .

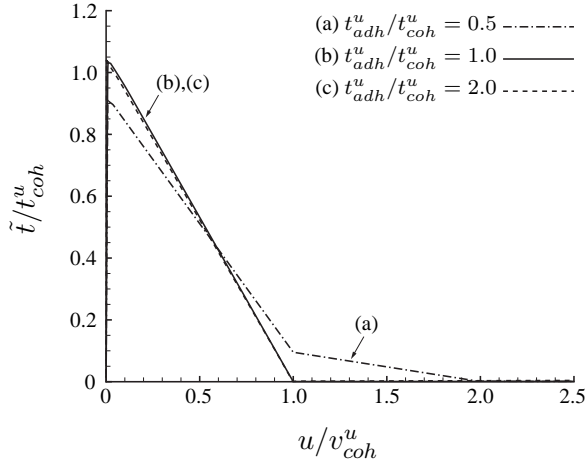
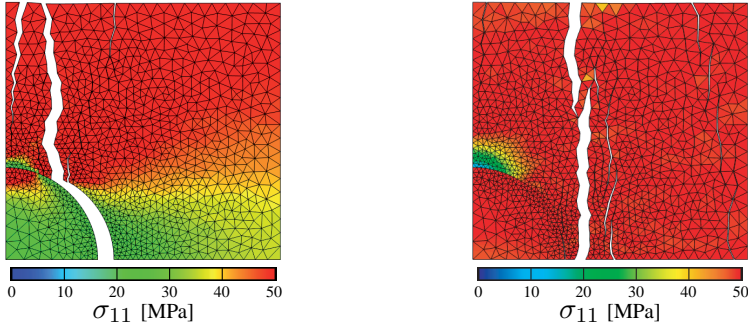


Figure 3.6: Effective sample response for three different strengths ratios $t_{adh}^u/t_{coh}^u = 0.5, 1.0$ and 2.0 . The traction \tilde{t} represents the average value at the right sample boundary at which the displacement u is prescribed, see Figure 3.1.

Here, the value of 0.5 reflects the reference case presented in Table 3.2. In the variation study the ultimate strength of the epoxy is kept constant, $t_{coh}^u = 50$ MPa.

The effective sample response for the three different strength ratios is depicted in Figure 3.6. It can be observed that for the low strength ratio, $t_{adh}^u/t_{coh}^u = 0.5$, the softening curve has a bilinear shape, see also Figure 3.4. In contrast, for the intermediate and high strength ratios, $t_{adh}^u/t_{coh}^u = 1.0$ and 2.0 , the response is characterised by a linear softening branch, which can be explained as follows. When the adhesive strength of the fibre-epoxy interface is larger than the cohesive strength of the epoxy, $t_{adh}^u > t_{coh}^u$, the failure response of the sample is determined by the fracture properties of the epoxy only and, as such, the strength of the fibre-epoxy interface becomes irrelevant. Accordingly, the curved crack along the fibre-epoxy interface, which typically appears when $t_{adh}^u < t_{coh}^u$, see Figure 3.7(a), vanishes, and the cracking pattern fully develops through the epoxy material, see Figure 3.7(b). The (almost) straight crack here indicates that the epoxy material (virtually) fails in mode I. Consequently, the effective failure response in Figure 3.6 closely approximates the mode I traction-separation law of the epoxy material (which is characterised by a linear softening branch, see Figure 2.2), where



(a) Response for the case where $t_{adh}^u < t_{coh}^u$. (b) Response for the case where $t_{adh}^u > t_{coh}^u$.

Figure 3.7: Axial normal stress σ_{11} depicted in the deformed configuration (true scale). The response states are taken after the effective peak strength is passed, at a prescribed displacement of $u = 0.05 v_{coh}^u$, see Figure 3.6.

the maximum effective traction equals $\tilde{t}_{max} = t_{coh}^u$ and the displacement at complete failure equals $u = v_{coh}^u$.

When the adhesive strength of the fibre-epoxy interface is equal to the cohesive strength of the epoxy, $t_{adh}^u = t_{coh}^u$, in principle both fracture patterns depicted in Figure 3.7 can occur; under these circumstances the actual fracture pattern becomes (somewhat arbitrarily) determined by the actual finite element discretisation and (small) numerical round-off errors in the solution procedure. For the present finite element discretisation this has led to a failure response characterised by cracking through the epoxy only, in a similar fashion as depicted in Figure 3.7(b) for the case $t_{adh}^u > t_{coh}^u$.

3.2.3 Fibre-epoxy interfacial toughness versus epoxy toughness

In Figure 3.8 the sample response is depicted for three different ratios of the fibre-epoxy interfacial toughness and the epoxy toughness, namely $G_{c,adh}/G_{c,coh} = 0.5, 1.0$ and 2.0 , where the toughness of the epoxy is kept constant, $G_{c,coh} = 0.5$ N/mm. Since for all cases $t_{adh}^u < t_{coh}^u$, the actual failure mechanism for the three cases closely resembles to that depicted in Figure 3.7(a). The sample deformation capacity for the cases $G_{c,adh}/G_{c,coh} = 1.0$ and 2.0 is set by the

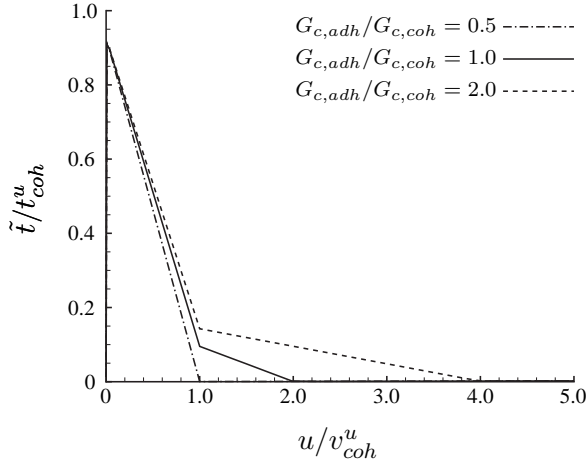


Figure 3.8: Effective sample response for three different ratios between the fibre-epoxy toughness and the epoxy toughness, $G_{c,adh}/G_{c,coh}$.

ultimate relative displacement of the fibre-epoxy interface, and corresponds to $v_{adh}^u = 2v_{coh}^u \approx 0.04$ mm and $v_{adh}^u = 4v_{coh}^u \approx 0.08$ mm, respectively. For the case $G_{c,adh}/G_{c,coh} = 0.5$ the ultimate relative displacements of the epoxy crack and the fibre-epoxy crack are equal, $v_{adh}^u = v_{coh}^u$, which is the reason that the softening branch of the sample response is linear instead of bi-linear. The effective fracture toughness of the sample can be computed from the area under the corresponding traction-separation curve, and equals 0.46 N/mm, 0.55 N/mm and 0.74 N/mm for $G_{c,adh}/G_{c,coh} = 0.5, 1.0$ and 2.0 , respectively. Hence, an increase of the toughness of the fibre-epoxy interface by a factor of $2.0/0.5 = 4.0$ increases the effective toughness of the sample by a factor of only $0.74/0.46 = 1.6$. This is, because most of the fracture occurs in the epoxy material, and therefore the effective sample toughness is not much influenced by a change in the fibre-epoxy interfacial toughness.

3.2.4 Symmetry of fracture pattern

In order to check the validity of symmetry boundary conditions in the computation of the effective sample response, the fracture pattern of the uniaxially loaded sam-

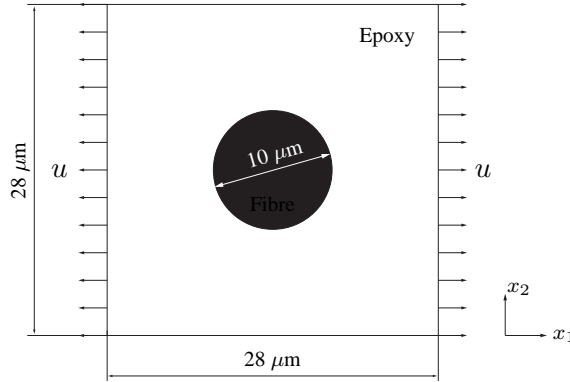


Figure 3.9: Geometry and boundary conditions for the model of the complete sample of a single fibre embedded in an epoxy matrix.

ple modelled with symmetry boundary conditions, see Figure 3.1, is compared to the response of a model of the complete sample, see Figure 3.9. In the model of the complete sample, the uniaxial tensile loading occurs by means of simultaneously prescribing the displacement u at the left and right edges of the sample. The centre point of the sample (which equals the centre point of the embedded fibre) is kept fixed by constraining the horizontal and vertical displacements. The response of the complete sample is computed for two different meshes, see Table 3.3, which have approximately the same mesh density but small differences in the discretised geometry. In terms of the mesh density, the two finite element discretizations are comparable to the Intermediate mesh depicted in Figure 3.3. The material parameters used in the simulations are equal to those of the reference case, as presented in Table 3.2.

Figure 3.10 shows the axial normal stress σ_{11} for three different deformed configurations (plotted on true scale), corresponding to prescribed displacements of $u = 0.05v_{coh}^u$, $0.19v_{coh}^u$ and $0.29v_{coh}^u$, respectively. It can be observed that at $u = 0.05v_{coh}^u$ the responses for the two finite element discretizations are approximately similar, and are comparable to that of the symmetric model plotted in Figure 3.5(b). Nevertheless, at larger axial deformations, $u = 0.19v_{coh}^u$ and $0.29v_{coh}^u$, differences arise in the stress and deformation responses, which are caused by differences in the cracking path (as triggered by the different mesh ge-

Table 3.3: Number of elements for two different meshes, 'Case 1' and 'Case 2', of a complete model of the single-fibre embedded in an epoxy matrix, see Figure 3.9.

Mesh	Continuum elements	Fibre-epoxy interface elements	Epoxy interface elements	Total
Case 1	7498	136	9443	17077
Case 2	7076	136	8787	15999

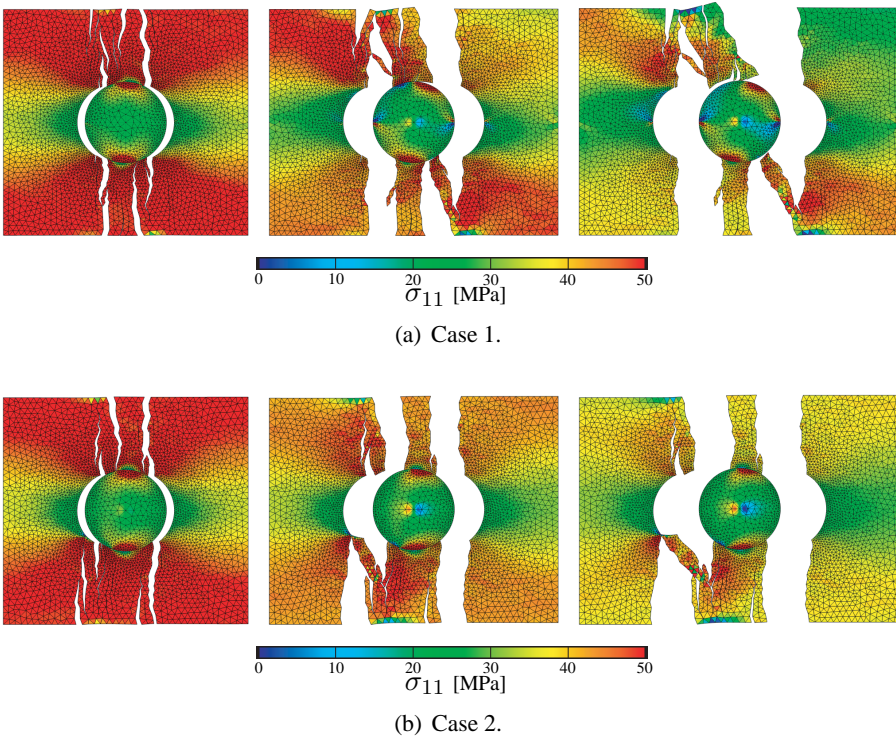


Figure 3.10: Axial normal stress σ_{11} for two different finite element discretizations, 'Case 1' and 'Case 2' (see Table 3.3), depicted in the deformed configuration (true scale). The response states are successively taken at prescribed displacements of $u = 0.05 v_{coh}^u$, $0.19 v_{coh}^u$ and $0.29 v_{coh}^u$.

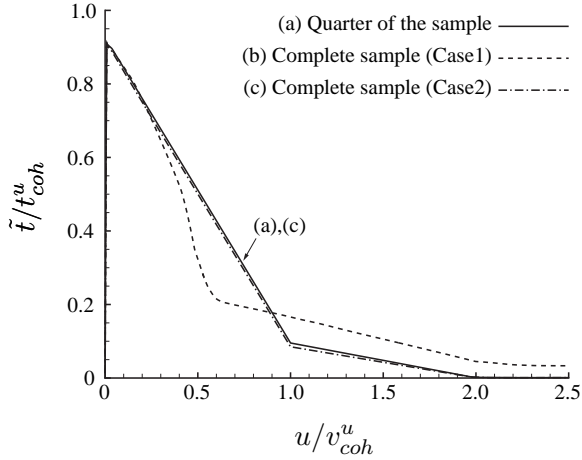


Figure 3.11: Effective sample response for the symmetric model (quarter of specimen, see Figure 3.1) and complete model (see Figure 3.9) of a single fibre embedded in an epoxy matrix. The traction \tilde{t} is the average traction measured at the right specimen edge at which the displacement u is prescribed.

ometries). Correspondingly, as illustrated in Figure 3.11, the effective sample responses for the two finite element discretizations are also different. In comparison to the response of Case 2, which is bi-linear and virtually identical to the response of the symmetric (quarter of the) specimen, the traction variations in the response for Case 1 are stronger, with a rather brittle response (characterised by a strong drop in traction) at the initial part of the softening branch, and a more ductile response at the end of the softening branch. These strong traction variations are caused by part of the epoxy remaining in contact with the fibre during failure, see Figure 3.10. This results in a more non-uniform stress distribution across the specimen width, which in the initial stage of cracking substantially reduces the effective traction of the sample. Conversely, near complete failure the connection between the epoxy and fibre warrants that more deformation needs to be applied in order to reduce the effective traction to zero, causing the sample ductility near complete failure for Case 1 to be larger than for the symmetric specimen (and Case 2).

The good correspondence between the responses of the symmetric specimen

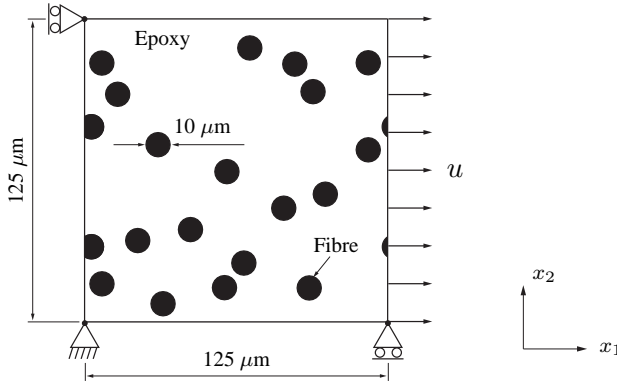


Figure 3.12: Geometry and boundary conditions for an epoxy sample that contains multiple, randomly placed fibres and is subjected to uniaxial tension.

and the full specimen represented by Case 2 validate the use of symmetry boundary conditions in the studies performed in Sections 3.2.1 to 3.2.3. However, as demonstrated by the simulation results for Case 1, small modifications in the finite element discretisation can substantially break the symmetry of the overall fracture response, under which circumstances the effective traction-separation curve of the sample becomes rather different than that of the symmetric specimen.

3.3 Simulation of a multiple-fibre composite

In this section, the off-axis failure response of epoxy samples containing multiple, randomly placed fibres is analysed. The geometry and boundary conditions of one such sample are sketched in Figure 3.12. The sample is square-shaped, and has a side length of $125 \mu\text{m}$. The diameter of the fibres is $10 \mu\text{m}$. The sample width and the fibre diameter are representative of fibre-epoxy layers typically used in the fibre-metal laminate GLARE [78]. As sketched in Figure 3.12, in the tensile direction (i.e., the x_1 -direction) the internal material structure of the sample is modelled as periodic.

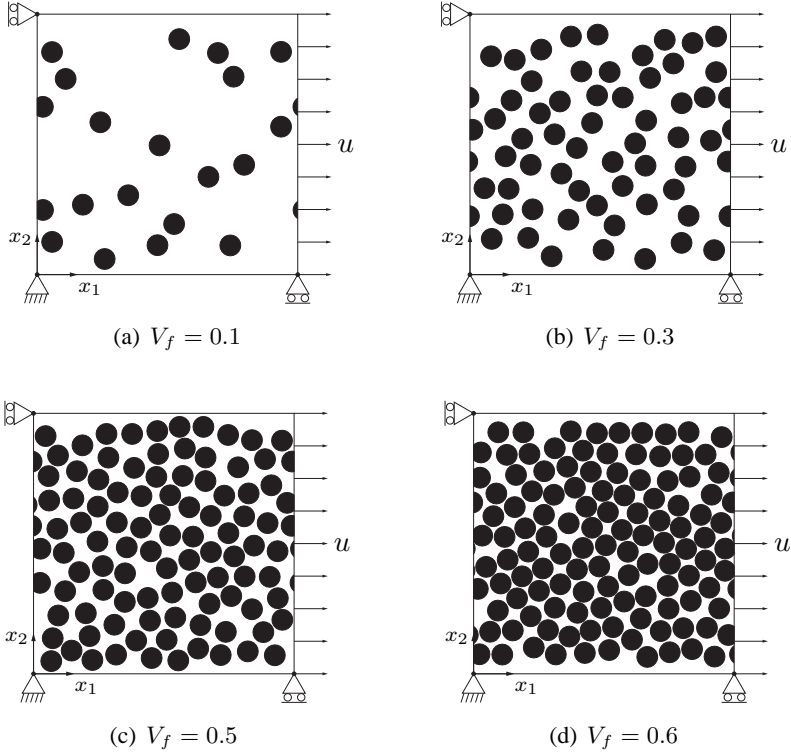


Figure 3.13: Uniaxially-loaded samples with different fibre volume fractions V_f .

3.3.1 Influence of the fibre volume fraction

In order to study the influence of the fibre volume fraction on the failure response of the sample, four different fibre volume fractions are considered, namely $V_f = 0.1, 0.3, 0.5$ and 0.6 . The fibre distributions related to these volume fractions are sketched in Figure 3.13, and the number of elements used in the simulations are summarised in Table 3.4. From the analyses on the single-fibre epoxy samples performed in the previous section, it has been concluded that the actual fracture pattern strongly depends on the relation between the strength of the fibre-epoxy interface and the strength of the epoxy. Accordingly, for the present simulations two strength ratios are considered, i.e., $t_{adh}^u/t_{coh}^u = 0.5$ and $t_{adh}^u/t_{coh}^u = 1.0$.

Table 3.4: Number of elements for the three different meshes in Figure 3.13.

Volume fraction	Continuum elements	Fibre-epoxy interface elements	Epoxy interface elements	Total
$V_f = 0.1$	11192	338	14731	26261
$V_f = 0.3$	9566	1017	9437	20020
$V_f = 0.5$	9844	1678	6716	18238
$V_f = 0.6$	10144	2018	5609	17771

All other material parameters correspond to the values listed in Table 3.2.

For the samples with volume fractions up to and including 0.5, the fibre distributions could be created in a relatively straightforward fashion, by randomly placing fibres within the epoxy matrix. However, for the highest volume fraction of 0.6 this method appeared to be unsuitable, since it could not avoid the overlapping of fibres that results from the limited physical space available in the epoxy matrix. Hence, to construct a microstructure with $V_f = 0.6$, a more advanced method was used, as developed by Stroeven and Stroeven [61]. In this method, fibres are randomly placed in a computational window much larger than the desirable specimen size. The total volume of the fibres (and thus, the total number of fibres) thereby relates to the required volume fraction ($V_f = 0.6$) at the desired specimen size. As a next step, the fibres are given random velocities, and the computational window is shrunk until the desired specimen size is reached. Besides the advantage of obtaining high fibre volume fractions, this method allows for creating fibre distributions with clusters of fibres, which is a realistic micromechanical feature of the fibre-epoxy systems used in GLARE.

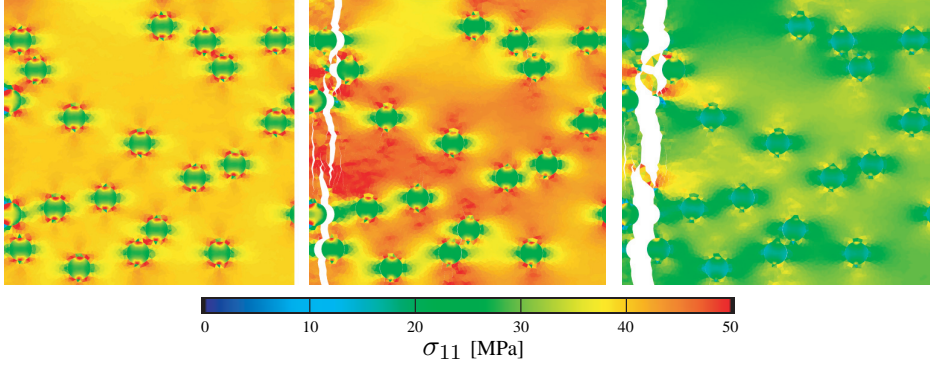
The influence of the fibre volume fraction on the response is illustrated in Figure 3.14, showing the axial stress σ_{11} at three deformed states for the case where the fibre-epoxy interfacial strength is half of the epoxy strength, $t_{adh}^u/t_{coh}^u = 0.5$. Irrespective of the value of the fibre volume fraction, cracking in the sample starts when the (relatively low) interfacial tensile strength of the fibre-epoxy interface of 25 MPa is reached locally. Correspondingly, the tensile stress in the fibres can not exceed 25 MPa, as indicated by the green colour in the stress contour plots in Figure 3.14. When the loading is further increased up to the tensile strength

of the epoxy matrix (= 50 MPa, as represented by the red colour in the stress contour plots), the interfacial cracks start deflecting in the epoxy matrix. Upon further deformation, the coalescence of these cracks leads to the development of a dominant crack across the complete specimen width, precluding overall failure of the sample. It can be observed from Figure 3.14 that the position of the dominant failure crack varies for the different fibre volume fractions, and is determined by the actual fibre distribution in the sample (i.e., the sample heterogeneity).

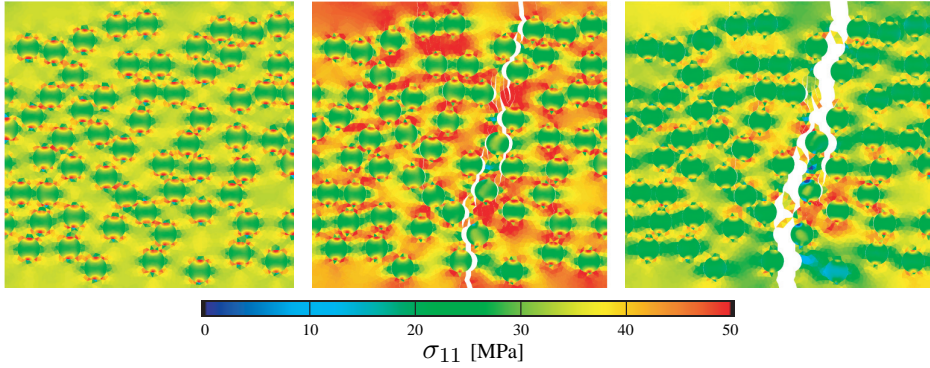
Figure 3.15 illustrates the effective sample response for the various fibre volume fractions. As a result of the relatively low fibre-epoxy interfacial strength, the peak strength of the sample increases with decreasing fibre volume fraction. Essentially, the peak strength for the smallest volume fraction, $V_f = 0.1$, is a factor $0.9/0.67 = 1.34$ larger than that for the largest volume fraction, $V_f = 0.6$. Furthermore, for the specimens with $V_f = 0.1, 0.3$ and 0.5 the effective strength has reached a value close to zero when the prescribed displacement u has become equal to the ultimate separation of the fibre-epoxy interface, $u = v_{adh}^u = 2v_{coh}^u$.

The strength of the specimen with $V_f = 0.6$ at this deformation stage is still somewhat larger, i.e., $\tilde{t} \approx 0.1 t_{coh}^u$. This is caused by the fact that the crack faces of the dominant failure crack in the specimen are locally connected by parts of epoxy, as a result of which transference of loading across the crack faces remains possible at larger deformations, $2v_{coh}^u \leq u \leq 3v_{coh}^u$.

Figure 3.16 shows the axial stress σ_{11} for samples with various fibre volume fractions, for the case where the fibre-epoxy interfacial strength equals the epoxy strength of 50 MPa, i.e., $t_{adh}^u/t_{coh}^u = 1.0$. In contrast to the case $t_{adh}^u/t_{coh}^u = 0.5$ depicted in Figure 3.14, the fibres now do reach the maximum stress of 50 MPa, as indicated by the red colour in the stress contour plots. Since the stiffness of the fibres is (much) larger than that of the epoxy, the fibres reach this maximum stress before the epoxy does, thus acting as stress concentrators (see also, [26, 38, 81]). Again, the dominant failure crack develops after coalescence of smaller fibre-epoxy interfacial cracks and epoxy cracks. The corresponding effective sample response is depicted in Figure 3.17; in contrast to the effective sample response for the case with $t_{adh}^u/t_{coh}^u = 0.5$ shown in Figure 3.15, the curves for the different fibre volume fractions are now similar. Essentially, all curves approach the traction-separation law of the epoxy material (which here equals the traction-separation

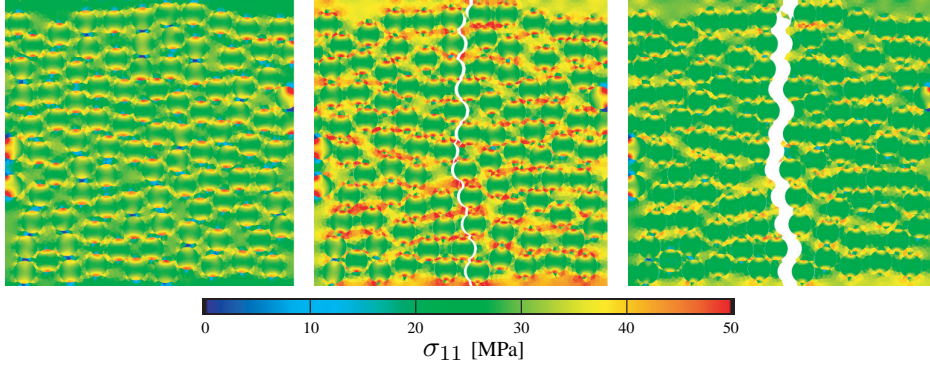


(a) $V_f = 0.1$. Axial normal stress σ_{11} taken at the deformed states $u = 0.06 v_{coh}^u$, $0.23 v_{coh}^u$ and $0.50 v_{coh}^u$.

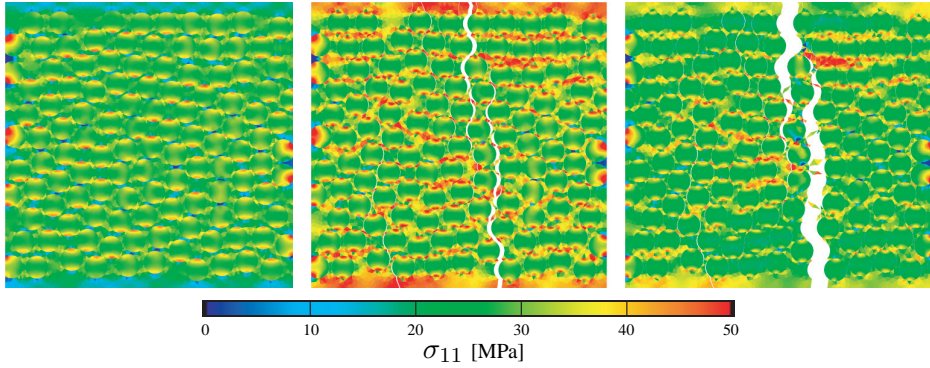


(b) $V_f = 0.3$. Axial normal stress σ_{11} plotted at the deformed states $u = 0.05 v_{coh}^u$, $0.18 v_{coh}^u$ and $0.44 v_{coh}^u$.

Figure 3.14: Axial stress σ_{11} at three deformed states, for different fibre volume fractions, $V_f = 0.1, 0.3, 0.5$ and 0.6 . The ratio between the fibre-epoxy interfacial strength and the epoxy strength is $t_{adh}^u/t_{coh}^u = 0.5$.



(c) $V_f = 0.5$. Axial normal stress σ_{11} plotted at the deformed states $u = 0.03 v_{coh}^u$, $0.13 v_{coh}^u$ and $0.37 v_{coh}^u$.



(d) $V_f = 0.6$. Axial normal stress σ_{11} plotted at the deformed states $u = 0.02 v_{coh}^u$, $0.18 v_{coh}^u$ and $0.43 v_{coh}^u$.

Figure 3.14: Axial stress σ_{11} at three deformed states, for different fibre volume fractions, $V_f = 0.1, 0.3, 0.5$ and 0.6 . The ratio between the fibre-epoxy interfacial strength and the epoxy strength is $t_{adh}^u/t_{coh}^u = 0.5$.

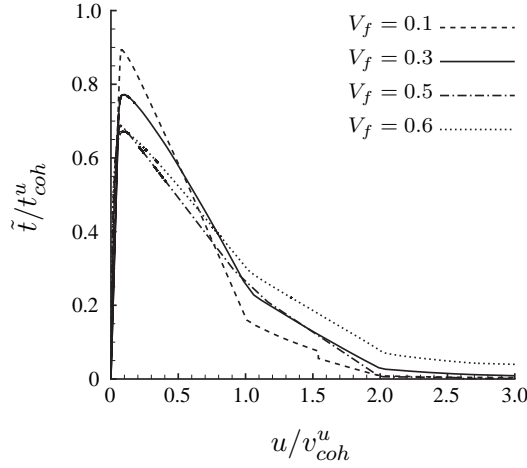
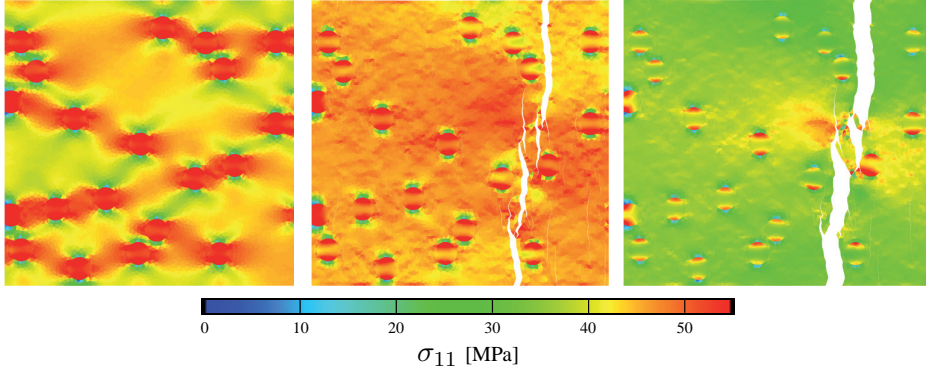


Figure 3.15: Effective sample response for different fibre volume fractions. The traction \tilde{t} represents the average traction measured at the right sample boundary at which the displacement u is prescribed. The ratio between the fibre-epoxy interfacial strength and the epoxy strength is $t_{adh}^u/t_{coh}^u = 0.5$.

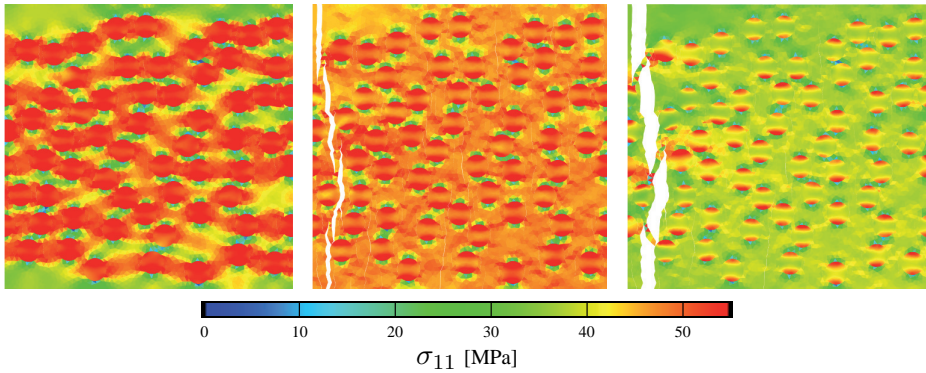
law of the fibre-epoxy interface), as characterised by a maximum strength t_{coh}^u , an ultimate separation v_{coh}^u , and a linear softening branch. This is not surprisingly; because the 'local' traction-separation laws of the epoxy matrix and the fibre-epoxy interface are identical, these are reflected by the 'global' sample response. As explained previously, a small residual strength at relatively large deformations $u > v_{coh}^u$ is caused by small parts of the epoxy connecting the two faces of the dominant failure crack, see also Figures 3.16(a),(b),(c).

3.3.2 Influence of the fibre distribution

To assess the influence of the fibre distribution on the failure response of the multiple-fibre specimen, two different configurations are studied for a fibre volume fraction $V_f = 0.6$, see Figure 3.18. Here, the first fibre distribution, abbreviated as 'Dist. 1', has been taken from the study in the previous section, see also Figure 3.13(d). It can be observed from Figure 3.18 that the second fibre distribution, named 'Dist. 2', is somewhat more uniform than the fibre distribution 'Dist.

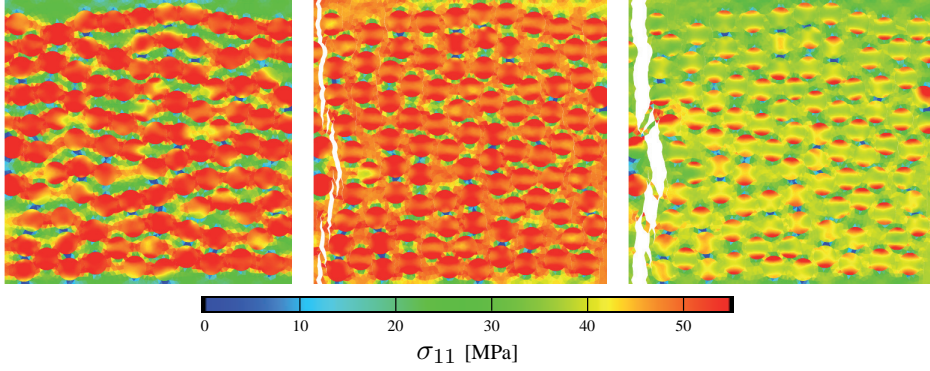


(a) $V_f = 0.1$. Axial normal stress σ_{11} taken at the deformed states $u = 0.06v_{coh}^u$, $0.23v_{coh}^u$ and $0.43v_{coh}^u$.

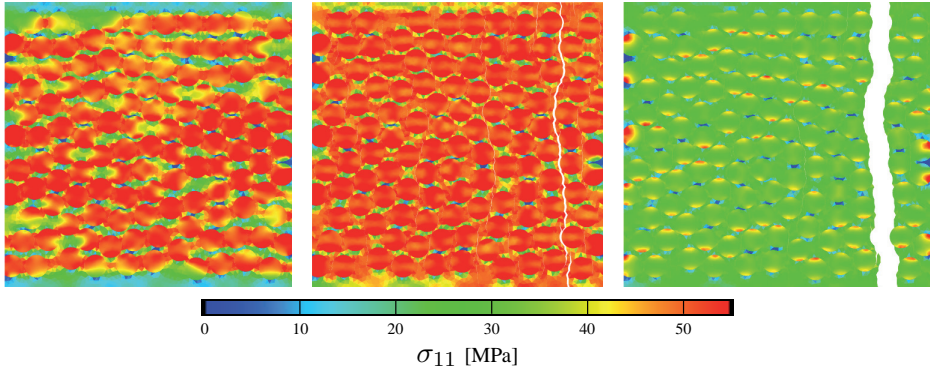


(b) $V_f = 0.3$. Axial normal stress σ_{11} taken at the deformed states $u = 0.05v_{coh}^u$, $0.19v_{coh}^u$ and $0.38v_{coh}^u$.

Figure 3.16: Axial stress σ_{11} at three deformed states, for different fibre volume fractions, $V_f = 0.1, 0.3, 0.5$ and 0.6 . The ratio between the fibre-epoxy interfacial strength and the epoxy strength is $t_{adh}^u/t_{coh}^u = 1.0$.



(c) $V_f = 0.5$. Axial normal stress σ_{11} taken at the deformed states $u = 0.03v_{coh}^u$, $0.16v_{coh}^u$ and $0.37v_{coh}^u$.



(d) $V_f = 0.6$. Axial normal stress σ_{11} taken at the deformed states $u = 0.02v_{coh}^u$, $0.11v_{coh}^u$ and $0.47v_{coh}^u$.

Figure 3.16: Axial stress σ_{11} at three deformed states, for different fibre volume fractions, $V_f = 0.1, 0.3, 0.5$ and 0.6 . The ratio between the fibre-epoxy interfacial strength and the epoxy strength is $t_{adh}^u/t_{coh}^u = 1.0$.

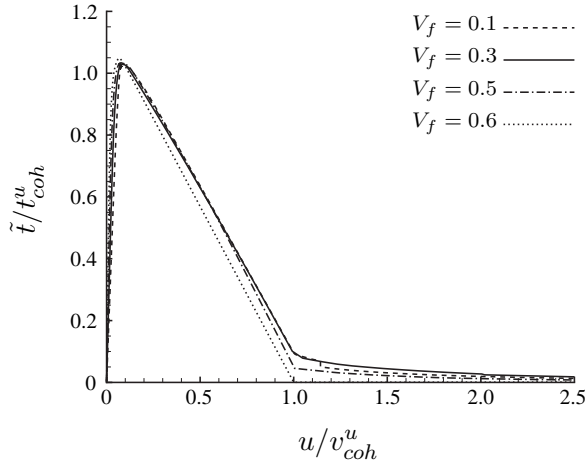


Figure 3.17: Effective sample response for different fibre volume fractions. The traction \tilde{t} represents the average traction measured at the right sample boundary at which the displacement u is prescribed. The ratio between the fibre-epoxy interfacial strength and the epoxy strength is $t_{adh}^u/t_{coh}^u = 1.0$.

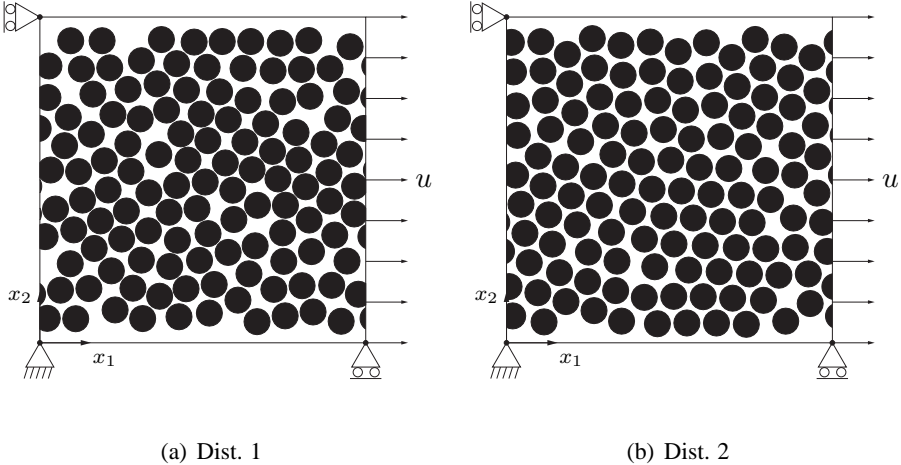


Figure 3.18: Two different fibre distributions for a volume fraction $V_f = 0.6$.

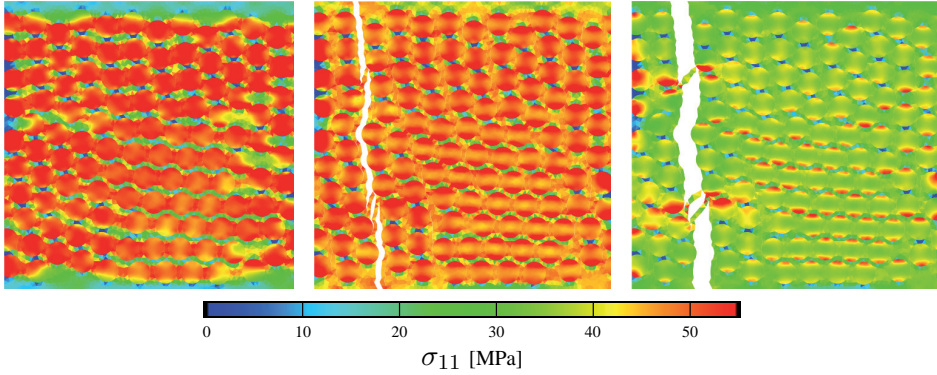


Figure 3.19: Axial stress σ_{11} at the deformed states $u \approx 0.03 v_{coh}^u$, $0.18 v_{coh}^u$, and $0.42 v_{coh}^u$, for fibre distribution 'Dist. 2', see Figure 3.18(b). The ratio between the fibre-epoxy interfacial strength and the epoxy strength is $t_{adh}^u/t_{coh}^u = 1.0$.

1'. In the simulations, the traction ratio has been taken as $t_{adh}^u/t_{coh}^u = 1.0$. As can be observed from Figure 3.19, the axial stress response σ_{11} of 'Dist. 2' is similar to that of 'Dist. 1', plotted in Figure 3.16(d). Nonetheless, due to the different fibre distribution (or, a different sample heterogeneity), the location of the dominant failure crack has changed. However, since the failure is mode I driven, a change in the position of the dominant failure crack does not (substantially) affect the effective sample response, see Figure 3.20.

3.4 Main conclusions and comparison to experiments

Micromechanical simulations on the off-axis failure behaviour of fibre-epoxy systems were presented. The results of the numerical simulations were obtained using the interface damage model presented in Chapter 2. The damage model was used for describing both fracture in the epoxy matrix and debonding of fibres. The fracture patterns obtained for the fibre-epoxy systems were characterised by numerous events of crack coalescence and bifurcation, and were simulated by the interface damage model in a numerically stable and robust fashion.

The numerical results showed that the effective sample response and the corre-

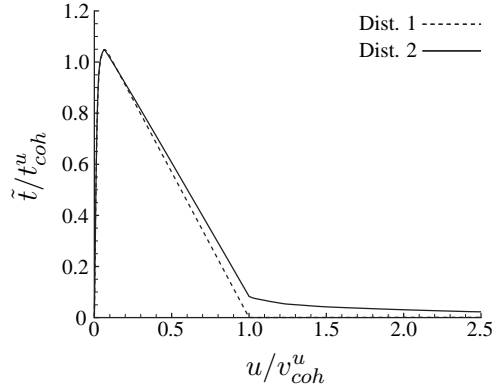


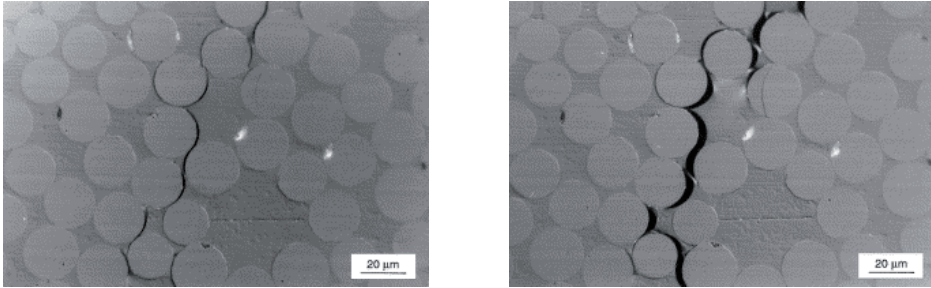
Figure 3.20: Effective sample response for different fibre distributions, 'Dist. 1' and 'Dist. 2', see Figure 3.18. The traction \tilde{t} represents the average traction measured at the right sample boundary at which the displacement u is prescribed. The ratio between the fibre-epoxy interfacial strength and the epoxy strength is $t_{adh}^u/t_{coh}^u = 1.0$.

sponding failure pattern are strongly determined by the ratio between the strengths of the fibre-epoxy interface and the epoxy matrix. If the fibre-epoxy interface is weaker than the epoxy matrix ($t_{adh}^u < t_{coh}^u$), the failure pattern is characterised by a combination of fibre debonding and epoxy cracking. Conversely, if the fibre-epoxy interface is stronger than the epoxy matrix ($t_{adh}^u > t_{coh}^u$), failure occurs solely through cracking in the epoxy matrix. In addition, the toughness ratio $G_{c,adh}/G_{c,coh}$ also has an effect on the effective sample response, but the influence on the sample failure pattern is small.

For epoxy systems containing multiple fibres, the fibre volume fraction only substantially affects the off-axis failure response of the sample if the fibre-epoxy interface is weaker than the epoxy matrix. This is, since for a relatively strong fibre-epoxy interface the only (rather small) contribution of the fibres to the failure response comes from their relatively high stiffness affecting the overall stress distribution. Furthermore, for fibre-epoxy systems with a large fibre volume fraction ($V_f = 0.6$), the failure response is only minorly influenced by the fibre distribution.

The failure patterns obtained from the numerical simulations are in good qual-

itative agreement with experimental results from static tensile tests, as obtained by Gamstedt *et al.* [23] on glass fibre-epoxy systems, see Figure 3.21, and by Hobbiebrunken *et al.* [37] on carbon fibre-epoxy composites, see Figure 3.22. In both experimental works the overall off-axis failure response of the fibre-epoxy specimens was characterised by coalescence of fibre debonding cracks, thus indicating that the fibre-epoxy interfacial strength in the test samples is lower than the epoxy strength. For a quantitative comparison between the present model and the results from experimental studies, it is necessary to accurately calibrate the cohesive laws of the fibre-epoxy interface and the epoxy matrix, which can be done through the performance of single-fibre pull-out tests and mixed-mode fracture tests on relatively small epoxy specimens. The present study aims to stimulate experimental investigators to put new efforts into this research direction.



(a) Fibre-matrix debonding.

(b) Coalescence of cracks into a dominant failure crack.

Figure 3.21: Experimentally observed failure pattern in carbon-fibre epoxy specimens loaded under uniaxial tension, taken from Gamstedt *et al.* [23].

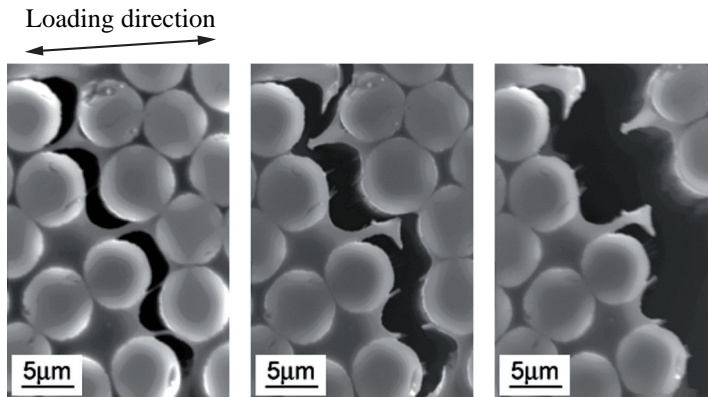


Figure 3.22: Experimentally observed failure pattern (at different consecutive deformation stages) of carbon fibre-epoxy specimens loaded under uniaxial tension, taken from Hobbiebrunken *et al.* [37].

Computational homogenization for simulating discrete fracture in fibre-epoxy systems

4.1 Introduction

Finite element simulations serve as an important tool for studying the complex failure behaviour of fibre-metal laminates (FMLs) and optimizing their performance in (macroscopic) engineering applications. However, the execution of a direct numerical simulation on the mechanical response of an engineering structure, where all the details of the underlying microstructure are incorporated, requires a very fine finite element mesh, leading to an impractical amount of computational time. A more efficient approach for this purpose is to use material models that represent the mechanical response of the underlying microstructure in an effective fashion. Such models can be obtained by applying homogenization

techniques, where various approaches have been proposed over the years, e.g., [7, 10, 19, 22, 31, 34, 39].

Analytical homogenization techniques often fail to describe the effective material response accurately when the underlying microstructure is complex and is characterised by a non-linear constitutive behaviour. Under these circumstances the use of a computational homogenization method is recommendable. Computational homogenization is based on numerically averaging the generated microstructural stress and deformation over a representative volume element (RVE), thereby implicitly (i.e., not in closed-form) establishing an effective, mesoscopic constitutive relation between the average stress (or traction, in the case of an interface model) and deformation [24, 25, 27, 45, 48, 50, 51, 67]. The method relies on a local periodicity of the microstructure in the direct neighborhood of the RVE, but does not impose periodicity over the complete macroscopic structure under consideration (i.e., global periodicity is not required). Essentially, the macroscopic structure contains mesoscopic material points for which the specific microscopic RVEs are assumed to be periodic only in a small vicinity of the material points.

The overall failure behaviour of FMLs strongly depends on small-scale fracture events occurring within individual fibre-epoxy (prepreg) layers, such as fibre decohesion and matrix cracking, see Chapter 3. Accordingly, the present chapter focuses upon the derivation of the effective mesoscale failure response of a fibre-epoxy sample from its complex microscale fracture behaviour. The mesoscale failure response is represented by a traction-separation curve constructed from numerically homogenizing the fracture response of a periodic fibre-epoxy microstructure loaded under uniaxial tension. The traction-separation curve can be applied in material points of interface elements that are used for simulating mesoscopic fracture in macroscopic laminate failure problems. This modelling approach is an appealing and acceptable alternative to the (costly) direct simulation of microscale fracture in macroscopic problems if the fluctuations of the microscale crack trajectories in the thickness direction of the laminate are much smaller than the laminate thickness itself (i.e., a separation of length scales can be warranted). The analysis of specific macroscopic problems, however, falls beyond the scope of the study in the present chapter; the attention is directed here to the numerical homogenization of the response of a microstructural RVE to a

mesoscopic traction-separation curve, thereby considering the influence of the fibre volume fraction and local imperfections. Although the numerical examples treated focus upon uniaxial tension, the homogenization framework presented is applicable to arbitrary loading conditions.

The organisation of this chapter is as follows. In Section 4.2 the governing equations of the fibre-epoxy material are formulated at the meso- and microscales. The numerical homogenization framework that connects the fracture behaviour of the microstructural fibre-epoxy sample to a mesoscopic traction-separation response is presented in Section 4.3. In Section 4.4 the applicability of the numerical homogenization framework is demonstrated by studying fibre-epoxy samples loaded under uniaxial tension. The convergence of the RVE size is examined, as well as the effect of the fibre volume fraction and the presence of imperfections on the traction-separation response. Finally, in Section 4.5 the main conclusions of the study are summarised.

4.2 Micro- and mesoscale modelling

Consider a mesoscopic domain $\Omega^M \subset \mathbb{R}^2$ with an external boundary Γ^M , see Figure 4.1. The external boundary is subjected to displacements \mathbf{u}^M and tractions \mathbf{t}^M at Γ_u^M and Γ_t^M , respectively. The mesoscopic domain is crossed by an adhesive layer Γ_{coh}^M . The response in a material point of the adhesive layer is connected to the lower-scale response of a heterogeneous, microscopic domain $\Omega^m \subset \mathbb{R}^2$. The microscopic domain is represented by a fibre-epoxy sample of width b . Fracture in the microscopic domain occurs along the cracking path Γ_{coh}^m . The boundary conditions at the outer edges Γ^m of the microscopic domain are assumed to be periodic.

4.2.1 Governing equations at the mesoscale

The equilibrium condition for an arbitrary material point in the mesoscopic domain Ω^M depicted in Figure 4.1 is

$$\sigma_{ij,j}^M = 0 \quad \text{in } \Omega^M, \quad (4.1)$$

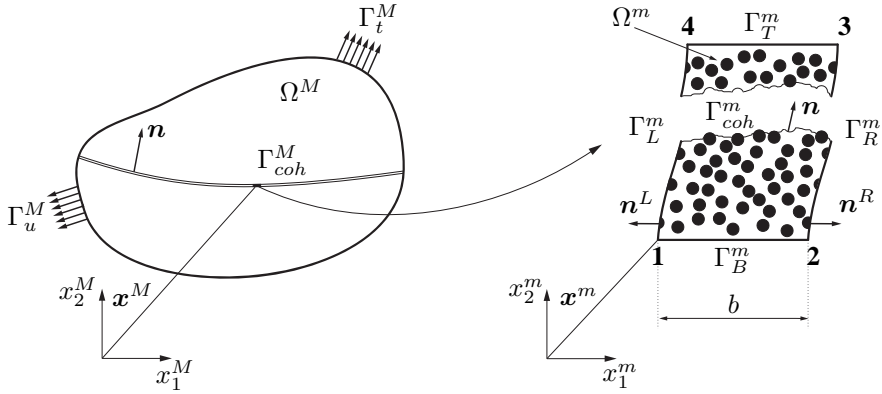


Figure 4.1: Mesoscopic domain Ω^M and microscopic domain Ω^m . The mesoscopic domain is crossed by an adhesive layer Γ_{coh}^M . The failure behaviour in a material point of the adhesive layer is connected to the failure response of the microscopic domain (i.e., a fibre-epoxy sample), as characterised by cracking across the domain width b along the internal boundary Γ_{coh}^m . The boundary conditions at the outer edges Γ^m of the microscopic domain are periodic.

where σ_{ij}^M represents the Cauchy stress, with the superscript M denoting the mesoscopic character of the variable. The tensor indices can have the values $i, j \in \{1, 2\}$, in correspondence with the two-dimensional, orthogonal coordinate system shown in Figure 4.1. Note that, for reasons of convenience, the body forces have been omitted in Eq.(4.1). In addition, the boundary conditions for the mesoscopic domain are given by

$$\sigma_{ij}^M n_j = t_i^M \quad \text{on } \Gamma_t^M, \quad (4.2)$$

$$u_i^M = \hat{u}_i^M \quad \text{on } \Gamma_u^M, \quad (4.3)$$

where t_i^M and \hat{u}_i^M respectively are the tractions and displacements, as prescribed on the corresponding external boundaries Γ_t^M and Γ_u^M with outward normal n_i . Note that the total external boundary is given by $\Gamma^M = \Gamma_t^M \cup \Gamma_u^M$. The cohesive surface Γ_{coh}^M can be considered as an internal boundary, for which the tractions t_i^M are related to the Cauchy stress σ_{ij}^M through the equilibrium condition

$$\sigma_{ij}^M n_j = t_i^M \quad \text{on } \Gamma_{coh}^M. \quad (4.4)$$

Applying the standard variational method, the principle of virtual work at the mesoscale, under the neglect of body forces, leads to the following expression

$$\int_{\Omega^M} \sigma_{ij}^M \delta \varepsilon_{ij}^M \, d\Omega^M + \underbrace{\int_{\Gamma_{coh}^M} t_i^M \delta \llbracket u_i^M \rrbracket \, d\Gamma_{coh}^M}_{\delta W_{coh}^M} = \int_{\Gamma_t^M} t_i^M \delta u_i^M \, d\Gamma_t^M, \quad (4.5)$$

which holds for any admissible variational mesoscale displacement δu_i^M . Here, ε_{ij}^M represents the mesoscopic strain, and the symbol $\llbracket \bullet \rrbracket = (\bullet^+ - \bullet^-)$ denotes the jump of a quantity (i.e., the displacement) across the cohesive surface, with \pm designating the upper and lower faces of the cohesive surface¹. As can be observed from the above expression, the quantity δW_{coh}^M represents the virtual work of the cohesive surface.

4.2.2 Governing equations at the microscale

Similar to the mesoscale equilibrium condition (4.1), the equilibrium requirement for a material point within the microscopic representative volume element (RVE) Ω^m shown in Figure 4.1 can be expressed as

$$\sigma_{ij,j}^m = 0 \quad \text{in } \Omega^m, \quad (4.6)$$

where the boundary conditions are

$$\sigma_{ij}^m n_j = t_i \quad \text{on } \Gamma_t^m, \quad (4.7)$$

$$u_i = \hat{u}_i \quad \text{on } \Gamma_u^m. \quad (4.8)$$

Here, t_i and \hat{u}_i are the tractions and displacements at the corresponding external boundaries Γ_t^m and Γ_u^m of the microscopic RVE, with the superscript m indicating the microscopic character of these parameters. The total external boundary of the RVE is given by $\Gamma^m = \Gamma_t^m \cup \Gamma_u^m$. In order to keep the notation in forthcoming sections concise, the index m will *not* be used for all microscale variables

¹In Chapter 2 of this thesis the relative displacement across a mesoscopic cohesive surface is designated as v_i ; however, in this chapter this displacement jump is denoted as $\llbracket u_i^M \rrbracket$ for convenience of notation.

introduced in this section, i.e., note that it has been omitted for the tractions t_i and the displacements u_i in Eqs.(4.7) and (4.8). As a next step, equilibrium at the microscale cohesive surface Γ_{coh}^m is prescribed by

$$\sigma_{ij}^m n_j = t_i \quad \text{on } \Gamma_{coh}^m. \quad (4.9)$$

Similar to Eq.(4.5), the principle of virtual work at the microscale leads to

$$\int_{\Omega^m} \sigma_{ij}^m \delta \varepsilon_{ij}^m \, d\Omega^m + \underbrace{\int_{\Gamma_{coh}^m} t_i \delta \llbracket u_i \rrbracket \, d\Gamma_{coh}^m}_{\delta W_{coh}^m} = \int_{\Gamma_t^m} t_i \delta u_i \, d\Gamma_t^m, \quad (4.10)$$

which must be satisfied for any admissible variational microscale displacement δu_i . In the above expression, ε_{ij}^m is the microscale strain tensor and δW_{coh}^m is the virtual work of the microscale cohesive interface.

4.3 Connection between the microscale and mesoscale

In order to establish a connection between the responses of the microscale and mesoscale domains shown in Figure 4.1, the microscale displacement field u_i is expressed in terms of the mesoscale displacement field u_i^M and a fluctuation displacement field \tilde{u}_i as

$$u_i(x_j^M, x_k^m) = u_i^M(x_j^M) + \tilde{u}_i(x_k^m), \quad (4.11)$$

where, as illustrated in Figure 4.1, x_j^M and x_k^m denote the locations of the meso-scale and microscale material points at which u_i^M and \tilde{u}_i are evaluated, respectively. Essentially, the fluctuation displacement field \tilde{u}_i accounts for the displacement variations generated by the microstructural inhomogeneities, as measured with respect to the (average) mesoscopic displacement of the microscale RVE.

4.3.1 Formulation of boundary conditions on the RVE

In correspondence with the decomposition given by Eq.(4.11), periodic boundary conditions for the microscale RVE can be formulated as

$$\begin{aligned}
 \tilde{u}_i^T(s_1) &= \tilde{u}_i^B(s_1), \\
 t_i^T(s_1) &= -t_i^B(s_1), \\
 \tilde{u}_i^L(s_2) &= \tilde{u}_i^R(s_2), \\
 t_i^L(s_2) &= -t_i^R(s_2),
 \end{aligned} \tag{4.12}$$

where s_1 is a local coordinate along the Γ_T^m and Γ_B^m boundaries of the RVE, and s_2 is a local coordinate along the Γ_L^m and Γ_R^m boundaries of the RVE. The first two boundary conditions for the Top (T) and bottom (B) edges of the RVE reflect the periodicity in the x_2^m -direction, where the second boundary condition ensures that the total work generated by the periodic boundary conditions is zero. Similarly, the last two boundary conditions for the left (L) and right (R) edges of the RVE warrant periodicity in the x_1^m -direction.

The displacements of the four corner nodes of the microscale RVE in Figure 4.1 correspond to the (uniform) mesoscopic deformation of a material point in the cohesive interface Γ_{coh}^M . Hence, the displacement jump across the mesoscale cohesive interface may be expressed in terms of the displacement difference of two opposite corner nodes at the top and bottom surfaces of the RVE as

$$\llbracket u_i^M \rrbracket = u_i^{M,T} - u_i^{M,B} = u_i^4 - u_i^1 = u_i^3 - u_i^2. \tag{4.13}$$

In accordance with this condition, the microscale displacement fluctuations are equal to zero at the four RVE corner nodes, i.e.,

$$\tilde{u}_i^n = 0 \quad \text{with} \quad n \in \{1, 2, 3, 4\}. \tag{4.14}$$

When combining Eqs.(4.14) and (4.11) with Eq.(4.12), the periodic displacement boundary conditions, Eq.(4.12), may be reformulated as

$$\begin{aligned}
 u_i^T(s_1) &= u_i^B(s_1) + u_i^4 - u_i^1 & (\text{or, } u_i^T(s_1) &= u_i^B(s_1) + u_i^3 - u_i^2), \\
 u_i^R(s_2) &= u_i^L(s_2) + u_i^2 - u_i^1 & (\text{or, } u_i^R(s_2) &= u_i^L(s_2) + u_i^3 - u_i^4).
 \end{aligned}$$

$$(4.15)$$

The above form of the periodic displacement boundary conditions is suitable for implementation within a finite element code.

4.3.2 Derivation of the mesoscopic interfacial traction

For establishing an expression for the mesoscopic traction, t_i^M , in a material point at the mesoscale cohesive interface Γ_{coh}^M , the averaging principle proposed by Hill [35] is applied. This principle states that the spatial average of the virtual work at the microscale, $\overline{\delta W^m}$, needs to be equal to the virtual work in a local material point of the mesoscale cohesive interface, δw_{coh}^M , i.e.,

$$\overline{\delta W^m} = \delta w_{coh}^M. \quad (4.16)$$

Since the local virtual work and total virtual work for the mesoscale cohesive interface are related as

$$\delta W_{coh}^M = \int_{\Gamma_{coh}^M} \delta w_{coh}^M \, d\Gamma_{coh}^M, \quad (4.17)$$

where the total virtual work is given by the second term in Eq.(4.5), the local virtual work of the mesoscale cohesive interface is expressed by

$$\delta w_{coh}^M = t_i^M \delta \llbracket u_i^M \rrbracket. \quad (4.18)$$

In addition, the average virtual work at the microscale is determined by contributions of the cohesive interface Γ_{coh}^m and the adjacent continuum Ω^m as

$$\overline{\delta W^m} = \frac{1}{b} \delta W^m = \frac{1}{b} \left\{ \int_{\Omega^m} \sigma_{ij}^m \delta \varepsilon_{ij}^m \, d\Omega^m + \int_{\Gamma_{coh}^m} t_i \delta \llbracket u_i \rrbracket \, d\Gamma_{coh}^m \right\}. \quad (4.19)$$

Note from the above expression that the averaging procedure is performed by dividing the total virtual work of the microscale RVE by its width b . The height of the RVE does not need to be taken into account here, since the actual mesoscale

geometrical object is a cohesive surface Γ_{coh}^M with zero thickness. Invoking Eq. (4.10), the term in between the curly braces in Eq.(4.19) may be rewritten as

$$\overline{\delta W^m} = \frac{1}{b} \int_{\Gamma_t^m} t_i \delta u_i \, d\Gamma_t^m. \quad (4.20)$$

Substituting the displacement decomposition, Eq.(4.11), into Eq.(4.20) then leads to

$$\overline{\delta W^m} = \frac{1}{b} \left(\int_{\Gamma_t^m} t_i \delta u_i^M \, d\Gamma_t^m + \int_{\Gamma_t^m} t_i \delta \tilde{u}_i \, d\Gamma_t^m \right). \quad (4.21)$$

The second integral term in the right-hand side of Eq.(4.21) may be developed as

$$\begin{aligned} \int_{\Gamma_t^m} t_i \delta \tilde{u}_i \, d\Gamma_t^m &= \int_{\Gamma_L^m} t_i^L \delta \tilde{u}_i^L \, d\Gamma_L^m + \int_{\Gamma_R^m} t_i^R \delta \tilde{u}_i^R \, d\Gamma_R^m + \\ &\quad + \int_{\Gamma_T^m} t_i^T \delta \tilde{u}_i^T \, d\Gamma_T^m + \int_{\Gamma_B^m} t_i^B \delta \tilde{u}_i^B \, d\Gamma_B^m \\ &= \int_{\Gamma_t^m} t_i^T (\delta \tilde{u}_i^T - \delta \tilde{u}_i^B) \, ds_1 + \int_{\Gamma_t^m} t_i^R (\delta \tilde{u}_i^R - \delta \tilde{u}_i^L) \, ds_2 \\ &= 0, \end{aligned} \quad (4.22)$$

in which the boundary conditions, Eq.(4.12) are substituted to arrive at the final result that the microscopic fluctuation field does not contribute to the average microscale virtual work. As mentioned previously, s_1 here is a local coordinate along the Γ_T^m and Γ_B^m boundaries of the RVE, and s_2 is a local coordinate along the Γ_L^m and Γ_R^m boundaries of the RVE. As a next step, the first integral term in

the right-hand side of Eq.(4.21) is developed as

$$\begin{aligned}
 \int_{\Gamma_t^m} t_i \delta u_i^M d\Gamma_t^m &= \int_{\Gamma_L^m} t_i^L \delta u_i^{M,L} d\Gamma_L^m + \int_{\Gamma_R^m} t_i^R \delta u_i^{M,R} d\Gamma_R^m + \\
 &\quad + \int_{\Gamma_T^m} t_i^T \delta u_i^{M,T} d\Gamma_T^m + \int_{\Gamma_B^m} t_i^B \delta u_i^{M,B} d\Gamma_B^m \\
 &= \int_{\Gamma_t^m} t_i^T \left(\delta u_i^{M,T} - \delta u_i^{M,B} \right) ds_1 + \\
 &\quad + \int_{\Gamma_t^m} t_i^R \left(\delta u_i^{M,R} - \delta u_i^{M,L} \right) ds_2 \\
 &= (\delta u_i^4 - \delta u_i^1) \int_{\Gamma_t^m} t_i^T ds_1 + (\delta u_i^2 - \delta u_i^1) \int_{\Gamma_t^m} t_i^R ds_2,
 \end{aligned} \tag{4.23}$$

where the periodicity conditions given by Eqs.(4.12) and (4.15) are inserted to arrive at the final expression. In order to develop this expression further, the specific boundary conditions of the microscale RVE need to be invoked. Within a finite element setting, the boundary conditions, Eq.(4.13), can be applied in two different ways, which are depicted in Figure 4.2 as 'Case 1' and 'Case 2'. The essential difference between these two cases relates to the horizontal displacement of the right corner node at the bottom RVE edge (i.e., node 2), which is unconstrained for Case 1 and fully constrained for Case 2. Correspondingly, the boundary conditions for Case 1 introduce the following constraints on the RVE

$$\delta u_1^1 = \delta u_1^2 = 0, \quad \delta u_2^2 = 0, \quad \int_{\Gamma_R^m} t_1^R d\Gamma_R^m = 0, \tag{4.24}$$

where the last constraint essentially corresponds to a zero average normal stress in the x_1^m -direction of the RVE (which is in agreement with an unconstrained displacement of node 2 in the x_1^m -direction). In contrast, the boundary conditions for Case 2 imply

$$\delta u_1^1 = \delta u_1^2 = 0, \quad \delta u_2^1 = \delta u_2^2 = 0, \tag{4.25}$$

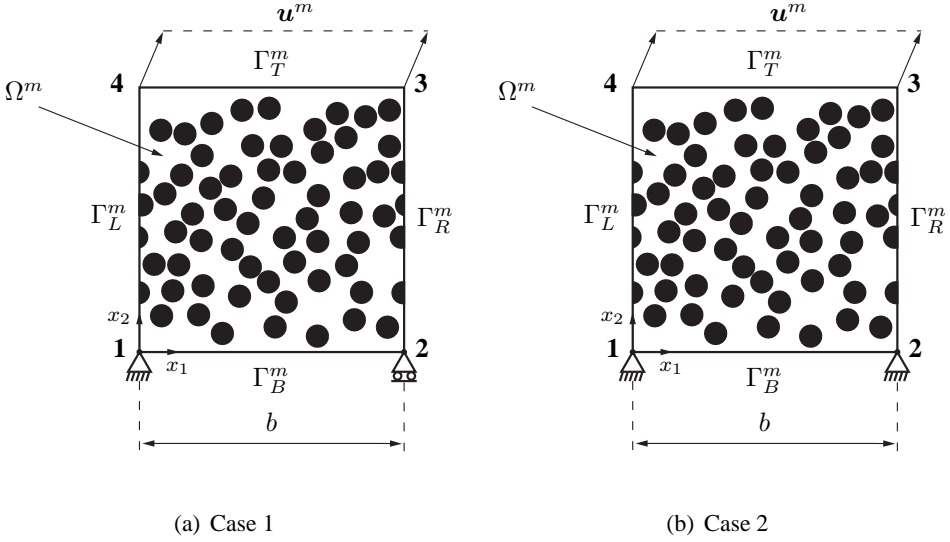


Figure 4.2: Two different boundary conditions for the microscale RVE.

where the third constraint in the above expression corresponds to a zero displacement of node 2 in the x_1^m -direction of the RVE. Despite the different boundary conditions for Cases 1 and 2, substitution of either Eq.(4.24) or Eq.(4.25) into Eq.(4.23) leads to an identical result, namely that

$$\int_{\Gamma_t^m} t_i \delta u_i^M d\Gamma_t^m = \delta u_i^A \int_{\Gamma_T^m} t_i^T d\Gamma_T^m. \quad (4.26)$$

Subsequently, inserting Eq.(4.26) together with Eq.(4.22) into Eq.(4.21) gives

$$\overline{\delta W^m} = \frac{1}{b} \int_{\Gamma_T^m} t_i^T d\Gamma_T^m \delta u_i^A. \quad (4.27)$$

In accordance with Eq.(4.16), this expression needs to be equated with the virtual work in a local material point of the mesoscopic cohesive interface, δw_{coh}^M , given by Eq.(4.18), which leads to

$$t_i^M \delta \llbracket u_i^M \rrbracket = \frac{1}{b} \int_{\Gamma_T^m} t_i^T d\Gamma_T^m \delta u_i^A. \quad (4.28)$$

Since $\llbracket u_i^M \rrbracket = u_i^A$ for both Case 1 and Case 2, see Figure 4.2, the above expression generally results in

$$t_i^M = \frac{1}{b} \int_{\Gamma_T^m} t_i^T d\Gamma_T^m. \quad (4.29)$$

Obviously, within a finite element discretisation the integral term in the right-hand side of Eq.(4.29) is approximated by the summation of the nodal forces at the top edge of the RVE. Although Eq.(4.29) is applicable to both types of RVE boundary conditions depicted in Figure 4.2, the results computed with this expression will be nevertheless different, as a result of the different responses of the two microscale RVE's. Here, it is difficult to say which of the two RVE's generally provides a more accurate representation for the behaviour at the mesoscale, since this typically depends on the characteristics of the macroscopic boundary value problem under consideration. Hence, for the numerical simulations presented in the forthcoming sections, the boundary conditions of the RVE are chosen somewhat arbitrarily in accordance with Case 1.

4.4 Numerical simulations of a fibre-epoxy specimen subjected to uniaxial tension

In the present section a mesoscale traction-separation curve is derived from the failure response of a microscale fibre-epoxy sample using the homogenization framework presented in Section 4.3.2. Although the homogenization framework can be applied to samples subjected to arbitrary combinations of tensile and shear loading, for simplicity the examples studied focus upon uniaxial tension. The interface damage model presented in Section 2.2 is used to study matrix cracking and debonding between fibres and matrix.

4.4.1 Geometry and boundary conditions of the fibre-epoxy sample

In order to check whether the sample size converges to a representative volume element, in the numerical analyses two different specimen widths are considered. For each of these samples two different fibre volume fractions are studied, i.e., $V_f = 0.3$ and 0.5 , see Figures 4.3 and 4.4. The samples are subjected to uniaxial tension by prescribing the vertical displacement, \hat{u} , at the top edge of the sample. Periodic boundary conditions are prescribed at the left and right edges of the sample, as explained in Section 4.3.1. The displacement at the bottom edge of the sample is constrained in the vertical direction, and the displacement of the node at the bottom-left corner of the specimen is also constrained in the horizontal direction, see Figures 4.3 and 4.4. These boundary conditions are in correspondence with Case 1 depicted in Figure 4.2(a).

The first sample studied is square-shaped, with a width (and height) equal to 0.125 mm. The second sample is rectangular-shaped, where, in comparison with the square-shaped sample, the width is chosen two times larger, i.e., 0.250 mm, while the height is kept the same, i.e., 0.125 mm. Essentially, the chosen sample height is representative of the thickness of fibre-epoxy layers used in GLARE [78]. The diameter of the S2 glass fibres is $10 \mu\text{m}$. As illustrated in Figures 4.3 and 4.4, the internal material structure of the samples relates to a random fibre distribution that is geometrically periodic in the x_1 -direction.

4.4.2 Finite element model

The finite element model used for the microscale computations is plane-strain and thus is representative of fibres with a relatively large (actually infinite) length. The type of continuum elements and discrete elements used for simulating the failure response of the sample are chosen the same as for the numerical analyses performed in Chapter 3, see Section 3.2. In addition, the material parameters of the S2 glass fibre, the FM94 epoxy and the interface between fibres and epoxy are chosen the same as for the analyses in Chapter 3, see Table 3.2. However, the values of the ultimate normal and shear strengths of the fibre-epoxy interface are taken differently, namely $t_1^u = t_2^u = t_{adh}^u = 50 \text{ MPa}$, which is in correspondence with the adhesive strength of the fibre-epoxy interface being *equal* to the cohesive

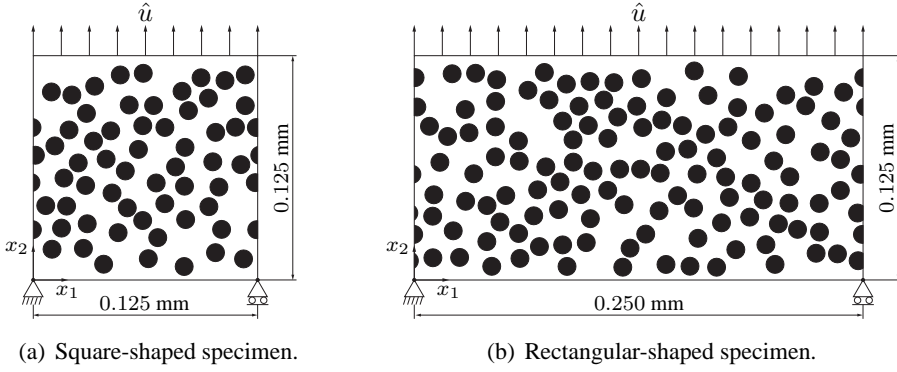


Figure 4.3: Geometry and boundary conditions of fibre-epoxy samples with a fibre volume fraction of 0.3. The diameter of the glass fibres is $10\mu\text{m}$.

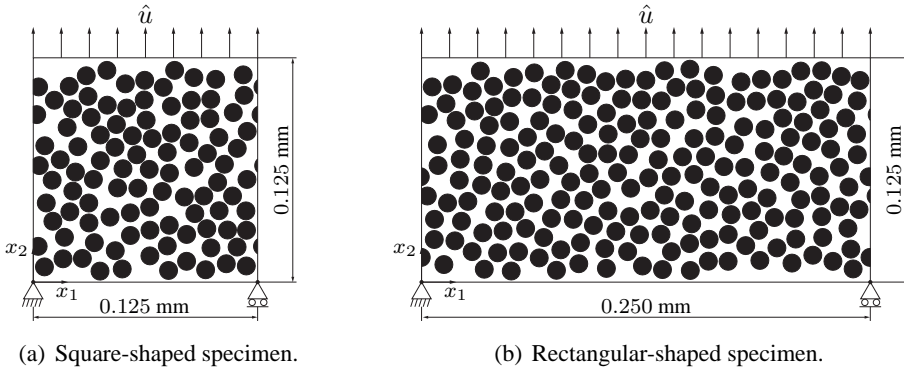


Figure 4.4: Geometry and boundary conditions of fibre-epoxy samples with a fibre volume fraction of 0.5. The diameter of the glass fibres is $10\mu\text{m}$.

Table 4.1: Number of elements used for samples of different size and volume fraction V_f , see Figures 4.3 and 4.4.

Sample shape	V_f	Continuum elements	Fibre-epoxy int. elems.	Epoxy int. elems.	Total
Square	0.3	5194	772	5001	10967
Square	0.5	9906	1679	6747	18332
Rectangular	0.3	10390	1549	10035	21974
Rectangular	0.5	19720	3360	13409	36489

strength of the epoxy material, $t_{adh}^u/t_{coh}^u = 1.0$. The number of continuum elements and interface elements used in the finite element meshes of the samples in Figures 4.3 and 4.4 are listed in Table 4.1. Note from this table that the number of elements used for modelling the rectangular sample is about two times the number of elements used for the square sample.

4.4.3 Influence of sample size and fibre volume fraction

The failure responses of the samples with the two different widths are mutually compared to assess the convergence of the numerical result upon an increasing microstructural sample volume. The mesoscopic traction-separation relation obtained after applying the homogenization method presented in Section 4.3.2 to the numerical results is shown in Figure 4.5. It can be observed that for both volume fractions the traction-separation responses of the square-shaped and rectangular-shaped samples are similar, indicating that the square-shaped sample is sufficiently large for being considered as an RVE. Essentially, the traction-separation responses closely follow the mode I traction-separation law of the epoxy material. This is due to the fact that the final failure crack develops mainly through the epoxy material and is mode I dominated (i.e., the orientation of the crack is more or less perpendicular to the direction of the tensile loading). This can be observed from Figures 4.6 and 4.7 for the square-shaped and rectangular shaped specimens with a fibre volume fraction of 0.3, respectively, and from Figures 4.8 and 4.9 for the square-shaped and rectangular shaped specimens with a fibre volume fraction

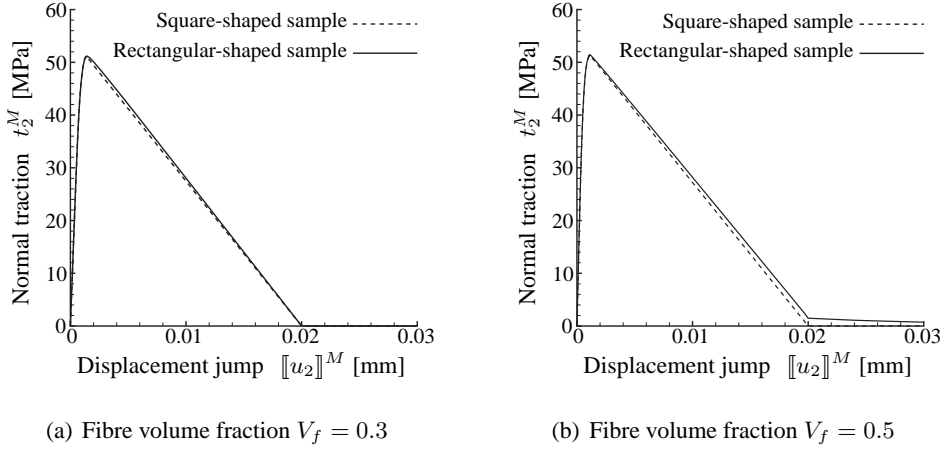


Figure 4.5: Mesoscopic traction-separation response for the square-shaped and rectangular-shaped samples shown in Figures 4.3 and 4.4. a) Fibre volume fraction $V_f = 0.3$. b) Fibre volume fraction $V_f = 0.5$.

of 0.5, respectively. In all these cases the crack clearly grows through the epoxy-rich area close to the top edge of the specimen. This position of the dominant failure crack is in correspondence with experimental observations on delamination failure in fibre-metal laminates, where mesoscale delamination between the prepreg layer and the aluminium layer at the microscale is represented by cracking through the fibre-low area located near the edge of the prepreg layer [78]. Since the fibres are hardly involved in this failure mechanism, a change in fibre volume fraction from 0.3 to 0.5 changes the sample response only minorly. Because the present analysis shows that the square-shaped sample can be considered as a representative volume element, this sample will be used for the forthcoming computations in this chapter.

4.4.4 Influence of imperfections on failure response

For studying how the homogenized traction-separation response is influenced by imperfections at fibre-epoxy interfaces, four different configurations are considered, see Figure 4.10. The fibre volume fraction of the sample is 0.3 and the

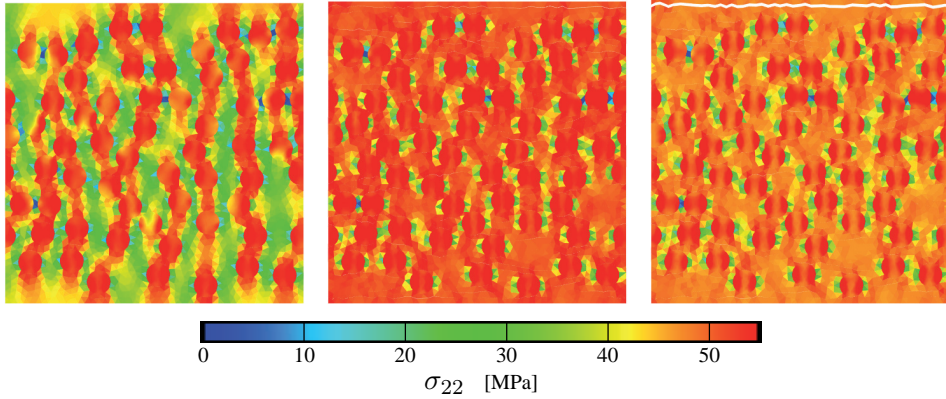


Figure 4.6: Axial normal stress σ_{22} depicted in deformed, cracked configurations, for the square-shaped sample in Figure 4.3(a) (which has a fibre volume fraction of 0.3). The deformed states are taken at relative displacements $\llbracket u_2 \rrbracket^M = 0.000816, 0.00146$ and 0.00257 mm, respectively.

imperfections are represented by a local absence of the adhesive bonding strength at specific fibre-epoxy interfaces. As illustrated in Figure 4.10, the four configurations considered are characterised by: (i) A single imperfection in the upper region of the sample (i.e., in the left-top quadrant), (ii) A single imperfection in the lower region of the sample (i.e., in the right-bottom quadrant), (iii) Two imperfections in the upper and lower regions of the sample (i.e., a combination of configurations (i) and (ii)), and (iv) Two imperfections in the upper and lower regions of the sample, where the upper imperfection coincides with that in configuration (i) and the lower imperfection is placed somewhat higher than that of configuration (ii).

The mesoscopic traction-separation response for the different configurations in Figure 4.10 is plotted in Figure 4.11. For comparison, the response of the specimen without imperfections, plotted in Figure 4.5(a), has also been included in this figure. The corresponding fracture patterns are depicted in Figures 4.12 to 4.15. For all studied configurations the imperfections clearly act as nucleation sites for crack development. In addition, their location typically is included in the

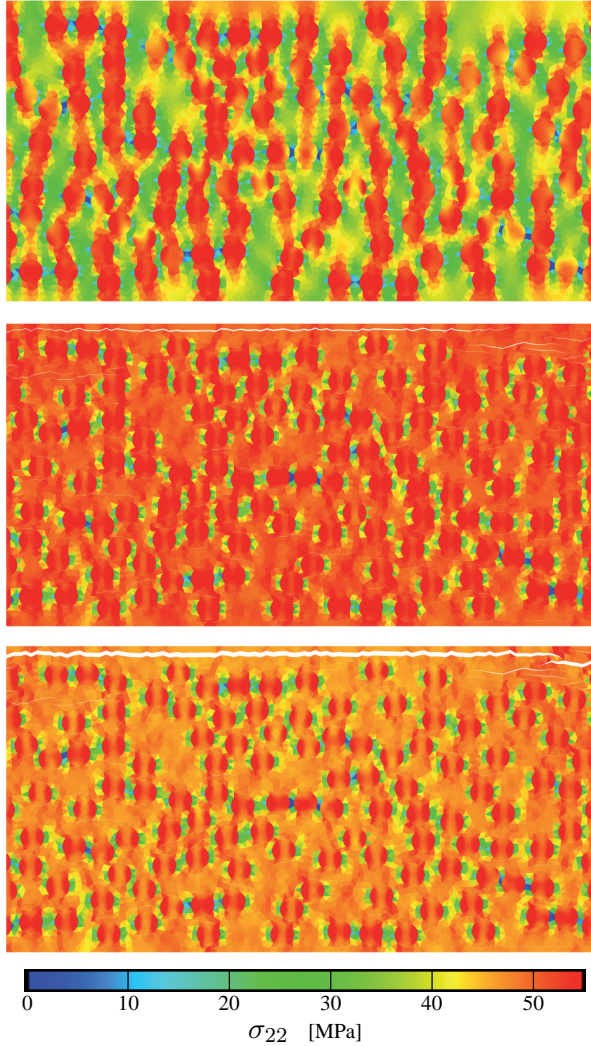


Figure 4.7: Axial normal stress σ_{22} depicted in deformed, cracked configurations, related to the rectangular-shaped sample in Figure 4.3(b) (which has a fibre volume fraction of 0.3). The deformed states are taken at relative displacements $[[u_2]]^M = 0.000815, 0.00186$ and 0.00314 mm, respectively.

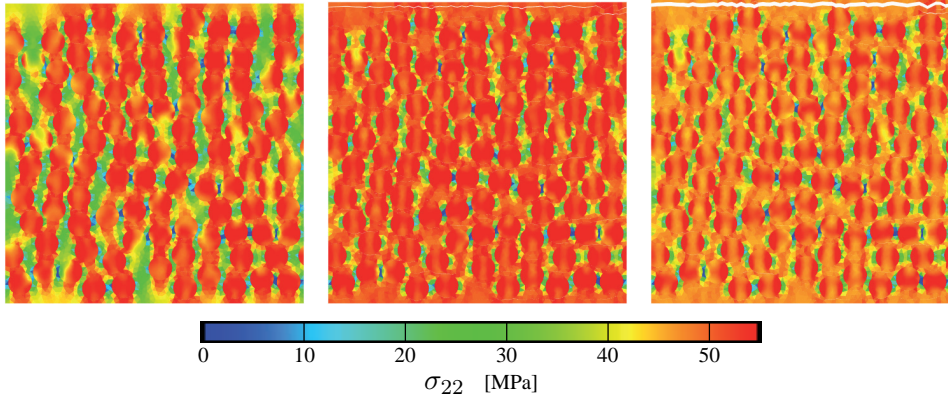


Figure 4.8: Axial normal stress σ_{22} depicted in deformed, cracked configurations, related to the square-shaped sample in Figure 4.4(a) (which has a fibre volume fraction of 0.5). The deformed states are taken at relative displacements $\llbracket u_2 \rrbracket^M = 0.000669, 0.00136$ and 0.00265 mm, respectively.

geometry of the dominant failure crack that develops upon complete failure of the fibre-epoxy specimen. An exception in this respect, however, is the imperfection located in the upper half of configuration (iii), see Figure 4.14; this imperfection initially acts as a nucleation site for cracking but eventually is not included in the geometry of the dominant failure crack, due to a local unloading behaviour during the loading process. This is an important difference with configuration (iv), where *both* imperfections are included in the geometry of the dominant failure crack, see Figure 4.15. The net result of this behaviour is that the total crack length of configuration (iv) is substantially larger than that of configuration (iii), which thus requires more energy dissipation in order to fail the sample. Correspondingly, the effective fracture toughness of configuration (iv) is larger than that of configuration (iii), see Figure 4.11, and also is larger than that of the sample without imperfections. Hence, it may be concluded that the presence of imperfections in a fibre-epoxy sample may have a positive effect on its effective failure characteristics.

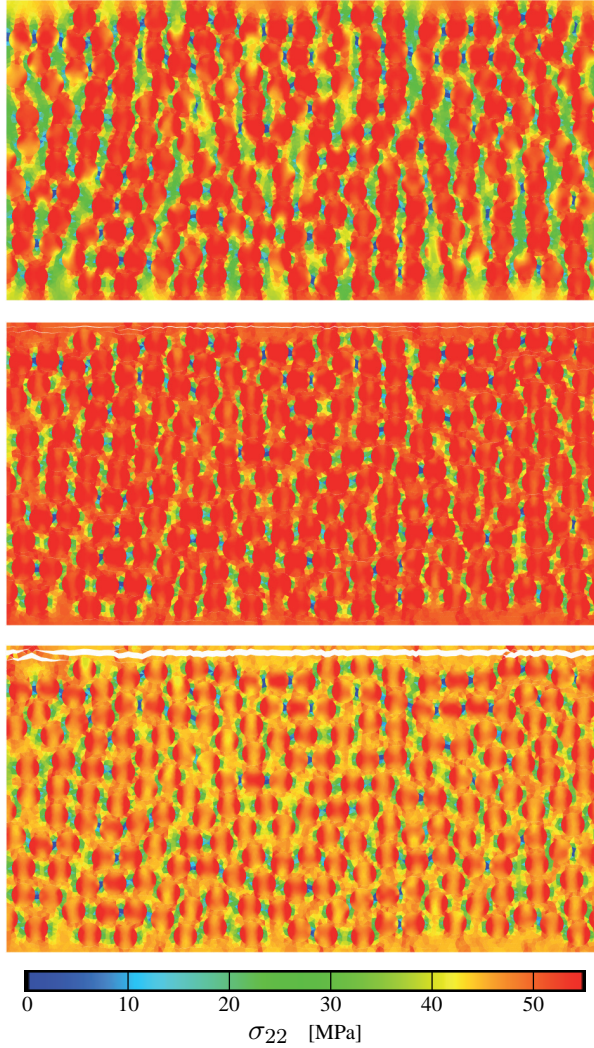


Figure 4.9: Axial normal stress σ_{22} depicted in deformed, cracked configurations, related to the rectangular-shaped sample in Figure 4.4(b) (which has a fibre volume fraction of 0.5). The deformed states are taken at relative displacements $[[u_2]]^M = 0.000669, 0.00134$ and 0.00345 mm, respectively.

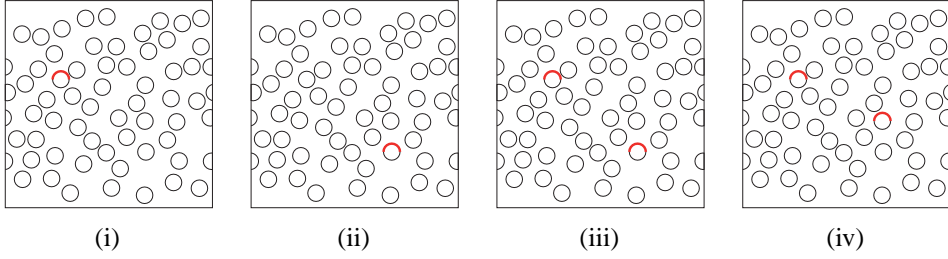


Figure 4.10: Four fibre-epoxy samples with different locations and/or number of imperfections. The fibre volume fraction of the sample is 0.3 and imperfections are indicated in red.

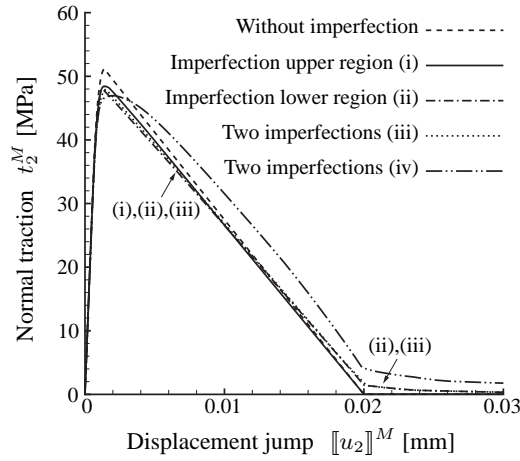


Figure 4.11: Mesoscopic traction-separation law corresponding to the square-shaped sample with a fibre volume fraction of 0.3 (shown in Figure 4.3(a)), plotted for a different number and position of imperfections.

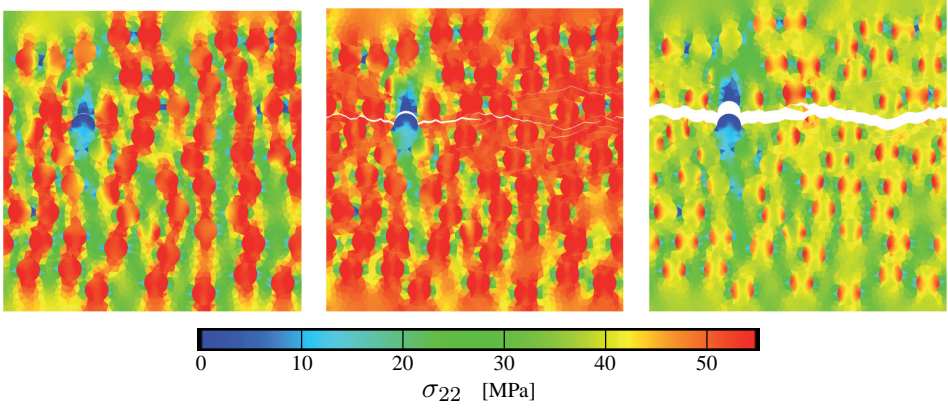


Figure 4.12: Axial normal stress σ_{22} depicted in deformed, cracked configurations, for case (i) in Figure 4.10. The deformed states are taken at $\llbracket u_2 \rrbracket^M = 0.821, 1.940$ and $5.985 \mu\text{m}$, respectively.

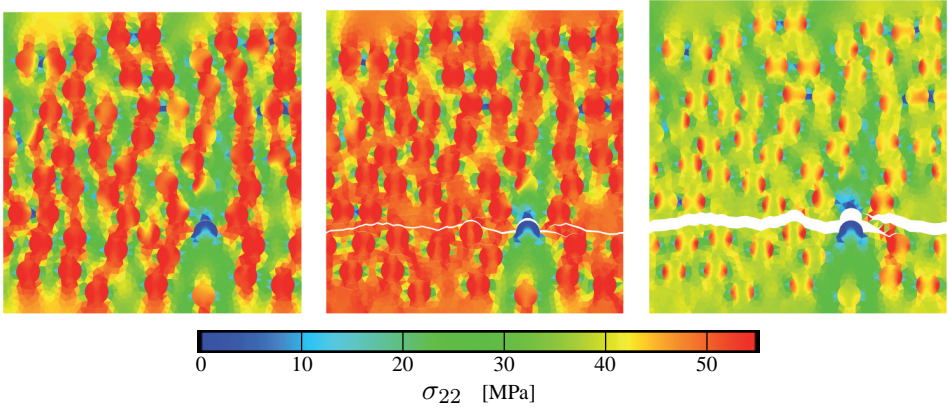


Figure 4.13: Axial normal stress σ_{22} depicted in deformed, cracked configurations, for case (ii) in Figure 4.10. The deformed states are taken at $\llbracket u_2 \rrbracket^M = 0.821, 1.854$ and $5.863 \mu\text{m}$, respectively.

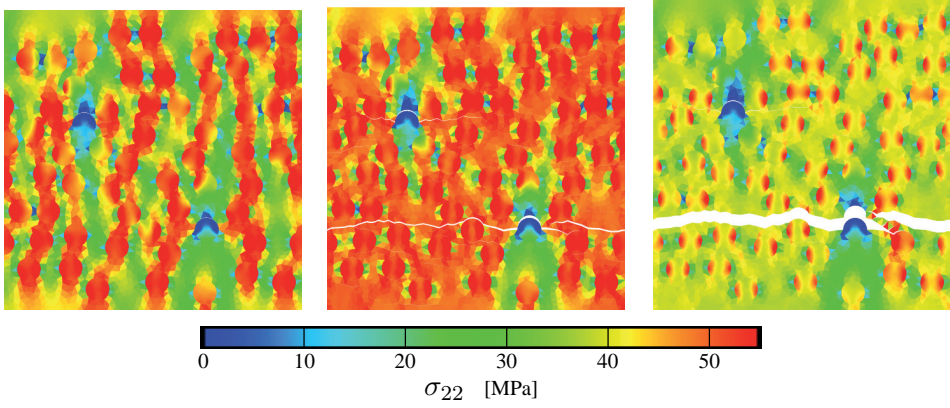


Figure 4.14: Axial normal stress σ_{22} depicted in deformed, cracked configurations, for case (iii) in Figure 4.10. The deformed states are taken at $\llbracket u_2 \rrbracket^M = 0.821, 1.985$ and $5.894 \mu\text{m}$, respectively.

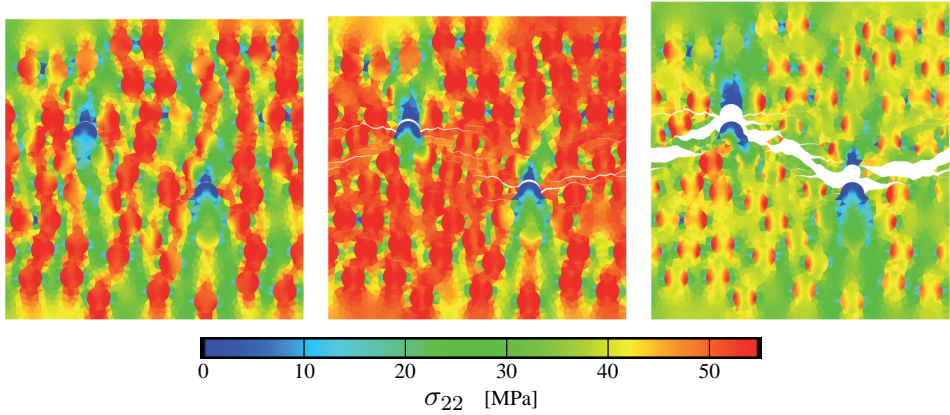


Figure 4.15: Axial normal stress σ_{22} depicted in deformed, cracked configurations, for the case (iv) in Figure 4.10. The deformed states are taken at $\llbracket u_2 \rrbracket^M = 0.822, 1.856$ and $8.041 \mu\text{m}$, respectively.

4.5 Conclusions

In this chapter a homogenization framework has been presented that links the microscale response of a fibre-epoxy sample to a mesoscale traction-separation curve that can be used for simulating the failure response of a (material point in a) cohesive interface. The formulation is based on Hill's averaging principle, which states that the spatial average of the virtual work at the microscale needs to be equal to the virtual work in a local material point of the mesoscale cohesive interface. Microscale numerical simulations are performed on a fibre-epoxy sample subjected to uniaxial tension. In the simulations the cohesive epoxy strength is taken equal to the adhesive strength of the fibre-epoxy interfaces. Two different sample sizes are analysed for two different values of the fibre volume fraction, $V_f = 0.3$ and 0.5 . The numerical response is characterised by a failure pattern that develops mainly through the epoxy matrix, as a result of which the failure response is not very sensitive to a change in fibre volume fraction. The numerical results converge upon increasing the sample size, confirming that the sample size then acts a representative volume element (RVE). The influence on the effective sample response by the number and position of initial imperfections within the specimen is also studied. The imperfections generally trigger crack nucleation, and their location typically is included in the geometry of the dominant crack that develops upon complete failure of the sample. As a result of this behaviour, imperfections can increase the length of the dominant failure crack (as compared to the crack length for a sample without imperfections), and thus may enhance the effective fracture toughness of the sample.

The present numerical homogenization technique computes the complex failure response of fibre-epoxy samples in a robust and accurate manner. Although the examples studied are limited to fibre-epoxy samples subjected to uniaxial tension, it is emphasised that the approach, in principle, can be applied to *any* type of material subjected to *arbitrary* combinations of tensile and shear loading.

Bibliography

- [1] R. C. Alderliesten. *Fatigue crack propagation and delamination growth in GLARE*. PhD thesis, Delft University of Technology, The Netherlands, 2005.
- [2] R. C. Alderliesten, M. Hagenbeek, J. J. Homan, P. A. Hooijmeijer, T. J. de Vries, and C. A. J. R. Vermeeren. Fatigue and damage tolerance of glare. *Applied Composite Materials*, 10(4):223–242, July 2003.
- [3] G. Alfano and M. A. Crisfield. Finite element interface models for the delamination analysis of laminated composites: Mechanical and computational issues. *International Journal For Numerical Methods In Engineering*, 50(7):1701–1736, 2001.
- [4] O. Allix and A. Corigliano. Modeling and simulation of crack propagation in mixed-modes interlaminar fracture specimens. *International Journal Of Fracture*, 77(2):111–140, 1996.
- [5] O. Allix, P. Ladeveze, and A. Corigliano. Damage analysis of interlaminar fracture specimens. *Composite Structures*, 31(1):61–74, 1995.
- [6] Z.P. Bažant and J.P. Planas. *Fracture and Size Effect in Concrete and other Quasibrittle Materials*. CRC Press, 1997.
- [7] A. Benssousan, J. L. Lions, and G. Papanicoulau. *Asymptotic analysis for periodic structures*. North Holland, Amsterdam, 1978.

- [8] J. L. Beuth. Cracking of thin bonded films in residual tension. *International Journal Of Solids And Structures*, 29(13):1657–1675, 1992.
- [9] M. Bischoff and E. Ramm. Shear deformable shell elements for large strains and rotations. *International Journal For Numerical Methods In Engineering*, 40(23):4427–4449, 1997.
- [10] B. Budiansky. On elastic moduli of some heterogeneous materials. *Journal Of The Mechanics And Physics Of Solids*, 13(4):223–227, 1965.
- [11] C. Chen, N. A. Fleck, and T. J. Lu. The mode I crack growth resistance of metallic foams. *Journal Of The Mechanics And Physics Of Solids*, 49(2):231–259, 2001.
- [12] V. Chohan and C. Galiotis. Effects of interface, volume fraction and geometry on stress redistribution in polymer composites under tension. *Composites Science And Technology*, 57(8):1089–1101, 1997.
- [13] M. V. Cid Alfaro, A. S. J. Suiker, R. de Borst, and J. J. C. Remmers. Analysis of fracture and delamination in laminates using 3D numerical modelling. *Engineering Fracture Mechanics*, 2008. (to appear).
- [14] B. N. Cox and D. B. Marshall. Crack initiation in fiber-reinforced brittle laminates. *Journal Of The American Ceramic Society*, 79(5):1181–1188, 1996.
- [15] T. de Jong. *Forming of laminates*. PhD thesis, Delft University of Technology, The Netherlands, 2004.
- [16] T. W. de Jong, E. Kroon, and J. Sinke. Fibre Metal Laminates an Introduction. In A. Vlot and J. W. Gunnink, editors, *Formability*, chapter 22, pages 337–354. Kluwer Academic Publishers, Dordrecht, The Netherlands, 2001.
- [17] T. J. de Vries. *Blunt and sharp notch behaviour of GLARE laminates*. PhD thesis, Delft University of Technology, The Netherlands, 2001.
- [18] A. Dollar and P. S. Steif. Stresses in fibers spanning an infinite matrix crack. *International Journal Of Solids And Structures*, 27(8):1011–1024, 1991.

-
- [19] W. J. Drugan and J. R. Willis. A micromechanics-based nonlocal constitutive equation and estimates of representative volume element size for elastic composites. *Journal of the Mechanics and Physics of Solids*, 44(4):497–524, 1996.
- [20] J. Dundurs. Edge-bonded dissimilar orthogonal elastic wedges. *Journal Of Applied Mechanics (ASME)*, 36:650–652, 1969.
- [21] R. Ermel, T. Beck, and E. Kerscher. Analysis of failure behaviour of carbon/carbon composite made by chemical vapour infiltration considering fibre, matrix and interface properties. *International Journal Of Materials Research*, 97(10):1401–1409, 2006.
- [22] J. D. Eshelby. The determination of the elastic field of an ellipsoidal inclusion, and related problems. *Proceedings Of The Royal Society Of London Series A-Mathematical And Physical Sciences*, 241(1226):376–396, 1957.
- [23] E. K. Gamstedt and B. A. Sjogren. Micromechanisms in tension-compression fatigue of composite laminates containing transverse plies. *Composites Science And Technology*, 59(2):167–178, 1999.
- [24] S. Ghosh, K. Lee, and S. Moorthy. Multiple scale analysis of heterogeneous elastic structures using homogenization theory and voronoi cell finite element method. *International Journal of Solids and Structures*, 32(1):27–62, 1995.
- [25] S. Ghosh, K. Lee, and S. Moorthy. Two scale analysis of heterogeneous elastic-plastic materials with asymptotic homogenization and voronoi cell finite element model. *Computer Methods in Applied Mechanics and Engineering*, 132(1-2):63–116, 1996.
- [26] S. Ghosh, Y. Ling, B. Majumdar, and R. Kim. Interfacial debonding analysis in multiple fiber reinforced composites. *Mechanics Of Materials*, 32(10):561–591, 2000.

- [27] J. M. Guedes and N. Kikuchi. Preprocessing and postprocessing for materials based on the homogenization method with adaptive finite-element methods. *Computer Methods In Applied Mechanics And Engineering*, 83(2):143–198, 1990.
- [28] M. Hagenbeek. *Characterization of fibre metal laminates under thermo-mechanical loadings*. PhD thesis, Delft University of Technology, The Netherlands, 2005.
- [29] F. Hashagen. *Numerical analysis of failure mechanisms in fibre metal laminates*. PhD thesis, Delft University of Technology, The Netherlands, 1998.
- [30] F. Hashagen and R. de Borst. Numerical assessment of delamination in fibre metal laminates. *Computer Methods In Applied Mechanics And Engineering*, 185(2-4):141–159, 2000.
- [31] Z. Hashin and S. Shtrikman. A variational approach to the theory of the elastic behaviour of multiphase materials. *Journal of the Mechanics and Physics of Solids*, 11(2):127–140, 1963.
- [32] M. Y. He, A. G. Evans, and J. W. Hutchinson. Crack deflection at an interface between dissimilar elastic materials: Role of residual stresses. *International Journal Of Solids And Structures*, 31(24):3443–3455, 1994.
- [33] O. M. Heeres, Suiker A. S. J., and de Borst R. A comparison between the Perzyna viscoplastic model and the consistency viscoplastic model. *European Journal of Mechanics A/Solids.*, 21:1–12, 2002.
- [34] R. Hill. Theory of mechanical properties of fibre-strengthened materials—iii. self-consistent model. *Journal of the Mechanics and Physics of Solids*, 13(4):189–198, 1965.
- [35] R. Hill. The essential structure of constitutive laws for metal composites and polycrystals. *Journal Of The Mechanics And Physics Of Solids*, 15(2):79–95, 1967.

-
- [36] S. Ho and Z. Suo. Tunneling cracks in constrained layers. *Journal Of Applied Mechanics (ASME)*, 60(4):890–894, 1993.
- [37] T. Hobbiebrunken, M. Hojo, T. Adachi, C. De Jong, and B. Fiedler. Evaluation of interfacial strength in CF/epoxies using FEM and in-situ experiments. *Composites Part A-Applied Science And Manufacturing*, 37(12):2248–2256, 2006.
- [38] J. C. Honoré, P. Mélé, and L. Flandin. Influence of fibre clustering on the transverse mechanical behaviour of polypropylene/glass fibre composites: experimental approach and modelling. *Journal Of Physics D-Applied Physics*, 40(21):6768–6777, 2007.
- [39] M. Hori and S. Nemat-Nasser. Double-inclusion model and overall moduli of multi-phase composites. *Mechanics of Materials*, 14(3):189–206, 1993.
- [40] <http://www.innoveermetpolymeer.nl/>.
- [41] J. W. Hutchinson and A. G. Evans. Mechanics of materials: Top-down approaches to fracture. *Acta Materialia*, 48(1):125–135, 2000.
- [42] J. W. Hutchinson, M. E. Mear, and J. R. Rice. Crack paralleling an interface between dissimilar materials. *Journal Of Applied Mechanics (ASME)*, 54(4):828–832, 1987.
- [43] J. W. Hutchinson and Z. Suo. Mixed mode cracking in layered materials. *Advances In Applied Mechanics*, 29:63–191, 1992.
- [44] H. M. Jensen. Mixed mode interface fracture criteria. *Acta Metallurgica Et Materialia*, 38(12):2637–2644, 1990.
- [45] V. Kouznetsova, W. A. M. Brekelmans, and F. P. T. Baaijens. An approach to micro-macro modeling of heterogeneous materials. *Computational Mechanics*, 27(1):37–48, 2001.
- [46] M. A. Leaity, P. A. Smith, M. G. Bader, and P. T. Curtis. The behavior of cross-ply hybrid matrix composite laminates. Part 1: Experimental results. *Composites*, 23(6):387–395, 1992.

- [47] T. J. Lu. Crack branching in all-oxide ceramic composites. *Journal Of The American Ceramic Society*, 79(1):266–274, 1996.
- [48] K. Matouš, M. G. Kulkarni, and P. H. Geubelle. Multiscale cohesive failure modeling of heterogeneous adhesives. *Journal of the Mechanics and Physics of Solids*, 56(4):1511–1533, 2008.
- [49] C. Miehe. Numerical computation of algorithmic (consistent) tangent moduli in large-strain computational inelasticity. *Computer Methods In Applied Mechanics And Engineering*, 134(3-4):223–240, 1996.
- [50] C. Miehe and A. Koch. Computational micro-to-macro transitions of discretized microstructures undergoing small strains. *Archive Of Applied Mechanics*, 72(4-5):300–317, 2002.
- [51] C. Miehe, J. Schroder, and J. Schotte. Computational homogenization analysis in finite plasticity. Simulation of texture development in polycrystalline materials. *Computer Methods In Applied Mechanics And Engineering*, 171(3-4):387–418, 1999.
- [52] F. París, E. Correa, and V. Mantic. Kinking of transversal interface cracks between fiber and matrix. *Journal Of Applied Mechanics-Transactions Of The Asme*, 74(4):703–716, 2007.
- [53] H. Parisch. A continuum-based shell theory for non-linear applications. *International Journal for Numerical Methods in Engineering*, 38(11):1855–1883, 1995.
- [54] A. Pérez-Foguet, A. Rodríguez-Ferran, and A. Huerta. Numerical differentiation for local and global tangent operators in computational plasticity. *Computer Methods In Applied Mechanics And Engineering*, 189(1):277–296, 2000.
- [55] A. W. Pryce and P. A. Smith. Behavior of unidirectional and crossply ceramic matrix composites under quasi-static tensile loading. *Journal Of Materials Science*, 27(10):2695–2704, 1992.

-
- [56] J. J. C. Remmers. *Discontinuities in materials and structures*. PhD thesis, Delft University of Technology, The Netherlands, 2006.
- [57] J. C. J. Schellekens and R. de Borst. A non-linear finite element approach for the analysis of mode-I free edge delamination in composites. *International Journal of Solids and Structures*, 30(9):1239–1253, 1993.
- [58] J. C. J. Schellekens and R. de Borst. On the numerical-integration of interface elements. *International Journal For Numerical Methods In Engineering*, 36(1):43–66, 1993.
- [59] C. Shet and N. Chandra. Analysis of energy balance when using cohesive zone models to simulate fracture processes. *Journal Of Engineering Materials And Technology (ASME)*, 124(4):440–450, 2002.
- [60] D. J. Shim, R. C. Alderliesten, S. M. Spearing, and D. A. Burianek. Fatigue crack growth prediction in GLARE hybrid laminates. *Composites Science And Technology*, 63(12):1759–1767, 2003.
- [61] M. Stroeven and P. Stroeven. Computer-simulated internal structure of materials. *Acta Stereologica*, 15:247–252, 1996.
- [62] A. S. J. Suiker and N. A. Fleck. Crack tunneling and plane-strain delamination in layered solids. *International Journal Of Fracture*, 125(1-2):1–32, 2004.
- [63] A. S. J. Suiker and N. A. Fleck. Modelling of fatigue crack tunneling and delamination in layered composites. *Composites Part A-Applied Science And Manufacturing*, 37(10):1722–1733, 2006.
- [64] A. S. J. Suiker and S. Turteltaub. Computational modelling of plasticity induced by martensitic phase transformations. *International Journal For Numerical Methods In Engineering*, 63(12):1655–1693, 2005.
- [65] Z. Suo, S. Ho, and X. Gong. Notch ductile-to-brittle transition due to localized inelastic band. *Journal Of Engineering Materials And Technology-Transactions Of The Asme*, 115(3):319–326, 1993.

- [66] Z. Suo and J. W. Hutchinson. Interface crack between two elastic layers. *International Journal Of Fracture*, 43:1–18, 1990.
- [67] P. M. Suquet. *Local and global aspects in the mathematical theory of plasticity*. In Sawczuk, A. and Bianchi, G., eds, *Plasticity today: modelling, methods and applications*, pages 279–310. Elsevier Applied Science Publishers, London, 1985.
- [68] T. Takamatsu, T. Matsumura, N. Ogura, T. Shimokawa, and Y. Kakuta. Fatigue crack growth properties of a GLARE 3-5/4 fiber metal laminate. *Engineering Fracture Mechanics*, 63(3):253–272, 1999.
- [69] M. G. A. Tijssens, L. J. Sluys, and E. van der Giessen. Simulation of fracture of cementitious composites with explicit modeling of microstructural features. *Engineering Fracture Mechanics*, 68(11):1245–1263, 2001.
- [70] M. G. A. Tijssens, E. van der Giessen, and L. J. Sluys. Simulation of mode I crack growth in polymers by crazing. *International Journal Of Solids And Structures*, 37(48-50):7307–7327, 2000.
- [71] J. Tong, F. J. Guild, S. L. Ogin, and P. A. Smith. On matrix crack growth in quasi-isotropic laminates - I. Experimental investigation. *Composites Science And Technology*, 57(11):1527–1535, 1997.
- [72] A. Turon, P. P. Camanho, J. Costa, and C. G. Davila. A damage model for the simulation of delamination in advanced composites under variable-mode loading. *Mechanics Of Materials*, 38(11):1072–1089, 2006.
- [73] V. Tvergaard and J. W. Hutchinson. The relation between crack growth resistance and fracture process parameters in elastic-plastic solids. *Journal Of The Mechanics And Physics Of Solids*, 40(6):1377–1397, 1992.
- [74] V. Tvergaard and J. W. Hutchinson. Effect of T-stress on mode I crack growth resistance in a ductile solid. *International Journal Of Solids And Structures*, 31(6):823–833, 1994.

-
- [75] J. van den Brande and J. Sinke. FIMELAS - Numerical modelling of fibre metal laminates: Microscopic damage models. Technical Report B2V-04-02, Delft University of Technology, The Netherlands, 2004.
- [76] C. A. J. R. Vermeeren. *The residual strength of fibre metal laminates*. PhD thesis, Delft University of Technology, The Netherlands, 1995.
- [77] A. Vlot. *Low-velocity impact loading on fibre reinforced aluminium laminates (ARALL) and other aircraft sheet materials*. PhD thesis, Delft University of Technology, The Netherlands, 1991.
- [78] A. Vlot and Gunnink J. W., editors. *Fibre Metal Laminates - An Introduction*. Kluwer Academic Publishers, 2001.
- [79] X. P. Xu and A. Needleman. Void nucleation by inclusion debonding in a crystal matrix. *Modelling And Simulation In Materials Science And Engineering*, 1(2):111–132, January 1993.
- [80] X. P. Xu and A. Needleman. Numerical simulations of fast crack growth in brittle solids. *Journal Of The Mechanics And Physics Of Solids*, 42(9):1397–1407, 1994.
- [81] L. Zhang, L. J. Ernst, and H. R. Brouwer. Transverse behaviour of a unidirectional composite (glass fibre reinforced unsaturated polyester) part i. influence of fibre packing geometry. *Mechanics Of Materials*, 27(1):13–36, 1998.

Summary

Multiscale analyses of fibre metal laminates

The advance of composites used in aerospace, civil and biomechanical engineering and other technology branches over the last decades has led to a substantial increase in the application of these materials. In addition, the search for new and improved materials in aerospace industry has stimulated the development of hybrid materials partly made out of composites, such as Fibre-Metal Laminates (FMLs). These materials are composed of alternatively stacked aluminium and fibre-reinforced composite layers such that the best features of both constituents are combined. FMLs also have additional advantages over conventional monolithic aluminium alloys and fibre-reinforced composites, such as an excellent fatigue and damage-tolerance behaviour. Furthermore, this class of materials possesses good fire, impact, damping, insulation and corrosion-resistance properties, which has led to their application in the construction of the upper part of the fuselage for the Airbus A380.

To ensure a maximal reliability under service conditions, the failure mechanisms of FMLs must be well understood. The main mesoscale failure mechanisms that endanger their overall reliability are delamination between adjacent plies, cracking, and plasticity in individual metal layers. Important failure mechanisms at the microscale are debonding of fibres, fibre breakage, pull-out of broken fibres and crack growth in the epoxy matrix.

Finite element simulations serve as an important tool for understanding the mechanical failure behaviour of FMLs in engineering applications. However, the performance of a direct numerical analysis of an engineering structure (e.g., an aircraft wing), where all features of the underlying heterogeneous microstructure are accounted for explicitly, requires an extremely fine finite element mesh and thus an impractical amount of computational time. A more efficient approach is to study engineering structures with the aid of mesoscale material models that account for the underlying microstructure in an average sense. The average prop-

erties in the mesoscale model can be computed using a numerical homogenization approach, where the microstructural stresses and deformations are averaged over a representative material volume. The present thesis comprises a detailed study of the failure behaviour of fibre-metal laminates at the meso- and microscale levels, and proposes a numerical homogenization framework that links specific failure mechanisms at these two levels of observation.

In Chapter 2 of the thesis the static failure behaviour of the fibre-metal laminate GLARE under uniaxial tension is examined using three-dimensional finite element simulations. GLARE laminates are characterised by reinforcement through glass fibres. The configuration analysed is a centre-cracked tensile specimen composed of two aluminium layers sandwiching a cross-plyed, fibre-epoxy layer. The mesoscale crack growth (within plies) and delamination growth (at ply interfaces) is simulated by means of interface elements equipped with a mixed-mode damage model. The mode-mixity in the interface damage model is derived from an energy criterion typically used in linear elastic fracture mechanics studies. The damage kinetic law is rate-dependent, in order to simulate rate effects during interfacial delamination and to avoid numerical convergence problems due to crack bifurcations. The numerical implementation of the interface damage model is based on a backward Euler approach.

In the boundary value problem studied, the failure responses of GLARE specimens containing elastic aluminium layers and GLARE specimens containing elasto-plastic aluminium layers are compared. The development of plastic deformations in the aluminium layers stabilizes the effective failure response, and increases the residual strength of the laminate. For a 'quasi-brittle' GLARE specimen with elastic aluminium layers, the residual strength is mainly governed by the toughness for interfacial delamination, and is in close correspondence with the residual strength obtained from a closed-form expression derived from energy considerations. Conversely, for a 'ductile' GLARE specimen with elasto-plastic aluminium layers, the residual strength is also determined by the relation between the fracture strength and the yield strength of the aluminium. The amount of constraint by the horizontal displacements at the vertical specimen edges has a moderate to small effect on the residual strength of the laminate. Furthermore, the ultimate laminate strength is lower for a larger initial crack length, and shows to

be in good correspondence with experimental values.

At the microscale the failure response of FMLs is strongly determined by a combination of complex fracture and delamination modes within the fibre-epoxy layers. Chapter 3 studies the microscale failure behaviour of unidirectional fibre-epoxy samples loaded under uniaxial tension, where failure is characterised by adhesive debonding between the fibres and the epoxy matrix and by cracking in the epoxy matrix. The analyses are performed through two-dimensional numerical simulations assuming plane-strain conditions. The failure mechanisms are modelled in a discrete fashion, using interface elements furnished with the mixed-mode damage model presented in Chapter 2. To allow for arbitrary cracking in the epoxy material, interface elements are introduced in between all continuum elements constructing the epoxy matrix. Similarly, fibre-matrix debonding is simulated by placing interface elements in between the fibres and the epoxy matrix. With this so-called cohesive surface methodology, the growth of cracks is straightforwardly determined by the stress field generated at crack tips. Additionally, coalescence and branching of cracks emerges as a natural outcome of the simulations, without a need for additional selection criteria. Consequently, using a sufficiently fine, randomly oriented mesh, the fracture response of microstructures can be predicted without an a-priori assumption of the cracking path. The results of the simulations performed at the microscale show that the effective sample response and the corresponding failure pattern are strongly determined by the ratio between the fibre-epoxy interfacial strength and the epoxy strength. Essentially, for a relatively weak fibre-epoxy interface the overall failure behaviour of the sample is characterised both by fibre-debonding and epoxy cracking. Conversely, when the epoxy is stronger than the fibre-epoxy interface, the overall failure behaviour of the sample is determined by epoxy cracking only.

In addition, the ratio between the fibre-epoxy interfacial fracture toughness and the epoxy fracture toughness does have a substantial influence on the effective sample response, but its effect on the corresponding failure pattern is small. The microscale computations further show that the fibre volume fraction only influences the sample failure response if the fibre-epoxy interface is weaker than the epoxy matrix. Moreover, the fibre distribution has a minor influence on the failure response of the fibre-epoxy sample when the fibre volume fraction is relatively

high. The failure patterns obtained by the numerical simulations are supported by experimental results presented in the literature.

In Chapter 4 the failure responses of a fibre-matrix composite at the meso- and microscales are linked by means of a computational homogenization procedure. The traction-separation law in a material point of a mesoscale cohesive interface is found by spatial averaging of the responses in the material points of the corresponding microscale sample. This is done applying Hill's averaging principle, which states that the spatial average of the virtual work at the microscale needs to be equal to the virtual work in a local material point at the mesoscale.

The microscale simulations consider a fibre-epoxy sample loaded under uniaxial tension, where the adhesive strength between the fibres and the epoxy is taken equal to the cohesive strength of the epoxy. The effect of the sample width on the effective failure response is studied analysing two different sample widths. The effective failure response is hardly influenced by a change in sample size since the final (mode I dominated) failure crack runs more or less straight across the sample width. Furthermore, the crack pattern forms mainly through the epoxy, as a result of which variations of the fibre volume fraction and the fibre distribution only have a minor effect on the homogenized traction-separation response. The introduction of an initial imperfection in the sample (as created by a local absence of adhesion between fibre(s) and epoxy) typically reduces the ultimate strength of the sample, and for specific configurations may lead to a higher overall sample toughness. The higher toughness can be ascribed to an extension of the microscale cracking path, as a result of which more energy needs to be dissipated for reaching complete failure of the fibre-epoxy sample.

Marcela Cid Alfaro
October 2008

Samenvatting

Multischaal analyses van vezel-metaallaminaten

De vooruitgang van composietmaterialen gebruikt in de luchtvaart- en ruimtevaarttechniek, civiele bouw, biomechanica en andere takken van techniek hebben de afgelopen decennia geleid tot een significante toename in de toepassing van deze materialen. Daarbij heeft de zoektocht naar nieuwe en verbeterde materialen in de luchtvaartindustrie geleid tot de ontwikkeling van hybride materialen, die deels zijn vervaardigd uit composieten. Een voorbeeld van een type hybride materiaal is het vezel-metaallaminaat. Dit materiaal is vervaardigd uit aluminium lagen en vezelversterkte composietlagen die afwisselend zijn gestapeld om zo de beste eigenschappen van de individuele componenten te combineren. Vezel-metaallaminaten hebben daarbij aanvullende voordelen ten aanzien van monolithisch aluminium en vezelversterkte composieten, zoals een uitstekende vermoeingsweerstand en een goede verdraagzaamheid van schade. Daarbij komt dat deze klasse van materialen goede vuurwerings-, inslag-, corrosie-, isolatie- en dempingseigenschappen heeft, wat ertoe geleid heeft dat vezel-metaallaminaten constructief zijn toegepast in het bovenste gedeelte van de romp van de Airbus A380.

Om een optimale betrouwbaarheid tijdens de operationele levensduur te kunnen garanderen dienen de bezwijkmechanismen van vezel-metaallaminaten goed te worden begrepen. De voornaamste bezwijkmechanismen op mesoschaal die de algehele betrouwbaarheid in gevaar brengen zijn delaminatie tussen aangrenzende lagen, scheurvorming, en plastische vervorming in individuele metaallagen. Op microschaal zijn de belangrijkste bezwijkmechanismen het loskomen, uittrekken en breken van vezels, en scheurgroei in de epoxylaag.

Berekeningen met de eindige-elementenmethode dienen als een belangrijk gereedschap om het bezwijkgedrag van vezel-metaallaminaten te begrijpen. Het uitvoeren van een directe numerieke analyse op een constructie (bijvoorbeeld een vliegtuigvleugel) waarbij alle kenmerken van de onderliggende heterogene microstructuur expliciet worden meegenomen vereist desalniettemin een zeer fijn

eindig-elementenrooster, hetgeen leidt tot onaanvaardbaar lange reketijden. Het is efficiënter om constructies te berekenen met behulp van modellen geformuleerd op mesoschaalniveau, waarbij de informatie van de onderliggende microschaal wordt meegenomen op gemiddelde wijze. De gemiddelde eigenschappen in het mesoscopische model kunnen worden berekend met behulp van een numerieke homogenisatiemethode, waarbij de spanningen en vervormingen op microschaal worden gemiddeld over een representatief materiaalvolume. Dit proefschrift omvat een gedetailleerde studie van het bezwijkgedrag van vezel-metaallaminaten op mesoscopische en microscopische niveaus, en presenteert een numerieke homogenisatiemethode die specifieke bezwijkmechanismen op deze twee observatieschalen met elkaar koppelt.

In hoofdstuk 2 van het proefschrift is het statische bezwijkgedrag van het vezel-metaallaminaat GLARE onder éénassige trek bestudeerd door middel van driedimensionale eindige-elementensimulaties. Het GLARE laminaat wordt gekenmerkt door een versterking door glasvezels. De configuratie die is geanalyseerd is een proefstuk uitgerust met een initiële centrische scheur welke op trek wordt belast. Het proefstuk bestaat uit twee aluminium lagen met daartussen een vezel-epoxy laag, waarbij de vezels kruislings zijn georiënteerd. Op mesoschaal worden scheurgroei en delaminatie gesimuleerd door gebruik te maken van grenslaagelementen die zijn uitgerust met een trek-schuif schademodel. De formulering van de trek-schuif verhouding is afgeleid vanuit een energiecriterium dat gebruikelijk is in de lineair elastische breukmechanica. De kinetische wet voor schade is snelheidsafhankelijk, zodat snelheidseffecten tijdens delaminatie kunnen worden gesimuleerd en numerieke convergentieproblemen ten gevolge van vertakking van scheuren kunnen worden voorkomen. De numerieke implementatie van het schademodel is gebaseerd op een achterwaartse Euler methode.

In het bestudeerde randwaardeprobleem is het bezwijkgedrag van GLARE vergeleken voor proefstukken waarbij het aluminium alleen elastisch kan vervormen, en waarbij het aluminium zowel elastisch als plastisch kan vervormen. Het ontstaan van plastische vervormingen in het aluminium heeft een stabiliserend effect op het algehele bezwijkgedrag en verhoogt de reststerkte van het laminaat. Voor het 'quasi-brosse' laminaat, waarbij het aluminium alleen elastisch kan vervormen, wordt de reststerkte in hoofdzaak bepaald door de delaminatietaaiheid.

Deze reststerkte is in overeenstemming met de waarde die wordt verkregen uit een uitdrukking die is afgeleid op basis van energiebeschouwingen. Daarentegen wordt de reststerkte in het 'quasi-ductiele' laminaat, waarin het aluminium ook plastisch kan vervormen, aanvullend bepaald door de relatie tussen de breuksterkte en de vloeigrens van het aluminium. De beperking die wordt opgelegd op de horizontale verplaatsing van de verticale randen van het proefstuk heeft een matige tot kleine invloed op de reststerkte van het laminaat. Verder is de maximale sterkte van het laminaat lager wanneer de initiële centrische scheur groter is, en is deze in goede overeenstemming met experimentele data.

Het bezwijkgedrag van vezel-metaallaminaten wordt op microschaal sterk bepaald door een combinatie van complexe breuk- en delaminatiemechanismen binnen de vezel-epoxylagen. Hoofdstuk 3 bestudeert het microscopische bezwijkgedrag van vezel-epoxylagen onder éénassige trek, waarbij de vezelrichting loodrecht op de belastingsrichting staat. Het bezwijkmechanisme kenmerkt zich door het loslaten van vezels in de epoxy matrix en door scheurvorming in de epoxy matrix. De analyse is uitgevoerd door middel van tweedimensionale numerieke simulaties met de aanname van een vlakke vervormingstoestand. De bezwijkmechanismen zijn op een discrete manier gemodelleerd, door het toepassen van grenslaagelementen uitgerust met het trek-schuif schademodel gepresenteerd in hoofdstuk 2. De grenslaagelementen zijn geïntroduceerd tussen alle continuüm-elementen, om zodoende willekeurige scheurvorming in de epoxy materiaal mogelijk te maken. Op overeenkomstige wijze is de onthechting tussen vezels en matrix gesimuleerd door ter plaatse grenslaagelementen aan te brengen. Met deze zogenaamde "methodologie van hechtende oppervlakten" wordt het ontstaan en groeien van scheuren direct bepaald uit het spanningsveld gegenereerd rond een scheurtip. Daarbij worden het samenkomen en vertakken van scheuren op een natuurlijke manier beschreven in de formulering, zodat hiervoor geen extra condities noodzakelijk zijn. Hierdoor kan met een voldoende fijn, willekeurig georiënteerd eindig-elementenrooster het scheurgedrag van microstructuren worden bepaald zonder dat vooraf een scheurpad hoeft te worden aangenomen. De resultaten van de simulaties op microschaal laten zien dat de algehele responsie van het proefstuk en het bijbehorende bezwijkpatroon sterk gekoppeld zijn aan de verhouding tussen de epoxysterkte en de aanhechtingssterkte tussen vezels

en epoxy. Feitelijk wordt voor een relatief zwakke verbinding tussen de epoxy en de vezels het algehele bezwijkgedrag bepaald door zowel het loslaten van de vezels als scheurvorming in de epoxy. Daartegenover wordt voor een relatief sterke verbinding tussen de epoxy en de vezels het algehele bezwijkgedrag alleen bepaald door scheurvorming in de epoxy.

De verhouding van de breuktaaiheid tussen de vezels en de epoxy en de breuktaaiheid van de epoxy heeft welliswaar een substantiële invloed op de algehele responsie van het proefstuk, maar de invloed op het corresponderende scheurpatroon is klein. De berekeningen op microschaalniveau laten ook zien dat de volumefractie van de vezels alleen invloed heeft op de bezwijkresponsie van het proefstuk indien de aanhechtingssterkte tussen vezels en epoxy lager is dan de breuksterkte van de epoxy. Bovendien heeft de vezelverdeling een kleine invloed op de bezwijkresponsie van het vezel-epoxy proefstuk wanneer de volumefractie van de vezels relatief hoog is. De bezwijkpatronen verkregen met de numerieke simulaties worden ondersteund door experimentele resultaten gepresenteerd in de vakliteratuur.

In hoofdstuk 4 is het bezwijkgedrag van het vezel-matrix composiet op de micro- en mesoschalen gekoppeld door middel van een numerieke homogenisatieprocedure. De tractie-separatie-wet in een materiaalpunt van een cohesieve grenslaag op mesoschaal is gevonden door het ruimtelijk middelen van de responsies in de materiaalpunten van een proefstuk op microschaal. Dit is gedaan door het toepassen van "Hill's middelingsprincipe", welk stelt dat het ruimtelijke gemiddelde van de virtuele arbeid op microschaal overeen moet komen met de virtuele arbeid in een lokaal materiaalpunt op mesoschaal.

De simulaties op microschaal beschouwen een vezel-epoxy proefstuk belast onder éénassige trek, waarbij de aanhechtingssterkte tussen de vezels en de epoxy gelijk genomen is aan de sterkte van de epoxy. De invloed van de breedte van het proefstuk op het effectieve bezwijkgedrag is bestudeerd door proefstukken met twee verschillende breedtes te beschouwen. De effectieve bezwijkresponsie wordt nauwelijks beïnvloed door een verandering in proefstukbreedte omdat de (mode I gedomineerde) bezwijkscheur vrijwel recht over de breedte van het proefstuk loopt. Verder ontwikkelt het scheurpatroon zich hoofdzakelijk door de epoxy, zodat variaties in de volumefractie van de vezels en de vezelverdeling slechts een

kleine invloed hebben op de gehomogeniseerde tractie-separatie-responsie. De introductie van een initiële imperfectie in het proefstuk (gecreëerd door een lokale afwezigheid van de aanhechting tussen vezels en epoxy) reduceert de breuksterkte van het proefstuk, en kan voor specifieke configuraties leiden tot een hogere taaigheid. De hogere taaigheid kan worden toegeschreven aan een verlenging van het scheurpad op microschaal, als gevolg waarvan meer energie moet worden gedissipeerd alvorens het vezel-epoxy proefstuk volledig bezwijkt.

Marcela Cid Alfaro
Oktober 2008

Curriculum Vitae



MARCELA VIVIANA CID ALFARO

born in Coyhaique, Chili

- Sep 2008 - present Researcher at Corus Research, Development & Technology, Department of Automotive Applications, Knowledge Group of Plasticity & Tribology.
- Mar 2004 - Jun 2008 Ph.D. candidate, Faculty of Aerospace Engineering, Delft University of Technology, the Netherlands.
- Aug 2007 - Oct 2007 Research visit to the Institute of Applied Mechanics (Chair I), Faculty of Civil and Environmental Engineering, University of Stuttgart, Germany.
- Aug 2001 - Feb 2004 Project engineer at ENAER (Chile's national aeronautical enterprise).
- Mar 1994 - Dec 2000 M.Sc. Mechanical Engineering, Universidad de Chile, Chili. (Graduated *Cum Laude*).